UNIVERSITÀ DEGLI STUDI DI PADOVA

SCUOLA DI SCIENZE

DIPARTIMENTO DI FISICA E ASTRONOMIA "GALILEO GALILEI"

Corso di Laurea Magistrale in Astronomia

POPULATION OF GAMMA-RAY SOURCES IN THE THIRD FERMI LAT CATALOG

Relatore: Ch. mo Prof. Alberto Franceschini
Co-relatore: Simona Paiano, dott.ssa

Laureando: Nikolina Šarčević
Matricola: 1110263

Anno Accademico 2016/2017

Acknowledgement

I'd like thank each person who helped me along the way.

First and foremost, I want to thank my mentor, professor Franceschini, for giving me the opportunity to work under his guidance and having faith in me. His wonderful lectures in Cosmology are the reason why I decided I wanted to do reasearch in this field.

Secondly, I want to thank professors Paola Marigo and Piero Rafanelli for being the best possible academic advisers one can wish for.

Thirdly, AstroMundus secretaries and overall wonderful people: Andrea Rumpold and Rossella Spiga - thank you for everything.

I also want to mention all the great teachers I was lucky to be taught by through AstroMundus master course - especially Markus Keil and Thorsten Battefeld from Goettingen, Olaf Reimer and Dominic Clancy from Innsbruck and the whole Astronomy department in Padova.

I want to thank my Astro-family for keeping up with me and listening to my student-drama for years. Iuliia, Max, Ernesto and Robert: thank you for being the best of friends. I love you so very much.

Robert, you get to be mentioned twice since this thesis would not be written without your advice, tips and knowledge.

Lastly, I'd like to thank my husband for being not just the moral support but the finantial one as well. I could not do this without you.

Nikolina, Padova 2017

Abstract

The Third Fermi LAT catalog (3FGL) is the most important astronomical catalog of gamma-ray sources, a long-lasting reference for high-energy astrophysics. As of today, perhaps surprisingly, more than a third of 3FGL sources lack a classification, not being identified nor even associated to sources at other wavelengths. Therefore finding a tool that could aid in the identification would be very helpful. To this purpose, we selected data from 3FGL, processed and analyzed them for the various categories of objects. In a first exploratory part of our investigation, we built histograms for galactic latitudes, photon fluxes, energy fluxex, spectral indices, variability indices and redshift of our samples, and tried interpreting the distributions. Secondly, we also built broad-band color-color diagrams that we used as diagnostic tools to verify the nature of already associated objects, and particularly to test those of the unidentified sources.

Contents

List of Figures

List of Tables

Chapter 1

Introduction

1.1 Aim of this thesis

The Fermi space observatory mission, since its launch in 2008, has collected, and is still collecting, a substantial amount of data on gamma-ray emissions from the sky in the photon energy interval from 20 MeV to 300 GeV. This is a full, unprecedented exploration of the high-energy sky. More than 3000 individual sources have been identified in the most recent Fermi catalog, based on a collection of data during the last 9 years, the Third Fermi Gamma-ray Source catalog, 3FGL. The observatory scans the whole sky in about 3 hours, thanks to its enormous field-of-view, such that 3FGL is based on 25000 repeated scans of the sky.

A vast variety of cosmic gamma-ray sources are represented in 3FGL, from local objects in the Milky Way to the most distant quasars. However, what is remarkable about this unique exploration of the sky is that a large fraction, about 34 %, of these objects are still unidentified or unassociated.

The present Thesis is dedicated to an investigation of the possible nature of these unidentified sources, with the aim of checking about the presence of new and unexpected phenomena that might reveal unexpected physical processes.

Our work has two main phases. In the first part, we derive a variety of properties of already known and already identified classes of Fermi gamma-ray sources. The parameters used in our analysis are in a first instance: galactic latitude, photon flux, energy flux, spectral index, variability index and redshift. Secondly, we used broad-band flux data from the literature in radio, optical, X and gamma bands and constructed color-color diagrams for all categories of Fermi objects.

The aim of the second part of this thesis is to compare in a statistical sense properties of the population of unidentified sources to characteristics of known sources and try to infer from that the possible nature of unassociated Fermi objects. In this way, color-color diagrams are used as diagnostic tool to deduce and predict the category of Fermi sources that lack classification.

Classes of objects we specifically inspected are: two blazar classes (BL Lacertae [BL Lacs] and flat spectrum radio quasars [FSRQs]), pulsars, BCU class (blazar candidates of unknown type) and UFOs (unidentified Fermi sources). Blazars are a broad class of Active Galactic Nuclei showing extreme properties of variability, high degree of polarization, point-like shapes, very broad-band emission from radio to gamma-rays with typically power-law spectral shapes. These properties are interpreted as due to "jetted" emission towards the observer because of relativistic motion of plasma clouds.

1.2 Outline of work

We start this thesis by a general overview of high energy astrophysics, with emphasis on gamma-ray astronomy (Ch. 2). We then provide a description of physical processes responsible for gamma-ray emission (§ 2.2) and relevant astrophysical sources (§ 2.3).

Chapter 3 talks about the Fermi mission and catalog, while the following chapter is reserved for summary of the data that we used and steps we took to process the data.

In Chapter 5 we present the first part of our work. We give a detailed analysis of statistical properties of known classes of sources in the Third Fermi catalog. The subsequent Chapter (6) is a discussion of the second part of our work, where we use color-color diagrams to predict the nature of unidentified Fermi sources.

We finish this thesis by providing a summary (§ 7) of our investigation.

Disclaimer

The theoretical part of this thesis relies on extensive amount of literature. However, some sections rely on certain books or papers to a higher degree. I would like to disclaim that, first of all, outline of this work was created (to some extent) based on the outline of theses Iani (2014) and Paiano (2014). Simona Paiano's thesis also provided a base for Chapter §2.1 and § 2.3. M. Longair's *High energy astrophysics* book, as well as a summary Ghisellini (2013), were used as a main resource for Chapter 2.2.

Chapter 2

Gamma-ray astrophysics

2.1 High energy astrophysics

The discovery of cosmic rays via balloon experiments conducted in Innsbruck, Austria at the beginning of last century by V. F. Hess, widened our knowledge of physical processes that occur in Universe and opened a new chapter in astrophysics that is referred to as *high energy astrophysics*. High energy astrophysics (HEA) is thus a branch that studies high energy astrophysical phenomena and the branches are further divided based on which part of electromagnetic spectrum or which particles are being studied. Therefore, we can speak of extreme UV-astronomy, X-ray astronomy, gamma-ray astronomy or neutrino and cosmic ray astronomy. Each abovementioned theoretical field has corresponding observational and instrumentational field. Major discoveries are usually obtained through collaborations and missions and some of them are: IceCube (neutrinos), AUGER (cosmic rays), MAGIC (gamma-rays) and FERMI (gamma-rays). In the next few sections, fields relevant to this work will be briefly described.

2.1.1 Cosmic rays

Cosmic rays (CRs) are defined as energetic particles that originate outside the Solar System. About 98 % of particles are protons and nuclei (out of which 87 % are protons, 12 % are alpha-particles and rest are heavier nuclei), while remaining 2 % are electrons, neutrons, neutrinos and photons [(Longair, 2011), (Paiano, 2014)]. Energy spectrum of cosmic rays extends over wide range of energies and (Figure 2.1) is described by a power-law:

$$N(E)\mathrm{d}E = CE^{-\alpha}\mathrm{d}E \tag{2.1}$$

with α being *spectral index* that has values:

$$\alpha = \begin{cases} 2.7, & \text{up to } E \sim 10^{15.5} \text{ eV (100 TeV)} \\ 3, & \text{for } 10^{15.5} \text{ eV} < E < 10^{18}\text{eV} \\ 2.6, & \text{from } E \sim 10^{18} \text{ eV} \end{cases} \tag{2.2}$$

The regions where spectral index changes its value (from 2.7 to 3) to (3 to 2.6) are colloquially known as the "knee" and the "ankle"[1], respectively. Since energy span of cosmic rays is substantial, it is convenient in practice to divide it into ranges "above and below the knee" and the corresponding particle populations are classified as *galactic* and *extragalactic*. That is also indicated in the Figure 2.1, with different symbols representing different detection techniques used. It can be noted that there is an obvious lack in spectral features, aside from the knee and ankle. This, combined with the extent of energies, implies universality in the origin of particles that comprise the CR population. (Paiano, 2014)

The problem arises from the fact that most of the CR particles are charged and will be deflected in all-present diffuse magnetic fields (galactic and intergalactic). That means their origin is impossible to determine. Hence, the only species that can be used to gain information about the region in space where they were formed are neutral particles. Neutral cosmic ray particles are: neutrons, neutrinos and photons.

[1] Often the spectrum is referred to as "Marlene Dietrich's leg".

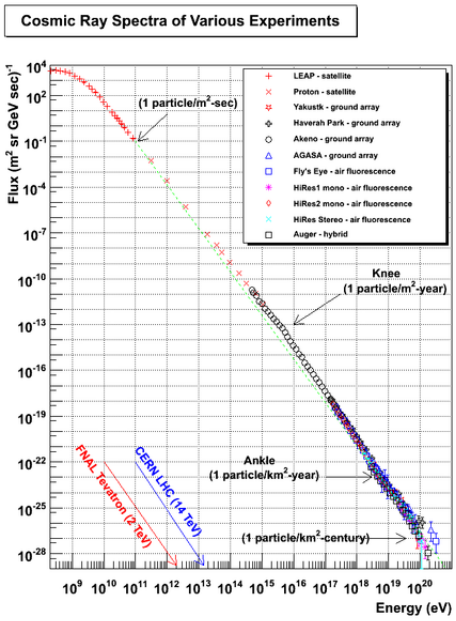

Figure 2.1: Differential energy spectrum of cosmic rays. Two characteristic features can be distinguished: the "knee" at 10^{15} eV and the "ankle" at 10^{18} eV. It can be noted that spectrum spans over the wide range of energies. Arrival frequences of particles, depending on their energy, are also indicated in the plot. Figure taken from (Hanlon).

- Neutrons have a half life of just under 15 minutes so only a negligible fraction of original neutron flux arrives to Earth.
- Neutrinos are also problematic due to their extremely small cross-section so a large active volume of detector is needed.

Therefore, the only species left are high energy photons, or *gamma-rays*.

2.1.2 Gamma-rays

Although only a very small fraction of CR, gamma-ray photons can be used to extract information about astrophysical objects. The major advantage over other particle families is that photons are very easy to detect by one of many developed techniques. Gamma-ray detection can provide an insight into their formation and acceleration mechanisms at origin as well as propagation effects along their trajectories towards the Earth (hence, an information about the medium).

Gamma-ray emission is related to acceleration of particles above the TeV range and is located at the furthest part of electromagnetic spectrum (Figure), in the energy range between 10^5 to 10^{20} eV (Paiano, 2014).

This energy range is further divided into sub-ranges, each associated with different detection technique. The energy intervals and designations are given in Table 2.1.

Table 2.1: Gamma-ray energy intervals and their designations

Energy Interval	Designation	Abbrevation
0.51 MeV-10 MeV	Low Energy	LE
10 MeV-30 MeV	Medium Energy	ME
30 MeV-100 GeV	High Energy	HE
100 GeV-100 TeV	Very High Energy	VHE
100 TeV-100 EeV	Ultra High Energy and Extremely High Energy	UHE and EHE

- ***Low Energy (LE)*** covers the lowest interval in gamma-range (0.51 MeV-10 MeV) and these photons are absorbed in the atmosphere. Their detection is only possible from space. Detectors in use are usually scintillators.

- ***Medium Energy (ME)*** photons extend from 30 MeV to 100 GeV. The radiative process in question is Compton scattering and these photons need to be detected by space-borne telescopes.
- ***High Energy (HE)*** gamma-photons have energy in the interval from 30 MeV to 100 GeV. Just like two abovementioned photon classes, HE-photons are also studied from space. The radiation process (and, thus, detection technique) characteristic for these photons is pair creation. Fermi telescope operates in this range.
- ***Very High Energy (VHE)*** can be studied by ground-based instruments as they are so energetic, they produce air-showers. Detectors used are Cherenkov telescopes.
- ***Ultra High Energy (UHE)*** and ***Extremely High Energy (EHE)*** photons are the most energetic ones, in the interval from 100 TeV to 100 EeV. Their interaction with atmosphere produce very extended showers so and are studied in the field of Auger physics.

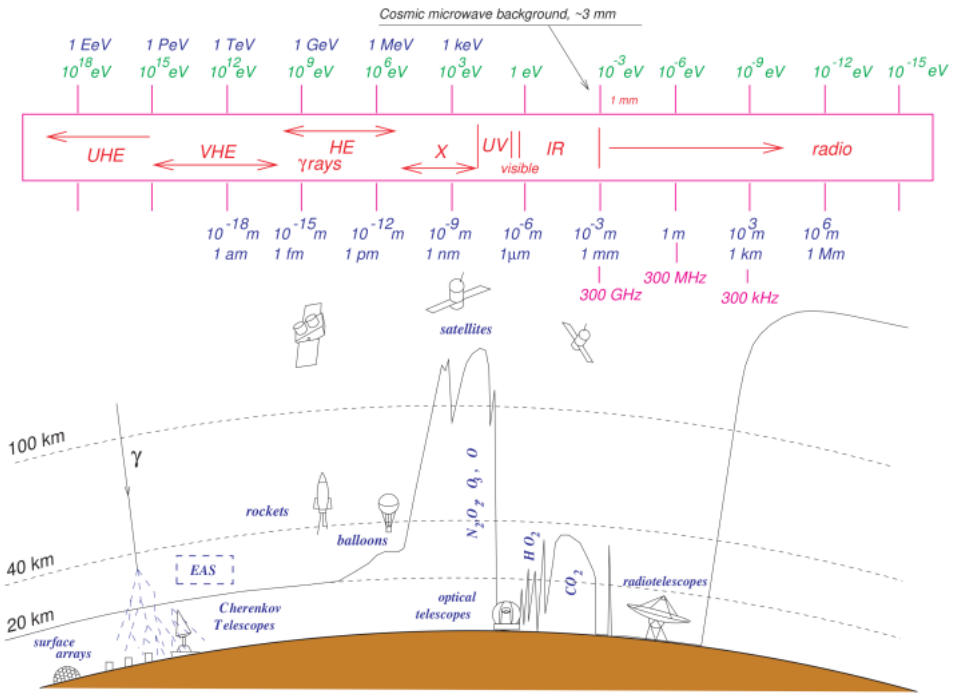

Figure 2.2: Schematic representation of electromagnetic spectrum and corresponding atmospheric transparency (observational window). Continuous line represents the height at which a detector can receive half of the total incoming radiation for every wavelength. (Paiano, 2014)

2.2 Relevant radiative processes

Gamma-rays are closely related to the most energetic and violent processes in the Universe. They are created (and accelerated) by particles of very high energies (Paiano, 2014). Understanding the mechanisms that are responsible for creation of gamma-rays is, therefore, fundamental. In this section, main processes will be described as succinctly as possible.

2.2.1 Bremsstrahlung

Bremsstrahlung is the emission of radiation in a scenario in which a free charged particle (electron) is moving at high velocity and passes the stationary nucleus. Interaction of electron with the field will affect electron so that it will change trajectory and emit energy in form of radiation at the expense of its kinetic energy (hence the name "bremsstrahlung"). Therefore, bremsstrahlung a mechanism in which electrons lose their energy to radiation. The detailed derivation of parameters for this process is not relevant for this work, so only main result is given.

Radiation spectrum of electron interacting with a charged nucleus with parameter b is:

$$I(\omega) = A\,\frac{\omega^2}{\gamma^2 v^2}\left[\frac{1}{\gamma^2}K_0^2\left(\frac{\omega b}{\gamma v}\right) + K_1^2\left(\frac{\omega b}{\gamma v}\right)\right] \tag{2.3}$$

where K_0 and K_1 are modified Bessel functions of order 0 and 1 and A is:

$$A = \frac{Z^2 e^6}{24\pi\epsilon_0^3 c^3 m_e^2 v^2} \tag{2.4}$$

The radiation spectrum of bremsstrahlung (Fig. 2.2.1) has two main features: continuous part and a cut-off. Each feature can be computed by calculating asymptotic limits of Bessel functions. Exponential cut-off is in high-frequency domain while continuous spectrum is dominant at low frequences (Longair, 2011).

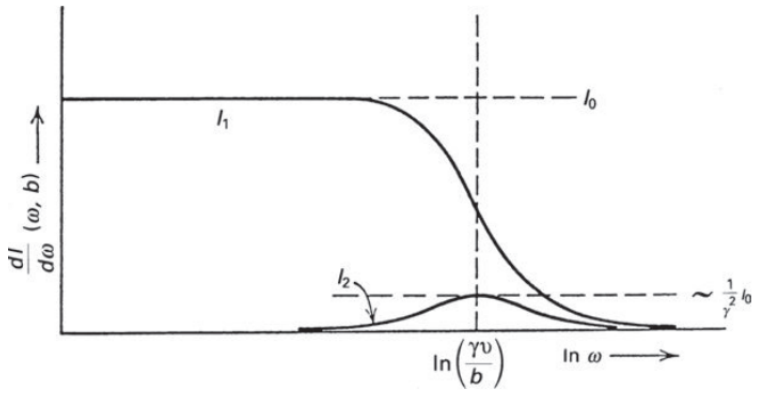

Figure 2.3: Spectrum of Bremsstrahlung. The spectrum is flat at low energies and shows an exponential decay at higher frequencies. Taken from (Longair, 2011)

The total energy loss rate of electrons, in cases of non-relativistic and relativistic Bremsstrahlung, is given in Eq. 2.10. Relativstic Bremsstrahlung results in exponential loss of energy of electron (Longair, 2011).

$$-\left(\frac{\mathrm{d}E}{\mathrm{d}t}\right) \propto \begin{cases} E^{1/2} & \text{non-relativistic Bremsstrahlung} \\ E & \text{relativistic Bremsstrahlung} \end{cases} \tag{2.5}$$

Bremsstrahlung radiation can be found in verious astrophysical sources, since its generation does not require some "special" conditions. Radio emission of nebulae are due to this process as well as an X-ray emission in AGN accretion mechanisms. When electrons are extremely relativistic, resulting spectrum can be in gamma-region of electromagnetic spectrum (Paiano, 2014).

2.2.2 Synchrotron radiation

When relativistic leptons (electrons of mass m_e, for example), travel in region where magnetic field of intensity B is present, they will undergo an acceleration due to Lorentz force and will radiate (Ghisellini, 2013). In other words, in a uniform magnetic field, relativistic electron will spiral[2] along filed lines at a constant pitch angle α^2 with gyro-frequency:

$$\nu_g = \frac{e\ B}{2\ \pi\ \gamma\ m_\mathrm{e}} \tag{2.6}$$

where γ is Lorentz factor:

$$\gamma = \left(1 - \beta^2\right)^{-\frac{1}{2}} \text{ and } \beta = \frac{v}{c} \tag{2.7}$$

The averge energy-loss rate is equal to:

$$-\left(\frac{\mathrm{d}E}{\mathrm{d}t}\right) = \frac{4}{3}\ \sigma_\mathrm{T}\ c\ U_\mathrm{mag}\ \beta^2\gamma^2 \tag{2.8}$$

U_mag represents energy density of magnetic field:

$$U_\mathrm{mag} = \frac{B^2}{2\mu_0} \tag{2.9}$$

Quantity μ_0 is permeability and σ_T from equation 2.8 is the Thomson scattering cross-section.

Spectrum emitted by a single electron has two limits, one for low (power-law) and one for high frequency domain (exponential cut-off):

$$F(\nu/\nu_c) \propto \begin{cases} \left(\frac{1}{2}\frac{\nu}{\nu_\mathrm{c}}\right)^{1/3}, & \text{for } \nu \ll \nu_\mathrm{c} \\ \left(\frac{\nu}{\nu_\mathrm{c}}\right)^{1/2} \exp\left(-\frac{\nu}{\nu_\mathrm{c}}\right), & \text{for } \nu \gg \nu_\mathrm{c} \end{cases} \tag{2.10}$$

where ν_c is defined as:

$$\nu_\mathrm{c} \equiv \frac{3}{2}\nu_\mathrm{s} \sin\theta \tag{2.11}$$

and ν_s is a typical synchrotron frequency:

$$\nu_\mathrm{s} = \gamma^2 \frac{e\ B}{2\ \pi\ m_\mathrm{e}\ c} \tag{2.12}$$

Emission from many particles will also have a power law form and it will depend on energy distribution of particles (i.e. it will depend on index of distribution p) as:

$$\alpha = \frac{p-1}{2} \tag{2.13}$$

Typical example of synchrotron spectra can be seen in Fig 2.4. In Fig. 2.4a, an example of synchrotron spectrum emitted by a single electron is presented. Spectrum has a power law form with spectral index of $\frac{1}{3}$ in low frequency domain. The shape of spectrum in region of high frequences is $\propto \exp(-x)$ (where x is defined as $x \equiv \frac{\nu}{\nu_\mathrm{c}}$).

Synchrotron radiation is all-present in high energy astrophysics. Many astrophysical objects are emitting radiation due to synchrotron process, like supernova remnants, Galaxy radio emission or pulsar wind nebulae (PWN). Notable extragalactic sources are SMBH or quasars whose emission in optical and X-ray continuum is due to synchrotron radiation Longair (2011). Lastly, jet physics cannot be studied without connecting it to this mechanism. Each synchrotron emitter will naturally have different spectral index (since the parameters will differ); however, it is observed that extended radio

[2] Electron's trajectory is helicoidal.

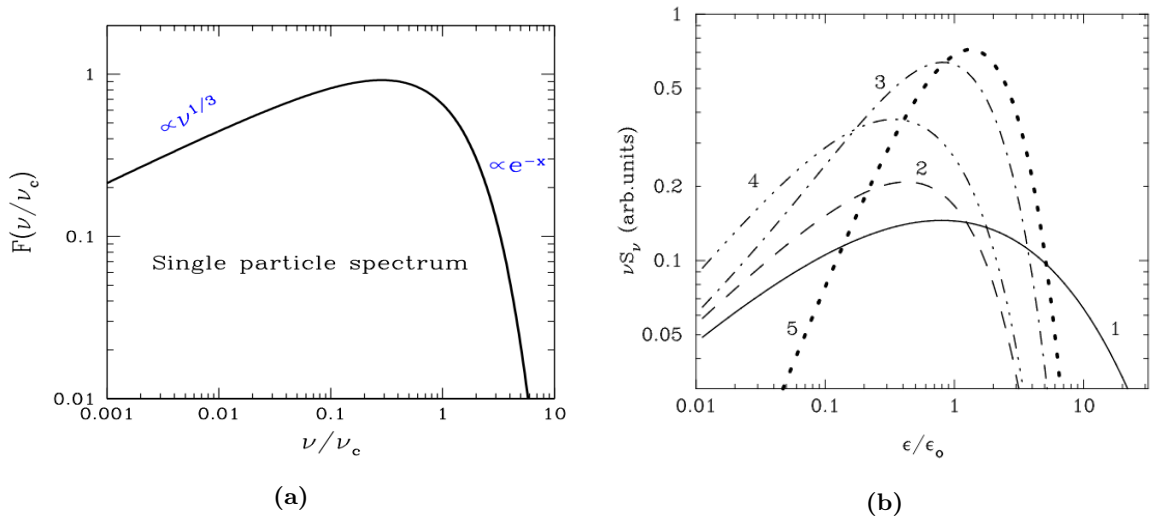

(a) **(b)**

Figure 2.4: Examples of synchrotron radiation spectra. (a) Spectrum emitted by a single electron. Low-frequency part can be described by a power law with index $\alpha = \frac{1}{3}$ while slope in high frequency domain is $\exp(-x)$. x is defined as $x \equiv \frac{\nu}{\nu_c}$. (b) "Spectral Energy Distributions of the synchrotron radiation produced by protons of different distribution spectra (curves 1, 2, 3 and 4). Curve 5 is the SED of synchrotron radiation of mono-energetic protons for which the function decays as $x^{4/3}\exp(-x)$". Figure (a) was taken from Ghisellini (2013) and illustration (b) was taken from(Aharonian, 2000) (b).

sources usually have spectral index $\alpha \sim 0.7$ (which implies the slope of electron distribution function of $p \sim 2.4$). Slope of radio jets is a bit flatter, $\alpha \sim 0.5$. This is indicative of higher degree of particle acceleration, compared to extended radio sources (Blandford et al., 1990). Lastly, it should be mentioned (althoguh it is obvious) the importance of synchrotron radiation in terms of it being an excelent way of determining the magnetic filed of emitters.

2.2.3 Synchrotron-self Compton

If a population of relativistic electrons exsists in a magnetized region, they will produce synchrotron radiation and fill the zone with photons. The synchrotron photons will, with certain probability, interact with electrons via ICS process. In this case, the electrons will be interacting "twice"[3]. This mechanism is called *synchrotron-self Compton (SCC)* (Ghisellini, 2013).

The spectrum of SSC is of a power-law form, with index of $\alpha = \frac{5}{2}$:

$$S_\nu \propto \frac{\theta^2 \nu^{5/2}}{B^{1/2}} \tag{2.14}$$

where Ω is the solid angle subtended by the source

$$\Omega \approx \theta^2 \tag{2.15}$$

and θ is the angular size of the source (Longair, 2011). Typical SSC spectrum is given in Figure 2.5.

"This radiation can be found at radio, cm and mm wavelengths in AGN. Presence of this radiation is a confirmation of exsistance of relativistic electrons in source regions." (Longair, 2011)

Self-absorbed part of spectrum is rarely observed in practice and never in radio-loud AGN. The explanation is taken from (Ghisellini, 2013) and is as follows: "in radio-loud AGN, SC at radio refquences comes from *radio lobes*[4] and from *jets*. Jet emission is beamed and it is a superposition of fluxes produced in several regions. Fluxes from regions close to central engine (compact ones) self-absorb at high frequences (typically 100 GHz). The bigger the regions are, the smaller their self-absorbed frequency is. However, the flux peak of each component[5] is aproximately constant. Hence, when the contribution of all components is summed up, the radio spectrum is *flat*". This effect is presented in Figure 2.6.

[3] First by making the synchrotron radiation and then scattering it to higher energies.

[4] Radio lobes are extended structures (several kpc in size), relaxed, unbeamed and usually self-absorbing at very small frequences (Ghisellini, 2013).

[5] the flux at self-absorption frequency

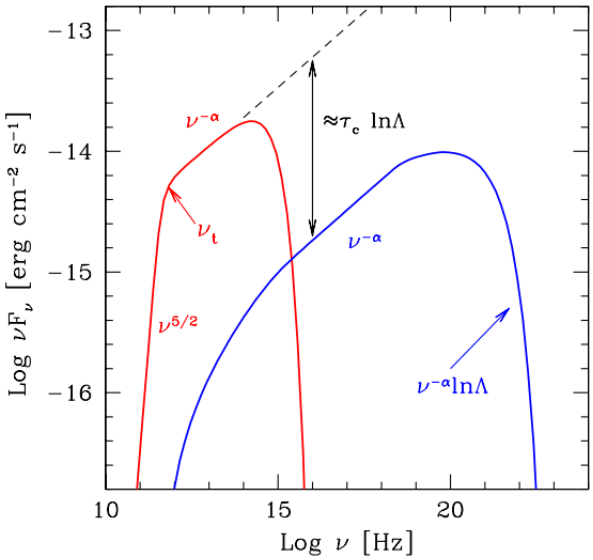

Figure 2.5: Typical example of synchrotron-self Compton spectrum. Spectral index is 5/2. Taken from (Ghisellini, 2013).

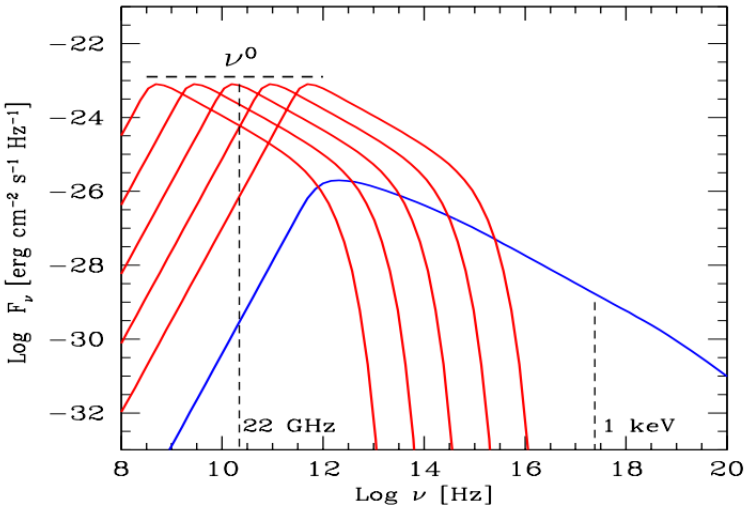

Figure 2.6: "Example of the composite spectrum of a flat spectrum quasars (FSRQ). The reason behind the flat spectrum is that different parts of the jet contribute at different frequencies, but in a coherent way. The blue line is the SSC spectrum. Suppose to observe, with the VLBI, at 22 GHz: in this framework, the jet component peaking at this frequency will always be observed. In that way, the self–absorption frequency of component, for which the angular size is being measure, is automatically being observed" (Ghisellini, 2013). Picture taken from (Ghisellini, 2013).

2.2.4 Compton scattering

Scattering is the simplest way of interaction between photons and free electrons. The general picture that describes this process is *Compton scattering* and has two limiting cases. One can easily be derived using classical treatment (Thomson scattering) while other requires quantum-mechanical approach (Compton scattering). Since the emphasis of this chapter section is on gamma-ray production, only important results from Compton (and Thomson) scattering will be covered and used as a pedagogical "leap" to Inverse Compton scattering.

Thomson scattering

The first, classical case, is one where electron is considered at rest and the incoming photon has frequency:

$$\nu \ll \frac{m_e c^2}{h} \tag{2.16}$$

Then, photon will be elasticaly scattered and the probability of this process is given by Thomson cross-section:

$$\sigma_T = \frac{e^4}{6\pi\epsilon_0^2 m_e^2 c^4} = 6.653 \times 10^{-29}\ \mathrm{m}^2 \tag{2.17}$$

Thomson's result has several important consequences. First, scattering is symmetric[6] (radiation is scattered "backwards" in the same amount as in the foreward direction). Secondly, if radiation is incoherent, radiated energy will be proportional to the sum of incident intensities. Next result account is that scattered radiation will be polarized, even if the incoming radiation was not. Lastly, this process is a way of preventing photons to escape the region. Also, there is no change in energy of photons.

Compton scattering

In case when photon energies are comparable or larger than $m_e c^2$, the picture is different from the one described above. After some mathematical treatment, the famous result is that there will be an increase of photon's wavelength (i.e. photon will lose energy through encounter):

$$\frac{\Delta\lambda}{\lambda} = \frac{\lambda' - \lambda}{\lambda} = \frac{\hbar\omega}{m_e c^2}(1 - \cos\alpha) \tag{2.18}$$

where α is the scattering angle. If the result is written in this form

$$\frac{\omega'}{\omega} = \frac{1 - \beta\cos\theta}{1 - \beta\cos\theta' + \left(\frac{\hbar\omega}{\gamma m_e c^2}\right)(1 - \cos\alpha)} \tag{2.19}$$

then, it can be used to understand how energy can be exchanged between electron and radiation field. It should be noted that θ and θ' represent the angles between incoming photon and velocity vector of electron before and after collision, respectively. Compton scattering is a generalization and in case when electron is very slow ($v \ll c$) or when photon has energy $\hbar\omega \ll m_e c^2$, Thomson scattering is obtained.

Cross-section for this process is given by Klein-Nishina formula:

$$\sigma_{KN} = \pi r_e^2 \frac{1}{x}\left\{\left[1 - \frac{2(x+1)}{x^2}\right]\ln(2x+1) + \frac{1}{2} + \frac{4}{x} - \frac{1}{2(2x+1)^2}\right\} \tag{2.20}$$

where

$$x = \frac{\hbar\omega}{m_e c^2} \tag{2.21}$$

and

$$r_e = \frac{e^2}{4\pi\epsilon_o m_e c^2} \tag{2.22}$$

is classical electron radius. Klein-Nishina will reduce to:

$$\sigma_{KN} = \frac{8\pi}{3} r_e^2 (1 - 2x) \approx \sigma_T (1 - 2x) \approx \sigma_T \text{ for } x \ll 1 \tag{2.23}$$

and to:

$$\sigma_{KN} = \pi r_e^2 \frac{1}{x}\left(\ln 2x + \frac{1}{2}\right) \text{ for } \gamma \gg 1 \tag{2.24}$$

[6] colloquially referred to as "the peanut shape".

To be able to predict where photons will be scattered, expression for differential cross-section is needed and the main result (which will not be given in its mathematical form) is that scattering becomes preferentially forward with the increase of photon energy.

2.2.5 Inverse Compton scattering

Inverse Compton scattering (ICS) is a process where ultra-relativistic electrons scatter photons of low energy and, as a result, photons gain energy at the expense of kinetic energy of electrons. To get mathematical result, the reference frame from which the Thomson cross-section is the solution is considered.

If S is the laboratory reference frame and S' is rest frame of electron and if $\gamma\hbar\omega \ll m_e c^2$, then

$$\hbar\omega' = \gamma\hbar\omega(1 + \beta\cos\theta) \tag{2.25}$$

Obtaining the abberation relations for incident angles in both frames of reference and using the Thomson limit, the loss rate is retrieved as:

$$-\left(\frac{\mathrm{d}E}{\mathrm{d}t}\right)' = \sigma_{\mathrm{T}} c U'_{\mathrm{rad}} \tag{2.26}$$

To get the expression for energy density, the quickest way is to use the invariance of the four-volume $\mathrm{d}t\mathrm{d}x\mathrm{d}y\mathrm{d}z$ and the configuration in which $\mathrm{d}y = \mathrm{d}y'$ and $\mathrm{d}z = \mathrm{d}z'$. Then, differential product $\mathrm{d}t\mathrm{d}x$ needs to be related to the differential product $\mathrm{d}t'\mathrm{d}x'$ in frame S'. Jacobian is, of course, unity and all it's left is just to combine this result to create new invariants and energy density of radiation is obtained as:

$$U'_{\mathrm{rad}} = U_{\mathrm{rad}}[\gamma(1 + \beta\cos\theta)]^2 \tag{2.27}$$

If the radiation field is isotropic, through calculation of the contribution to energy density (in the frame S'), radiation energy density is:

$$U'_{\mathrm{rad}} = U_{\mathrm{rad}}\frac{4}{3}(\gamma^2 - \frac{1}{4}) \tag{2.28}$$

Equation 2.28 is already showing the significant increase in energy density in frame S'. Relation 2.28 can be substituted into 2.26, and making sure that $\dot{E}$ is invariant, after some mathematical manipulations, the main result is retrieved as:

$$\left(\frac{\mathrm{d}E}{\mathrm{d}t}\right)_{\mathrm{IC}} = \frac{4}{3}\sigma_{\mathrm{T}} c U_{\mathrm{rad}} \beta^2 \gamma^2 \tag{2.29}$$

and is valid as long as intital condition $\gamma\hbar\omega \ll m_e c^2$ holds. There is an analogy with synchrotron radiation, namely 2.8. In case of IC, energy loss rate depends on the electric field whereas in synchrotron case the magnetic field is responsible. This correlation can be used to construct a power-law spectrum of radiation. Spectral index of synchrotron radiation is given by equation 2.13. After dimensional analysis, it is easy to conclude that the spactral index in this case is (Longair, 2011):

$$\alpha_{\mathrm{ph}} = \frac{p+1}{2} \tag{2.30}$$

Inverse Compton spectrum is presented in Fig. 2.7

One of the most important consequence of IC (as well as in synchrotron case) is that photons can tremendeously increase their energy (Eq. 2.29) through such process - γ can take values in wide interval (100-1000) in various astrophysical sources. As an example, radio photons can be scattered to UV, FIR photons to X and optical radiation can be upscattered to gamma-ray domain. At the same time, the process is responsible for electron depletion in regions where IC occurs. In the end, it should be noted that above case that was treated mathematically is very simple compared to realistic scenario. In reality, situation is much more complicated and the evolution of source spectrum (with its problematics) is treated under name *Comptonisation*. Surface will be only scratched here and a rudimentary explanation will be given: the starting assumption was a monochromatic isotropic radiation field. That is definitely not realistic (but it is needed as a starting point, i.e. to simplify

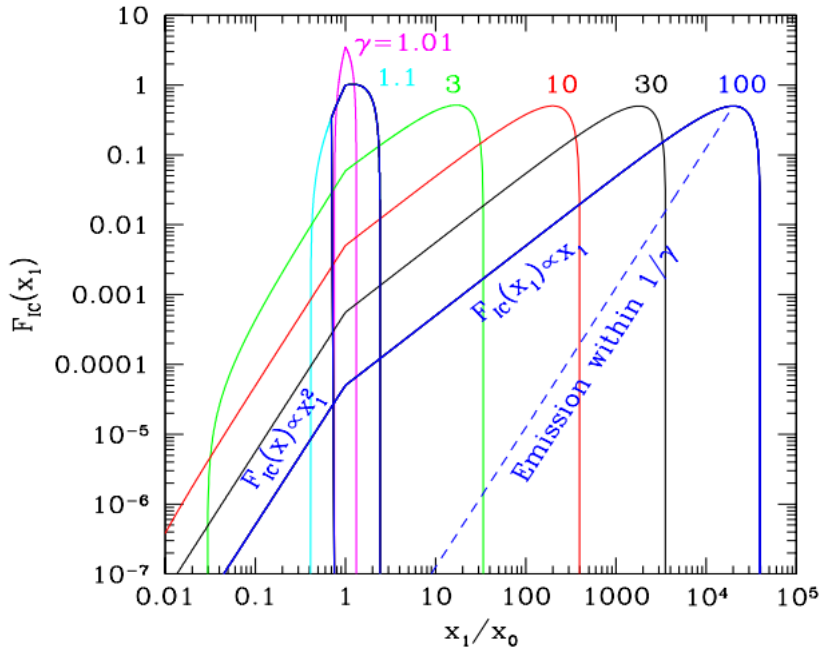

Figure 2.7: Inverse Compton spectrum generated by electrons of different γ. The dashed line corresponds to the spectrum emitted within the $1/\gamma$ beaming cone: it always contains the 75 % of the total power, for any γ. Picture taken from (Ghisellini, 2013).

calculations). In reality, IC spectrum is a contribution of each scattering (and even thermal electrons can produce a power law), so the problem gets even more complicated. The reader is advised to consult Pozdnyakov, Sobol and Sunyaev (1983) for more details. Finally, the best way to illustrate what was said is to provide a Comptonisation spectrum, as it was done in Fig. 2.8.

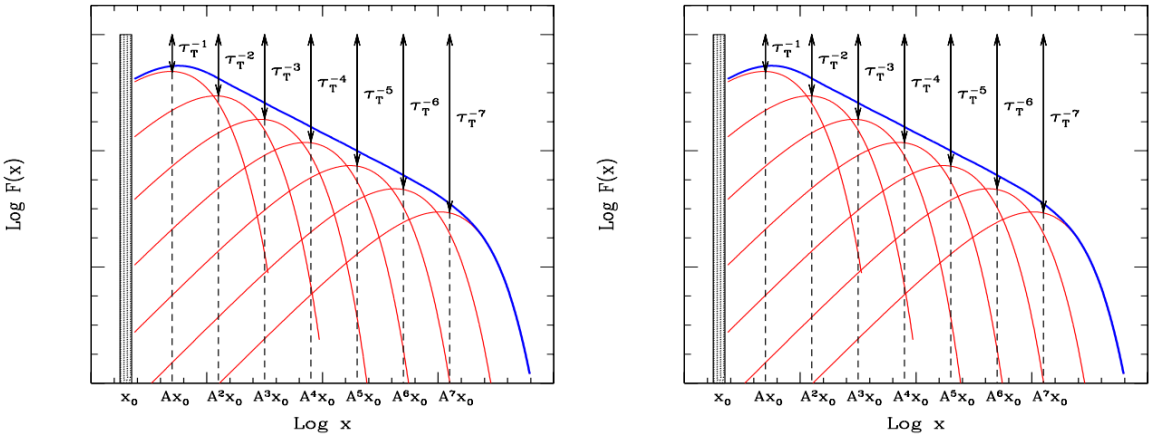

(a) **(b)**

Figure 2.8: Multiple Comptons scatterings for different electron temperatures and y parameters. y parameter represents the average number of scatterings and average fractional energy gain for scattering. Comptonisation becomes important for $y > 1$. Taken from (Ghisellini, 2013).

2.2.6 Fermi acceleration

Fermi acceleration[7] is a process by which particles can be accelerated to high energies. In this scenario, charged particles are colliding with ISM clouds and are reflected from, what Fermi originally called

[7]This segment is taken from (Longair, 2011).

"magnetic mirrors". The mirrors represent the irregularities in the Galactic magnetic field and the whole process is stochastic in nature (mirrors are moving randomly).

If V is cloud velocity, v is particle velocity m and M are particle and cloud masses, respectively and if the encounter is represented as in Figure 2.9, then, provided that mirror has extremely large mass, the energy of the particle in center-of-momentum frame will be:

$$E^{'} = \gamma_V (E + V\ p\ \cos\theta) \tag{2.31}$$

where

$$\gamma_V = \left(1 - \frac{V^2}{c^2}\right)^{-\frac{1}{2}} \tag{2.32}$$

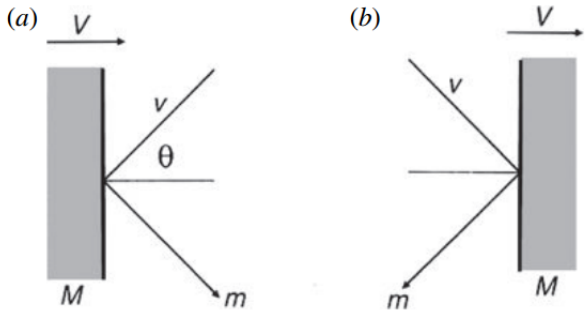

Figure 2.9: Schematic representation of Fermi mirror. Case (a) is a head-on collision while (b) illustrates a following collision. The probability of a head-on collision is proportional to $1 + \frac{V}{c}\cos\ \theta$ and $0 < \theta < \pi$. Picture is taken from (Longair, 2011).

After some mathematical manipulations and physics, an average energy gain per collision can be obtained as:

$$\left\langle \frac{\Delta E}{E} \right\rangle = \frac{8}{3}\left(\frac{V}{c}\right)^2 \tag{2.33}$$

The average energy gain per collision is of the second order of $\frac{V}{c}$, which further implies a very slow increase in the energy of particle. If L is a mean free path between clouds along a field line and time between collisions is equal $\frac{L}{c\ \cos\phi} = \frac{2\ L}{c}$ (ϕ is a pitch angle of particle w.r.t. magnetic field direction), then the average rate of energy iscrease is:

$$\frac{\mathrm{d}E}{\mathrm{d}t} = \frac{4}{3}\left(1 + \frac{V^2}{c\ L}\right)E = KE \tag{2.34}$$

Finally, the resulting energy spectrum is equal to:

$$\frac{\mathrm{d}N(E)}{\mathrm{d}E} = -\left(1 + \frac{1}{K\ \tau_{esc}}\right)\frac{N(E)}{E} \tag{2.35}$$

where τ_{esc} is time in whic particle remains within the accelerating region.

A power-law form energy spectrum is obtained:

$$N(E) \sim E^{-\alpha} \tag{2.36}$$

where

$$\alpha = 1 + \frac{1}{K\tau_{esc}} \tag{2.37}$$

Therefore, Fermi acceleration mechanism results in a power-law energy spectrum. This result has some theoretical omission and it was corrected later on. The power-law form still holds, only power-law index has changed to:

$$\alpha = \frac{3}{2}\left(1 + \frac{16}{9\ K\ \tau_{esc}}\right)^{\frac{1}{2}} - \frac{1}{2} \tag{2.38}$$

In summary, "charged particles will be accelerated when being repeadetly reflected and when crossing the shock front ("diffusive shock aceeleration"). Particle fractional energy gain is then of the order of the velocity of the shock front and will have energies observed in the CR spectrum. This effect is thought to be important in astrophysical shock waves, for example shock waves from supernova remnants or solar flares" (Paiano, 2014).

2.2.7 Pion decay

Inelastic proton-proton[8] (scatterings) can produce charged and neutral pions through reaction. Some of the possible scenarios are:

$$\mathrm{p} + \mathrm{p} \rightarrow \mathrm{p} + \mathrm{p} + \pi^0 \tag{2.39}$$

and

$$\mathrm{p} + \mathrm{p} \rightarrow \mathrm{p} + \mathrm{n} + \pi^+ \tag{2.40}$$

and

$$\mathrm{p} + \mathrm{p} \rightarrow \mathrm{p} + \mathrm{p} + \pi^+ + \pi^- \tag{2.41}$$

Proton treshold energy for this type reaction is about 290 MeV. It should be said that even more particles can be produced if proton energies are high enough. Reactions (2.40 and 2.41), in which a positively and negatively charged pions are created, do not concern us at this instance. However, the reaction channel (2.39) has astrophysical importance, since the neutral pion will decay into two gamma-ray photons as:

$$\pi^0 \rightarrow 2\gamma \tag{2.42}$$

Each photon has an energy equal to (Ackermann et al., 2013):

$$\frac{m_{\pi^0} c^2}{2} = 67.5 \text{ MeV} \tag{2.43}$$

in the rest frame of neutral pion, where $\frac{m_{\pi^0} c^2}{2}$ is the rest mass of pion. Spectrum for gamma-ray production is given in Figure 2.10. Pion decay spectrum traces parent proton spectrum (Dermer, 2013) up to few GeV and is described by a power-law with power-law index $\alpha = 2.85$ below 200 MeV. This spectral characteristic, referred to as "pion-decay bump", is used as an identification of pion-decay gamma-rays and therby high-energy protons (Ackermann et al., 2013). This allows the cosmic-ray source spectrum measurement. It should be said that bremsstrahlung can significantely affect the spectrum as low energies (Dermer et al., 2013). Astrophysical objects of interest in this aspect are usually supernova remnants.

2.2.8 Pair annihilation

The most extreme means of energy loss for electrons is pair annihilation. Electron-positron annihilation process results in production of gamma-rays. These photons can interact with medium photons and produce electron-poistron pairs(Longair, 2011).

In order for process of annihilation to occur, there has to exsist a positron source. Astrophysical events and locales responsible for positron creation are as follows:

[8] more generally, nuclear-nuclear collisions (Ackermann et al., 2013)

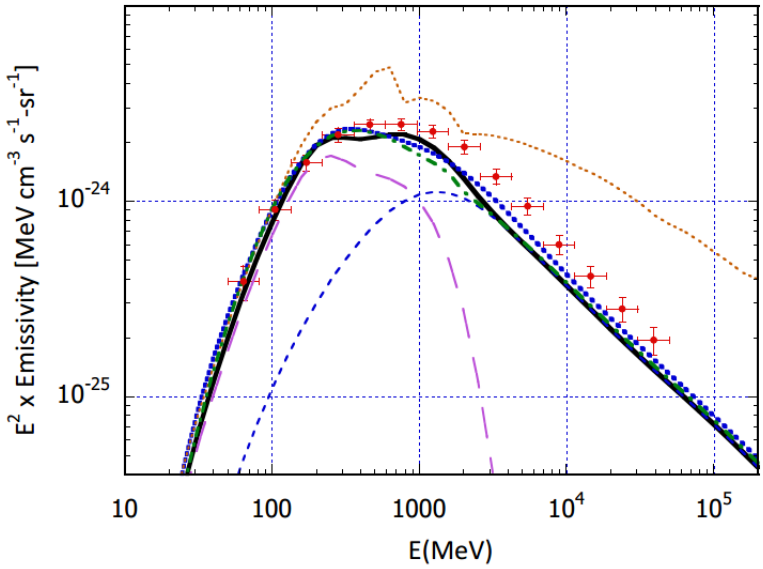

Figure 2.10: Calculation for $p + p \rightarrow \pi^0 \rightarrow 2\gamma$ production compared with preliminary *Fermi*-LAT emissivity (red data points). Proton flux is given by a power-law with power-law index $\alpha = 2.85$ below 200 MeV. Above 200 MeV, $\alpha = 2.65$ and is reproducing PAMELA hardening. Heavy solid curve represents hybrid model by Dermer. Long-dashed light purple and short-dashed light blue curves represent isobar and scaling components, respectively. Blue dotted curve is the clculation using the Kamae model. An all-isobar calculation and an an all-scaling calculation are shown for comparison by the light-dotted orange and dot-dashed green curves, respectively. Picture and caption taken from (Dermer et al., 2013)

- π^+ **decay**: Pions are created in proton-proton and other nuclear-nuclear collisions, as it is described in section 2.2.7. Positively and negatively charged pions will decay into muons, with muon neutrinos and muon antineutrinos in following reactions:

$$\pi^+ \rightarrow \mu^+ + \nu_\mu \tag{2.44}$$

and

$$\pi^- \rightarrow \mu^- + \bar{\nu}_\mu \tag{2.45}$$

Further on, low energy muons[9] will decay into positrons, electrons, muon and electron neutrinos and muon and electron antineutrinos as:

$$\mu^+ \rightarrow e^+ + \nu_e + \bar{\nu}_\mu \tag{2.46}$$

and

$$\mu^- \rightarrow e^- + \bar{\nu}_e + \nu_\mu \tag{2.47}$$

Charged pion decay reactions have a mean lifetime of 2.551×10^{-8} s while mean lifetime of muon decay reaction is 2.2001×10^{-6} s. A very handy schematic diagram of pion (neutral and charged) decay is given in Figure 2.11.

Decay of isotopes created in Supernova events: Some isotopes that are created through Supernova nucleosynthesis are radioactive and will sponteneously decay through β decay. One example is the β^+ decay of ^{26}Al which has a mean lifetime of 1.1×10^6years. This isotpe is created in a SN explosion and therefore injected into ISM where it will decay and emit positrons.

[9] High energy mouns (from high energy CR entering the atmosphere) are able to penetrate atmosphere and deeper underground.

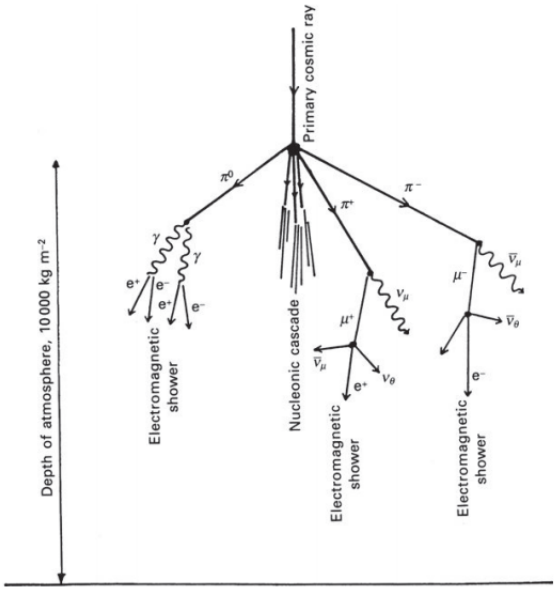

Figure 2.11: Graphical representation of possible decay channels of intial cosmic ray. Picture taken from (Longair, 2011).

Electromagnetic showers: Another mechanism by which positrons are created are electromagnetic showers. This happens when a high energy photon interacts with the field of nucleus. In brief: energetic photons penetrates the atmosphere and generates a pair, each of which creates high energy photon by bremsstrahlung, each of which creates a pair and so on (Longair, 2011).

Photon-photon collisions: It is possible for pair to be created in a photon-photon interaction. The treshold for this reaction is:

$$\epsilon_2 \geqslant \frac{m_e^2 c^4}{\epsilon_1} = \frac{0.26 \times 10^{12}}{\epsilon_1} \text{ eV} \tag{2.48}$$

Pair annihilation can occur in two ways. The first possibility is for electron and positron to annihilate at rest or in flight and the reaction is:

$$e^+ + e^- \rightarrow 2\gamma \tag{2.49}$$

Each photon will have an energy of 511 keV, provided they are emitted at rest. If, on the other hand, collision is fast (particles interact "in-flight"), there's going to be a dispersion in energy of photons. Photon that moves off in the direction of incoming positron will carry most of energy of the positron. The energy is defined by relation:

$$E = \frac{m_e c^2 (1+\gamma)}{2}\left(1 \pm \frac{V}{c}\right) \tag{2.50}$$

where γ is Lorentz factor. Equation 2.50 is also setting a lower limit to the energy of photon ejected in the direction opposite of $\frac{m_e c^2}{2}$.

In a situation when the velocity of positron is small, annihilation can occur through formation of positronium[10]. The bound state of this system has two possible configurations. The singlet state $1\,^1\mathrm{S}_0$, called para-positronium (p-Ps) decays predominantly into *two* photons with a lifetime in vacuum of $\tau_{\mathrm{p-Ps}} = 125$ ps . Triplet state $\left(1\,^3\mathrm{S}_1\right)$, called ortho-positronium, decays predominantly into *three* photons with a lifetime in vacuum of $\tau_{0-\mathrm{Ps}} = 142.05$ ns (Badertscher et al., 2007). Photons created through a decay of para-positronium each have energies of 0.511 MeV. In case when three gamma-ray photons are formed, maximum energy[11] is 0.511 MeV and the spectrum will be continuous, to the low

[10] Positronium can be defined as a bound state of electron and positron.
[11] in the center of momentum frame.

side of 511 keV line Longair (2011). This is used as a diagnostic aid in understanding the origin of 511 keV line. Environmental requirement for positronium formation is a neutral medium with particle density less than 10^{21} m^{-3}. If temperature of medium (gas) exceeds 10^6 K, annihilation will occur directly (without formation of positronium).

Pair annihilation spectra can be described by a power-law and an example is given in Fig. 2.12. For different approximations, various values of power law indices were obtained, and the interval is $2.0 < \alpha < 3.0$ (Boettcher and Schlickeiser, 1996).

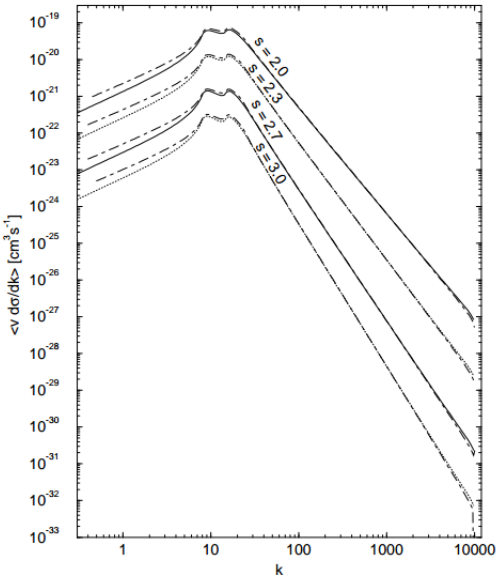

Figure 2.12: Pair annihilation spectra calculated by the asymptotic approximation (dashed) compared to numerical integrations (solid and dotted, respectively) for different γ parameters. Spectral index has values in the interval from $2.0 < \alpha < 3.0$. Taken from (Boettcher and Schlickeiser, 1996). Spectral index notation is changed from s to α in order to be consistent in this work.

Evolution of this power-law spectrum is given in Fig. 2.13. Two cases are presented: the one where medium is electron-dominated plasma 2.13a and where densities of electrons and positrons are equal, as well as their distribution functions 2.13b. A significant diversity of influence on spectrum can be noted, depending on environment parameters.

2.2.9 Dark Matter annihilation

Cosmological model (ΛCDM)[12] in which about 23 % of Universe is composed of unknown form of non-baryonic matter, called *Dark Matter (DM)*, is widely accepted today. Particle physics beyond the Standard Model proposes many DM candidates, most of which are the self-annihilating particles. The product of such annihilation reactions are standard particles (quarks, leptons and W bosons) and gamma-photons. Gamma-ray spectrum (Figure 2.14) of such events is a continuous one and has several features. The spectral features predicted are a cut-off (for $E = m_{\mathrm{DM}}$) and spectral hardening (that will depend on the proposed DM particle mass).

The search for DM candidate can be done from various angles and it is being conducted in particle physics (collider physics), in scattering experiments and in astrophysics. Astrophysical approach involves a detection of by-product of annihilation reaction, that is - gamma-ray photons. Astrophysical objects and structures where the annihilation signal is being looked for are dwarf galaxies, galaxy clusters and DM clumps in galaxy halos. Gamma-ray emission from Galaxy center is also a proposed location; however, it is extremely hard to distinguish a DM signal from other gamma-emitters located there.

[12]This segment is taken from (Paiano, 2014).

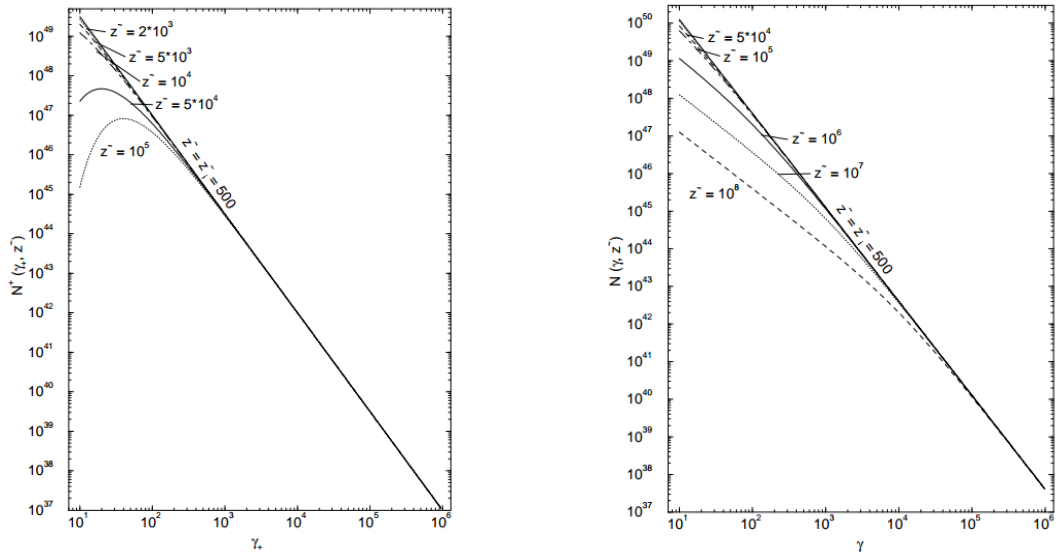

(a) **(b)**

Figure 2.13: Evolution of power-law particle energy spectrum influenced by pair annihilation losses. (a) Case of electron-dominated plasma and (b) Case when electrons and positrons have the same density and distribution functions. Taken from (Boettcher and Schlickeiser, 1996).

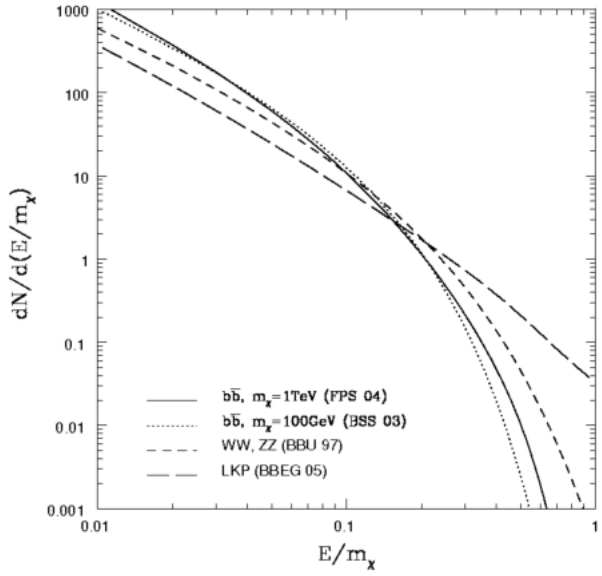

Figure 2.14: Dark matter spectrum. Spectrum is continuous with a cut-off at $E = m_{\mathrm{DM}}$. Picture is taken from (Paiano, 2014)

2.3 Gamma-ray sources

As explained in the section above, gamma-ray emission is due to processes that are non-thermal in nature and involve presence of intense magentic fields and various particle acceleration mechanisms. Sources of gamma-rays are divided into **galactic** and **extragalactic** ones.

Galactic sources

Galactic gamma sources are further divided into two categories: point-like and extended. The study of extended galactic sources is as useful as it is important: apart from information about their emission, we are able to study their morphological properties. Investigation of extended sources also incorporates the study of the soruce environment (as it is connected to its emission). Emission of point-like sources is associated to relativistic particle flows and jet formation. Astrophysical objects that belong to galactic source class are:

- **Pulsars (PSR)**
- **Supernova Remnants (SNr)**
- **Binary systems and MicroQuasars**
- **Pulsar Wind Nebulae (PWNe)**

We will briefly describe pulsars as they are investigated in this work. Pulsars are neutron stars with extremely small radius (~ 10 km) and mass of $\sim 1.4 M_{\odot}$. Therefore, they are extremely compact objects. They are also rapidly rotating stars: their rotational period is of the order of seconds or miliseconds. Lastly, they are characterized by strong magnetics fields, up to $\sim 10^{13} - 10^{15}$ G. Therefore, particles that interact with pulsar's intense magnetic fields, are accelerated and will emit synchrotron and IC radiation which will be detected in radio to gamma band. Emission is collimated along the magnetic field axis (which is not aligned to rotational axis).

On average, pulsars have a flat spectrum with a cut-off. Cut-off is either above a few GeV (if the primary gamma-rays are produced close to magnetic poles) or above 100 GeV (if the gamma emission is produced in a region far from the star). The models that describe these two cut-offs are *polar cap model* and *outer gap model*, respectively. Pulsars are the most populous galactic class in HE gamma band. A light curve of most famous pulsar, Crab pulsars, is given in Fig. 2.2.1

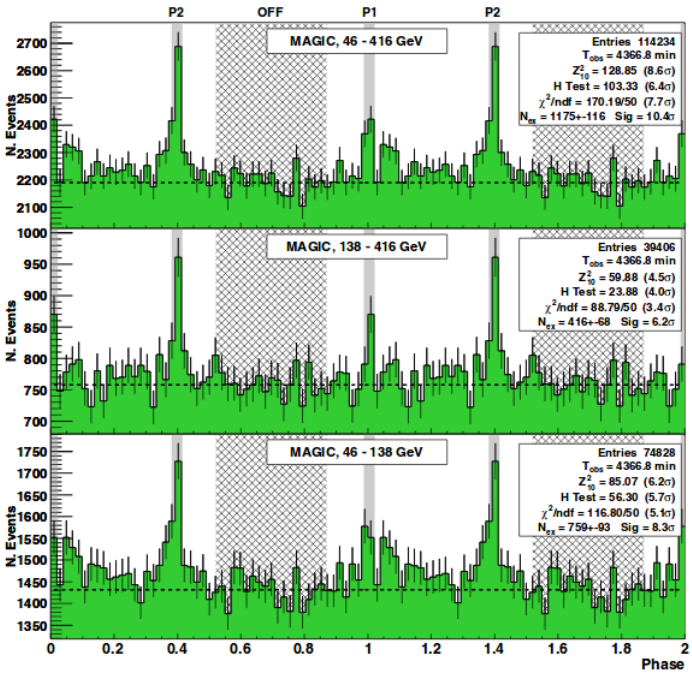

Figure 2.15: Light curves of the Crab pulsar. Picture taken from (Aleksić et al., 2012)

Extragalactic sources

There are two classes of extragalactic sources:

- **Gamma-ray bursts (GRB)**
- **Active galactic nuclei (AGN)**

Two classes that were analyzed in this work (flat spectrum radio quasars and BL Lacs) belong to AGN category. In a nutshell, AGN is a compact central region of galaxies that is emitting substantial amount of energy. Radiation from AGN is non-thermal, highly variable and is emitted throughout the whole spectrum. Many objects are classified as AGN, based on their morphological, optical or other properties (Fig. 2.16). This leads into a very complicated taxonomy which makes AGN category one of the most "confused and confusing" fields (Blandford et al., 1990).

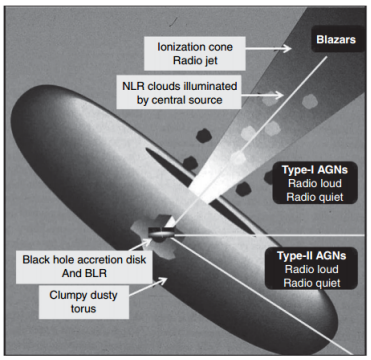

Figure 2.16: Side view of AGNs showing the main ingredients of a unification scheme. Picture taken from (Netzer, 2013).

In order not to make already complicated things more complicated, we present AGN classification diagram in Fig. 2.17. From this scheme, we see that our objects of interest (FSRQ and BL Lacs) belong to blazar subclass that is radio-loud. In the next paragraph we will provide brief important properties of each blazar class.

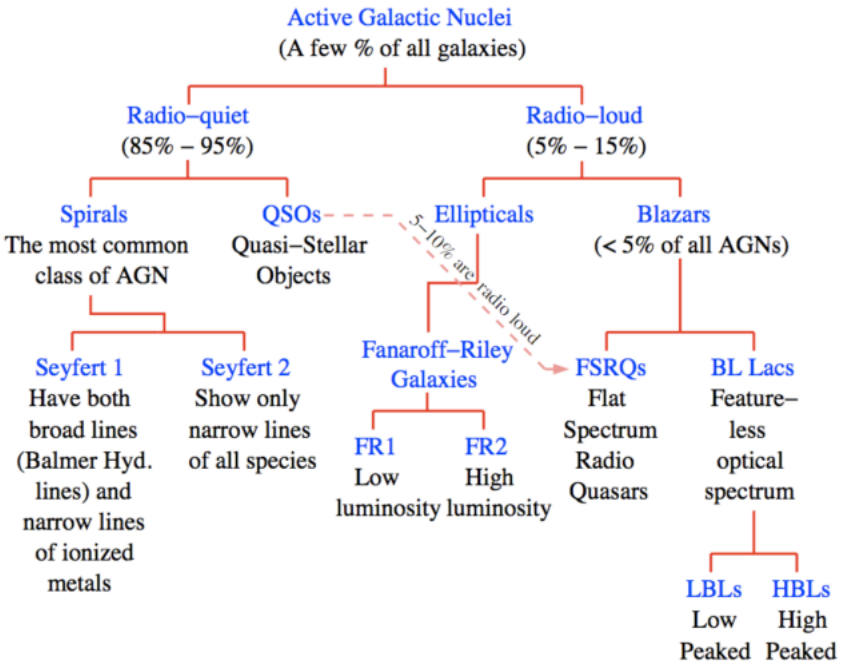

Figure 2.17: AGN classification diagram. Picture taken from (Paiano, 2014).

Blazars are AGN class that is detected in gamma regime. These radio-loud sources are extremely variable at all frequences. They are characterized by high level of polarization in radio and optical and by compact core. All these attributes are due to the relativistic beaming of jet radiation when jet axis is close to our line of sight (as it can be seen in Fig. 2.16). Blazar emission is dominated by the continuum emission of the jet, which is non-thermal as already mentioned. Their spectral energy distribution (SED) has a specific, double-bump[13] shape (typical for SSC process) and extends from radio to gamma. SED examples can be seen in Fig. **??**. Bolometric luminosity of these objects is in the range from $\sim 10^{42}$ to $10^{4}8$ erg $\cdot$ s^{-1}. Extreme brightness is explained by a process in which gravitational energy is released by accretion onto a black hole (BH). A formation of accretion disk is possible and it is seen as a powerful way of energy dissipation and carry the angular momentum (Paiano, 2014). Formation of jets is possible, given certain conditions. Jet physics and physics of accretion disks is very complicated field and is not part of this work. What we will mention is that material can be expelled in highly collimated jets and if the jets are aligned to our line of sight (Los) (more or less), we will see these objects as radio-loud blazars.

Blazars are, therefore, compact, point-like sources characterized by jet emission where jet is aligned to our LoS. They are further divided into **radio-quasars** and **BL Lac objects**. Radio quasars are usually hosted by elliptical galaxies and their optical spectrum has broad lines. BL Lacs lack any emission lines or their lines are extremely weak. Their flux is very variable. The lack of emission lines in BL Lacs is still uder a debate; some possible explanations can be found in (Stein et al., 1976).

In general, studying AGN is one of the tasks of modern astrophysics as they are objects whose activity dictates galaxy evolution, star formation and other cosmologically important processes.

[13] "camel-hump"

Chapter 3

The Third Fermi LAT point source catalog

NASA's Fermi is a space mission whose main scientific goal is whole sky survey in the energy range from $\sim$ 20 MeV to more than 300 GeV. Instrument on board is Large Area Telescope (LAT) that, apart from energy measurment, also measures the arrival times, direction of radiation and the background radiation (Acero et al., 2015). Instrument's field of view (FoV) is 2.4 sr at 1 GeV. "LAT is a pair-conversion detector and its calorimeter and tracker consist of 4 $\times$ 4 array of 16 modules, segmented anticoincidence detector and triger and aquisition system." (Atwood et al., 2009). Tracker is made out of layers of silicon-strip detectors and tungsten foil. Silcon strips are use to track charged particles while tungsten foil aids in conversion of gamma-rays to pair electron-positron. Calorimeter is a CsI 8 layer detector. Anticoincidence detector is a plastic scintilator read out by photomultiplier.

Data of 3FGL was taken in the period from 4 August 2008 (15:43 UTC) to 31 July 2012 (22:46 UTC). Data is publicly available at FERMI. Improvements w.r.t. Second Fermi catalog (2FGL) can be found described in detail in (Ackermann et al., 2015) paper. We will briefly touch upon the catalog itself. 3FGL has 3034 sources. Out of 3034 sources, 1011 are unassociated. Sources are associated using the Automated Source Association (in this method, data is compared to other catalogs, listed in Table 12 of the 3FGL paper). List of source classes in 3FGL is given in Fig. 3.1.

Description	Identified		Associated	
	Designator	Number	Designator	Number
Pulsar, identified by pulsations	PSR	143	...	...
Pulsar, no pulsations seen in LAT yet	...	...	psr	24
Pulsar wind nebula	PWN	9	pwn	2
Supernova remnant	SNR	12	snr	11
Supernova remnant / Pulsar wind nebula	...	...	spp	49
Globular cluster	GLC	0	glc	15
High-mass binary	HMB	3	hmb	0
Binary	BIN	1	bin	0
Nova	NOV	1	nov	0
Star-forming region	SFR	1	sfr	0
Compact Steep Spectrum Quasar	CSS	0	css	1
BL Lac type of blazar	BLL	18	bll	642
FSRQ type of blazar	FSRQ	38	fsrq	446
Non-blazar active galaxy	AGN	0	agn	3
Radio galaxy	RDG	3	rdg	12
Seyfert galaxy	SEY	0	sey	1
Blazar candidate of uncertain type	BCU	5	bcu	568
Normal galaxy (or part)	GAL	2	gal	1
Starburst galaxy	SBG	0	sbg	4
Narrow line Seyfert 1	NLSY1	2	nlsy1	3
Soft spectrum radio quasar	SSRQ	0	ssrq	3
Total	...	238	...	1785
Unassociated	...	...	...	1010

Figure 3.1: LAT 3FGL Source Classes. Designation "spp" is an indication of potential association with Supernova Remnant (SNR) or Pulsar Wind Nebula (PWN). Picture of this table is taken from (Acero et al., 2015).

58 % of all 3FGL sources are AGN. Apart from main catalog (3FGL), there are many supporting catalogs such as 3LAC (The Third Catalog of Active Galactic Nuclei Detected by the Fermi Large

Area Telescope, (Ackermann et al., 2015)) and tools provided. Each source is designated 3FGL JHHMM.m+DDMM where the 3 indicates that this is the third LAT catalog, FGL represents Fermi Gamma-ray LAT. Some sources have "c" added at the end of their Fermi name as an indication they should be taken with caution (since they are detected in the overcrowded Galactic plane region).

It can be seen (Fig. 3.1) that some designations are in capital letters and some are in lower case. The lower case designators indicate associations while capital letters indicate firm identifications. The catalog is available online, in FITS format, at: https://fermi.gsfc.nasa.gov/ssc/data/access/lat/4yr_catalog/. Catalog column descriptions are given in Fig. 3.2.

Column	Description
Name	`3FGL JHHMM.m+DDMM[c/e/i/s]`, constructed according to IAU Specifications for Nomenclature; `m` is decimal minutes of R.A.; in the name, R.A. and Decl. are truncated at 0.1 decimal minutes and 1′, respectively; `c` indicates that based on the region of the sky the source is considered to be potentially confused with Galactic diffuse emission; `e` indicates a source that was modeled as spatially extended (see § 3.4); the two spectral components of the Crab PWN are designated `i` and `s`
R.A.	Right Ascension, J2000, deg, 3 decimal places
Decl.	Declination, J2000, deg, 3 decimal places
l	Galactic Longitude, deg, 3 decimal places
b	Galactic Latitude, deg, 3 decimal places
θ_1	Semimajor radius of 95% confidence region, deg, 3 decimal places
θ_2	Semiminor radius of 95% confidence region, deg, 3 decimal places
ϕ	Position angle of 95% confidence region, deg. East of North, 0 decimal places
σ	Significance derived from likelihood Test Statistic for 100 MeV–300 GeV analysis, 1 decimal place
F_{35}	Photon flux for 1 GeV–100 GeV, 10^{-9} ph cm^{-2} s^{-1}, summed over 3 bands, 1 decimal place
ΔF_{35}	1σ uncertainty on F_{35}, same units and precision
S_{25}	Energy flux for 100 MeV–100 GeV, 10^{-12} erg cm^{-2} s^{-1}, from power-law fit, 1 decimal place
ΔS_{25}	1σ uncertainty on S_{25}, same units and precision
Γ_{25}	Photon number power-law index, 100 MeV–100 GeV, 2 decimal places
$\Delta\Gamma_{25}$	1σ uncertainty of photon number power-law index, 100 MeV–100 GeV, 2 decimal places
Mod.	`PL` indicates power-law fit to the energy spectrum; `LP` indicates log-parabola fit to the energy spectrum; `EC` indicates power-law with exponential cutoff fit to the energy spectrum
Var.	`T` indicates < 1% chance of being a steady source; see note in text
Flags	See Table 3 for definitions of the flag numbers
γ-ray Assoc.	Positional associations with 0FGL, 1FGL, 2FGL, 3EG, EGR, or 1AGL sources
TeV	Positional association with a TeVCat source, `P` for unresolved angular size, `E` for extended
Class	Like 'ID' in 3EG catalog, but with more detail (see Table 6). Capital letters indicate firm identifications; lower-case letters indicate associations
ID or Assoc.	Designator of identified or associated source

Figure 3.2: LAT Third Catalog description. Picture is taken from (Acero et al., 2015) (Table 5. in the paper).

In case a source has problematic characteristic or unusual one, a flag is assigned. There are several types of flags and their description can be found in Table 3. of the 3FGL paper. Finally, a full sky map with all sources (by source class) mapped is given in Fig. 3.4. The blow-up of the inner Galactic region is given in Fig. 3.3.

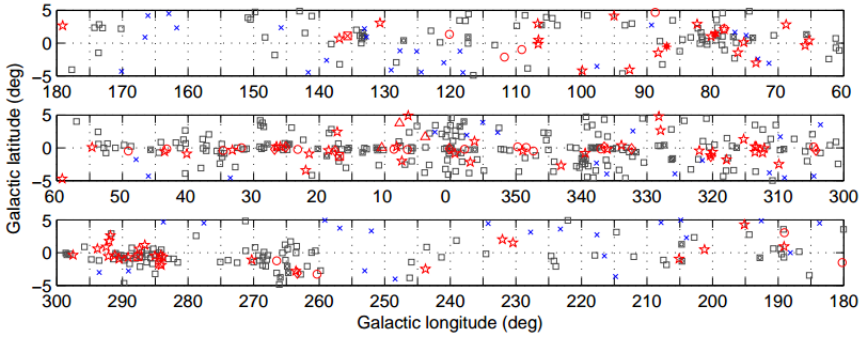

Figure 3.3: Blow-up of the inner Galactc region. Picture is taken from (Acero et al., 2015).

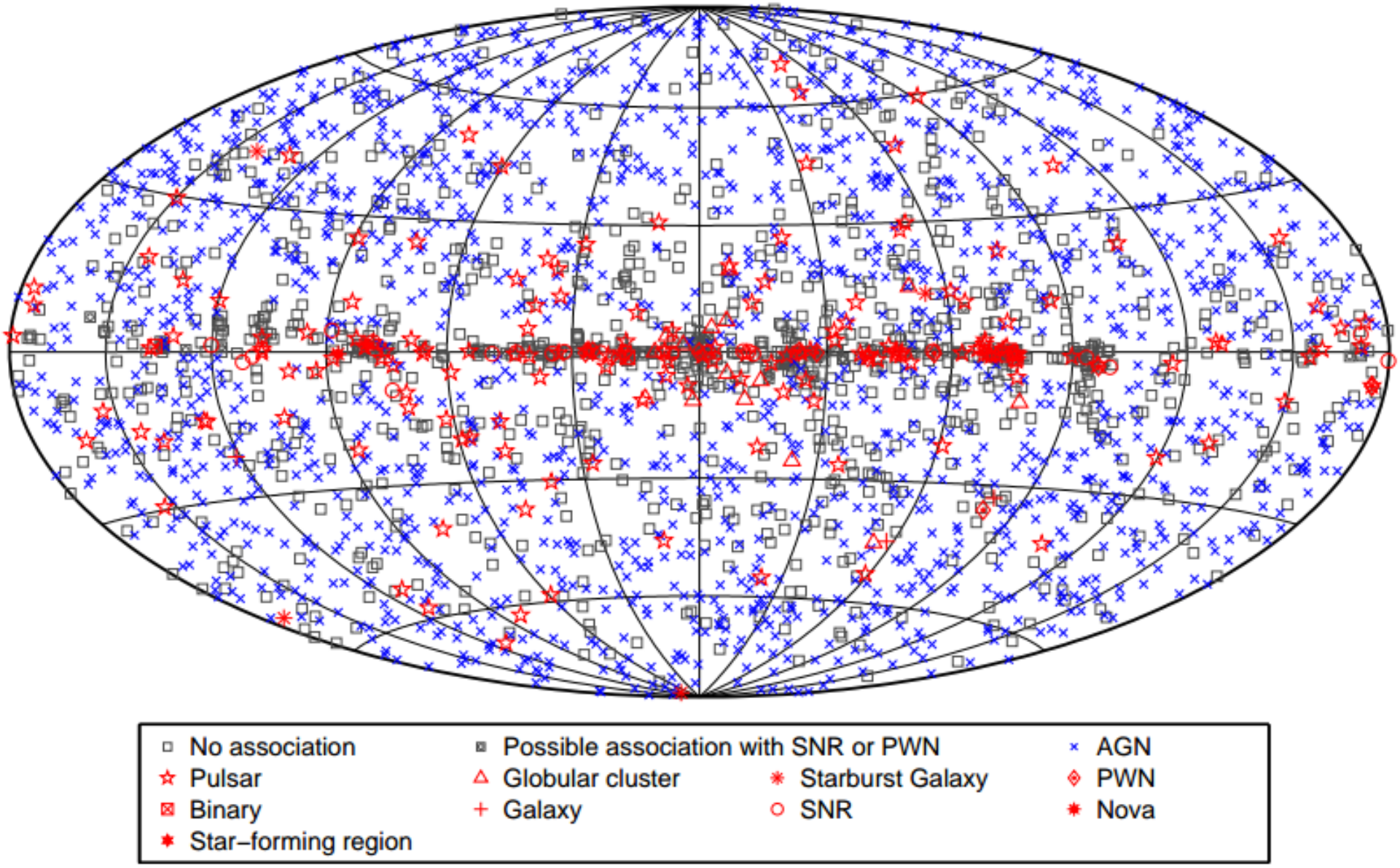

Figure 3.4: FERMI full sky map with all sources marked. Different source classes are indicated in the legend below the map. Picture is taken from (Acero et al., 2015).

Chapter 4

Data

In this chapter we will briefly explain how our sample was chosen and the steps we took to process the data. The first step was to decide which sources we will chose in our study. Our sample consits of 5 types of gamma-ay emitters and they are listed in Table 4.1

Table 4.1: Sources from The Third Fermi Catalog chosen in this work

Source type	Number of sources
BL Lacs	660
FSRQ	484
BCU	573
UFO	1011
PSR	167

Third Fermi LAT catalog was downloaded in FITS format from FERMI. All other Fermi producst used in this work (such as 2PC, 2LAC and 3LAC catalogs) were downloaded from the same website. Apart from Fermi data, we also extensively used information available from ASI Data Science Center (ASI) in order to cross-correlate the data. Files in FITS format were further handled using fv (Pence and Chai) and TOPCAT (http://www.star.bris.ac.uk/ mbt/topcat/sun253/ack.html) editors.

The first task of this work was to obtain general statistical properties of selected classes of sources. In order to o that, we chose several parameters listed in 3FGL and plotted histograms for each. These parameters are listed in Table 4.2 and the results are analyzed in Ch. §**??**.

Table 4.2: List of quantities available in 3FGL for which we plotted histograms and performed statistical analysis in Ch. §**??**

Parameter	Parameter
Galactic latitude	Spectral index
Photon Flux	Variability index
Energy flux	Redshift

The second part of this thesis required a construction of color-color diagrams. For this, we selected certain information primarily available in 3FGL (some data was collected from other Fermi catalogs) in order to calculate ratios of fluxes in radio, optical, X and gamma bands. Tabulated parameters used to obtain fluxes for AGN class were: `flux_xray`, `flux_radio`, `Vmag_USNOB1`, `spectral_index`, `pivot_energy` and `flux_density`. PSR class fluxes were calculated using `G_100`, `S_1400`, `XFlux_NonTherm` and `Corr_OptFlux` parameters. All quantities were converted to have the same dimension. After that, data was processed using python with numpy, scipy and seaborn libraries. Results were plotted with matplotlib. For contours in plots, KDE function from seaborn library was used (bivariate kernel density estimation).

Chapter 5

Analysis of selected gamma-ray sources: statistical properties

In this chapter, we are preforming a statistical analysis of selected gamma-ray emitter classes. Parameters (tabulated in 3FGL) analyzed are: *galactic latitude, photon flux, energy flux, spectral index, variability index* and *redshift*. As explained in (§**??**), a histogram for each quantity and for each object class was constructed and is presented in subsequent sections.

5.1 Galactic latitude

Galactic latitude b is a crucial parameter because it gives a position of the source. In astrophysical terms, celestial distribution of a certain class of object is indicative and can be related to many factors: cosmological, evolutive, etc. Therefore, galactic latitude can be used as a base for constructing a theory and scientific interpretation. Position of FERMI sources is extremely important, especially for AGN class. Classification of AGN is a complicated task but it always requires a mutiwavelength approach, which further puts an emphasis on significance of position.

Distribution of position of sources depending on their galactic latitude is presented in Fig. 5.1. Galactic latitude is plotted on abscissa while ordinate represents the number of sources. All catalogued sources for classes: BCU, BLL, FSRQ and PSR are used in a plot. Class with unknown association (UFO) is subdivided into two categories, using the $|b| > \pm 20^\circ$ criterion. Histograms of galactic latitude do not inlcude the UFO subclass with objects whose galactic latitude values fall into $|b| < \pm 20^\circ$ category. These objects are plotted separately in Fig. 5.3. Basic parameters of histograms for galactic latitude is given in Table 5.1. Each object category is treated separately in following subsections. However, the feature present in distribution (Fig. 5.1) is an asymmetry above and below Galactic plane. There is a slightly higher number of sources in northern hemisphere of associated sources. At the same time, the number of UFOs is higher in the southern hemisphere. This was addressed by FERMI collaboration and their explanation is that this is not due to some intrinsic property of classes. The reason behind the discrepancy is the fact that counterpart catalogs FERMI uses in the automatic association procedure are more extensive for positive latitudes.

Table 5.1: Parameter values for galactic latitude histogram given in Fig. 5.1

Object class	Number of sources	Number of bins
BLL	660	20
FSRQ	484	20
BCU	573	20
UFO $\|b\| > \pm 20^\circ$	380	20
UFO $\|b\| < \pm 20^\circ$	630	20
PSR	167	20

Among all classified sources in 3FGL catalog, **BL Lacertae** objects are the most numerous. The first characteristic of latitude distribution of BL Lacs is the asymmetry in numbers in north and south hemisphere (Fig. 5.2a). This issue is discussed in paragraph above. There is also present a significant

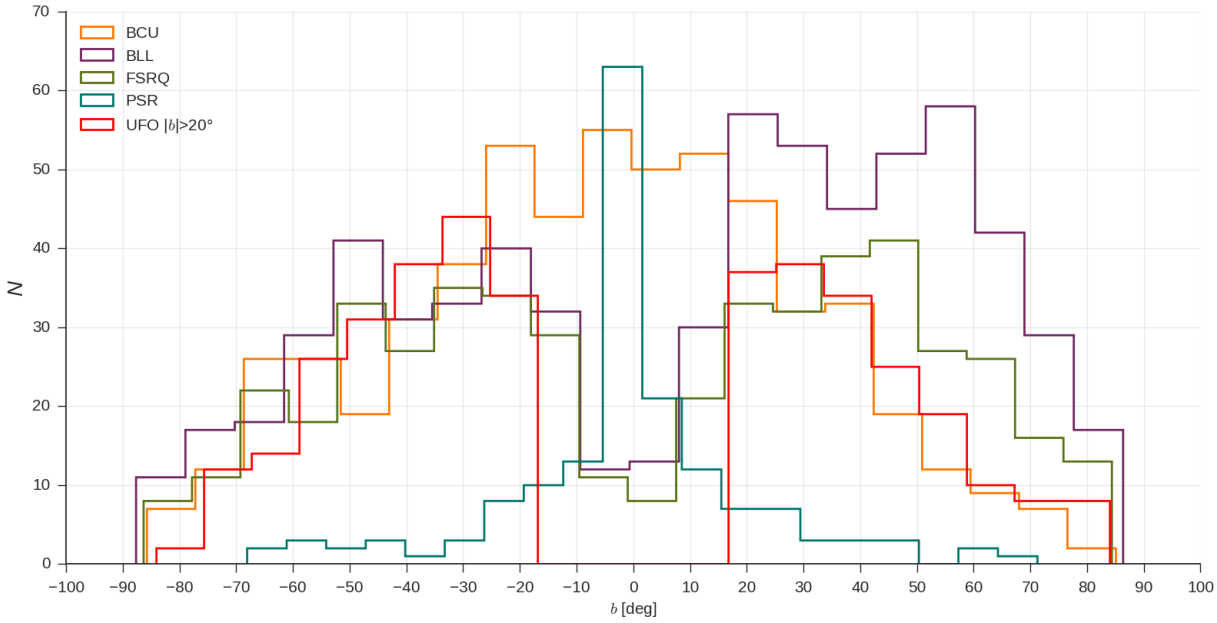

Figure 5.1: Histogram of galactic latitudes for different classes of objects

lack of these sources at low latitudes, specifically in the $\pm 10°$ region. The reason is of course not of "cosmological" or of any other nature but simply because of discussed confusion in the Galactic plane. In the northern hemisphere, in the interval between $\sim 35°$ and $\sim 55°$, a slight drop in BL Lacs can be seen. If compared to distribution of FSRQs at the same latitudes, a correlation can be made. However, an astrophysical reason behind cannot be established by us at this point. In the southern hemisphere, a higher frequency of BL Lacs is at $\sim -20°$ and $\sim -50°$. There are also very few objects at the highest negative latitudes.

Flat spectrum radio quasars show slightly higher degree of symmetry in distribution in hemispheres when compared to other classes (Fig. 5.2b). Expected drop in numbers in the problematic $\pm|10°|$ region is present. Low population can be seen in $\sim -70°$ to $\sim -90°$ interval as well. Highest frequency is between 35° and 50°. In the southern region, higher number can be seen between $\sim -25°$ and $\sim -35°$ and $\sim -45°$ and $\sim -50°$. A significant drop (when compared to "local" distribution, not all latitudes) can be seen between $-50°$ and $-60°$, as well as between $\sim -35°$ and $\sim -45°$.

Latitude distribution of **blazar candidates of uncertain type (BCU)** is given in Fig. 5.2c. The highest number of these blazar candidates is at low latitudes, especially at 0° and $-20°$. Overall, the concentration in the Galactic plane (in the region from $\sim -30°$ to $\sim 30°$) is the highest. This is to be expected due to already discussed ambiguities. Another noticable feature is the considerable drop in numbers at latitudes from $-40°$ to $-50°$. This can be explained by comparing the distribution of BCU to distributions of BL Lac and FSRQ population, given in Fig. 5.2a and Fig. 5.2b, respectively. In both blazar categories, their number is higher at exactly these latitude values. The same can be used to interpret the lower frequency of BCU in norther hemisphere, in interval from 40° to 90°.

More than half (57%) **Unassociated Fermi Objects** can be found in the Galactic plane, as expected. The highest frequency is around 0°. Interestingly, their number at $\pm|10|\circ$ is very low (Fig. 5.3). UFO sources outside the zone of avoidance (Fig. 5.2d) show "smoother" distribution than classified sources (i.e. the number of sources decreases from Galactic plane outwards smoothly). As mention above, there are more unassociated objects in the southern hemisphere. Also, there are more UFOs in the interval from 75° to 80° than in its southern counterpart.

Pulsars are, by far, a population that is the highes in frequency in the Galactic plane (out of associated ones, that is). Distribution is condensed towards the plane (Fig. 5.4). The reason behind this is the fact that these are galactic sources so their parameters are well known and studied. Numbers after $\pm|30°|$ are very low. The other noticable feature is a complete lack of sources detected in 50° to 60° interval. No other significant features are present.

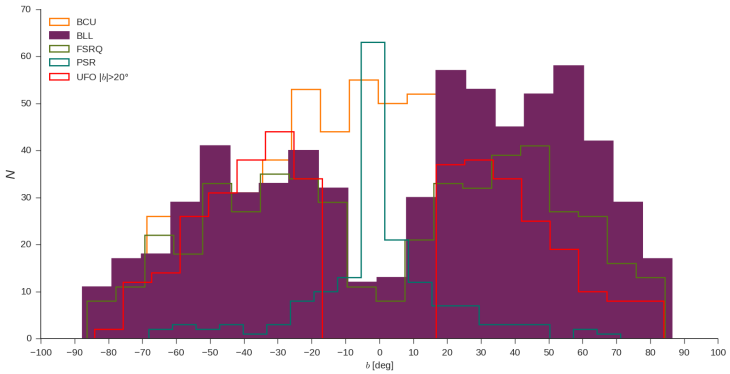

(a) Galactic latitude histogram for 3FGL BL Lac objects.

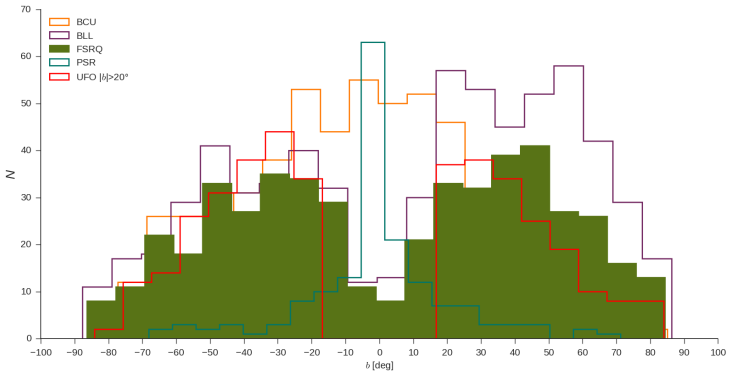

(b) Galactic latitude histogram for 3FGL FSRQ objects.

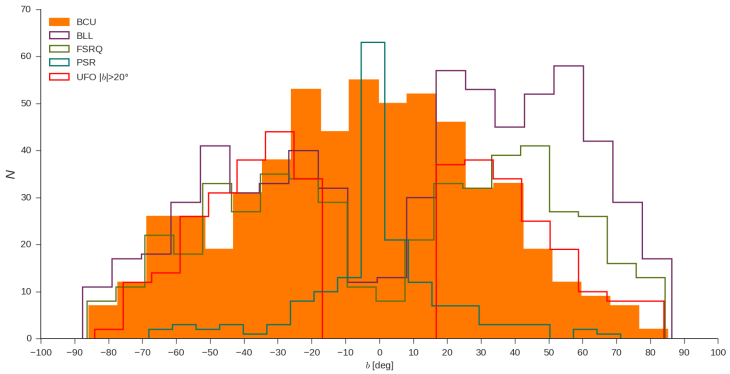

(c) Galactic latitude histogram for 3FGL BCU objects.

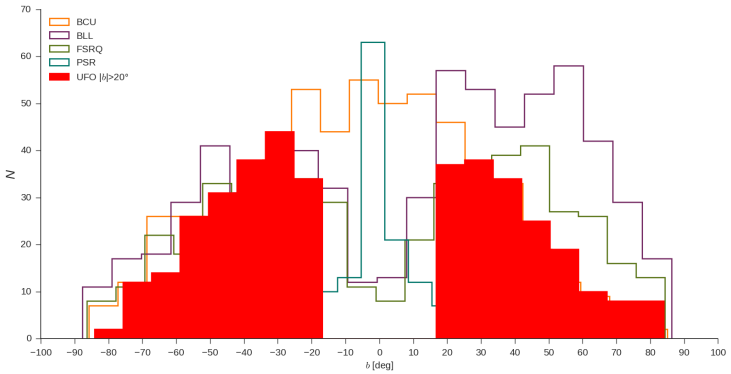

(d) Galactic latitude histogram for 3FGL UFO objects.

Figure 5.2: Galactic latitude distribution for blazar class. Galactic latitude is plotted on abscissa while ordinate represents the number of objects.

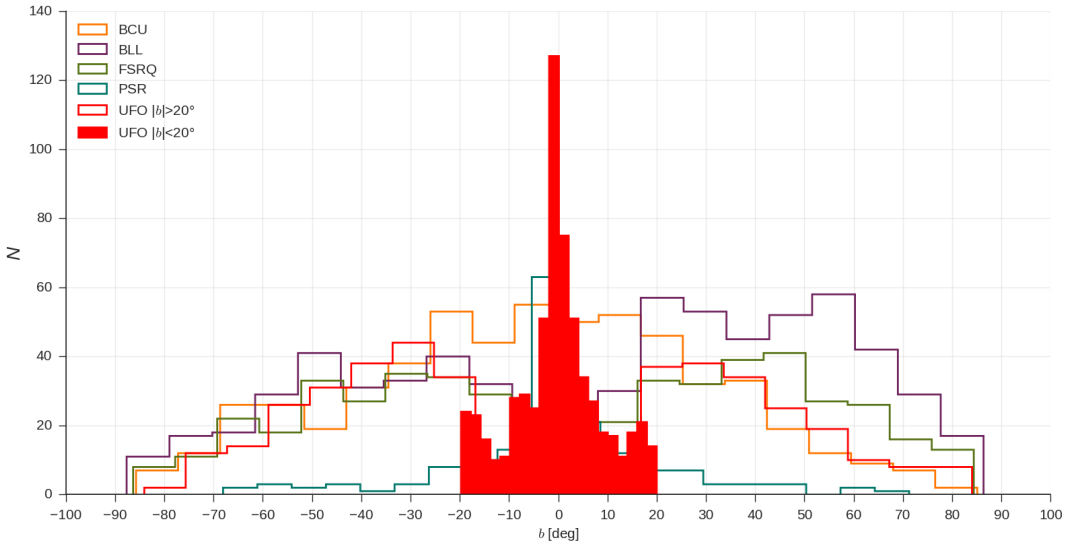

Figure 5.3: Histogram of galactic latitudes for UFO in the range $|b| < \pm 20°$.

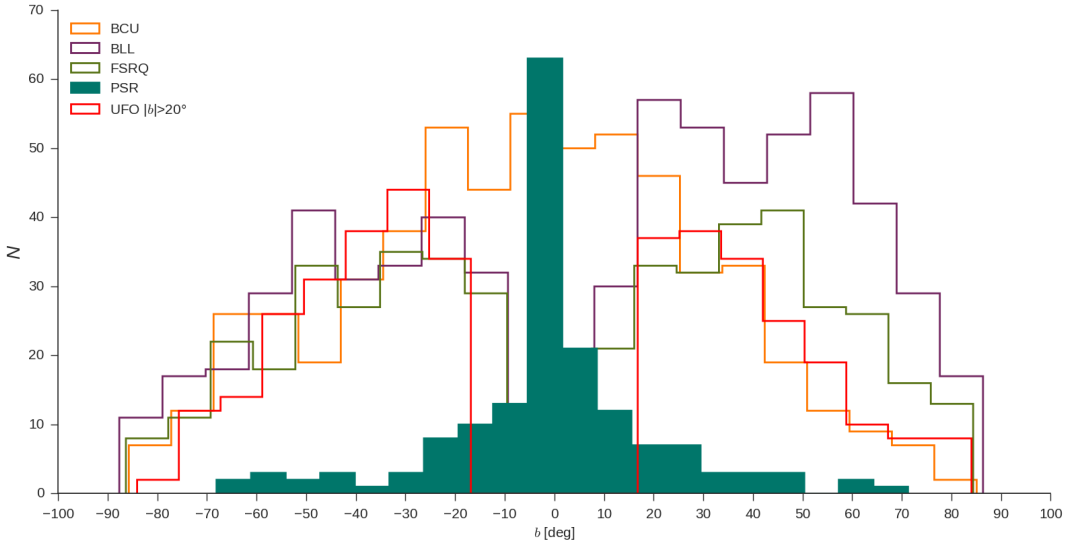

Figure 5.4: Histogram of galactic latitudes for PSR

5.2 Photon flux

Photon flux is another important quantity that we examined. Photon flux is defined as number of photons per unit area per time. It depends on distance of an object and on its intrinsic flux. Analyzing which class is emitting most photons and how many photons on average we can expect can be used a good statistical tool in various investigations.

Histogram for photon flux for selected source categories is given in Fit. 5.5. Since we included different classes of sources in the study, photon flux values are very spread. Therefore logarithmic value of photon flux is plotted on abscissa. Y-axis represents the number of sources. Histogram[1] parameters are given in Table 5.2. Distribution is given in Fig. 5.5 and subsequent histograms are the same with difference being the filled-in bars for better visibility. Each class is anaylized separately in following segments. The common characteristic is a slight asymmetry of the distribution in favor of higher photon count for extragalactic sources.

Table 5.2: Parameters for photon flux distribution of selected classes, given in Fig. 5.5

Object class	Number of sources	Number of bins
BLL	660	15
FSRQ	484	15
BCU	573	15
UFO	380	15
PSR	167	15

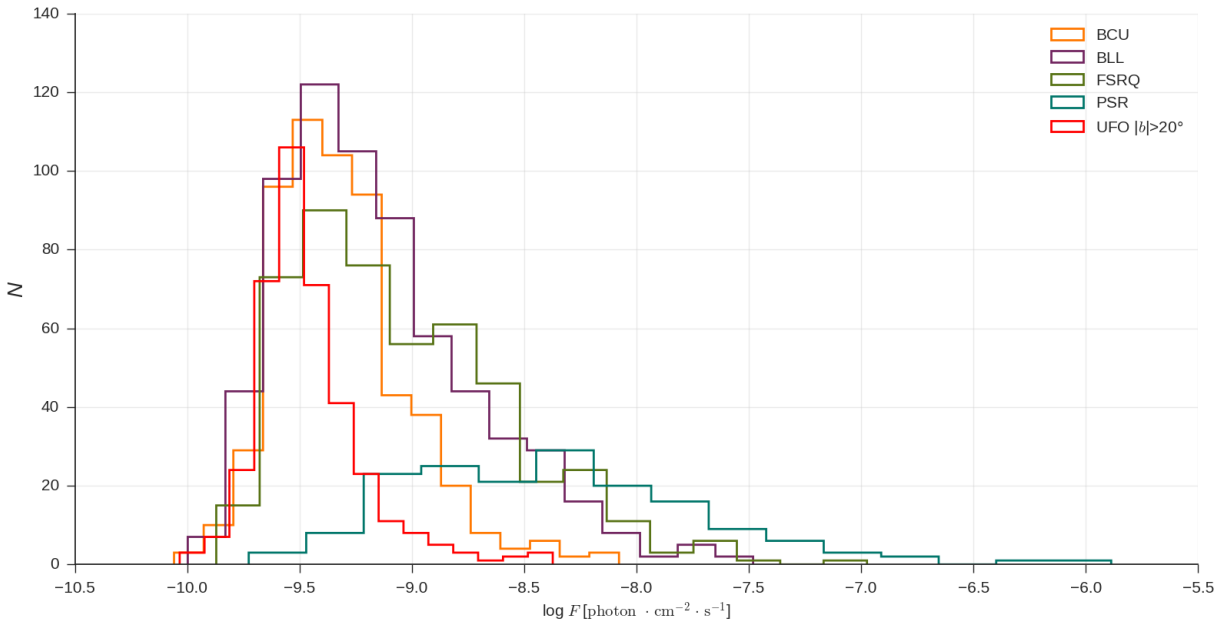

Figure 5.5: Histogram of photon flux for different classes of objects

BL Lacertae objects have photon flux in the range from 10^{-10} to 3.3×10^{-8}. We noticed majority of BL Lacs emit in interval from $\log F \sim -9$ to ~ -9.7 photons per unit area per second. Flux of -9.5 photons $\cdot\, \mathrm{cm}^{-2} \cdot \mathrm{s}^{-1}$ is the flux of the peak of the distribution. As in previous case, there is an asymmetry of the distribution with larger number of BL Lacs having higher flux. Visual representation is given in Fig. 5.6a.

Flat spectrum radio quasar class emits photons in the range from 1.35×10^{-10} to 1.1×10^{-07} per unit area and unit time (Fig. 5.6b). That is one order of magnitude more than BL Lacertae category. Also, the interval where most of FSRQs emit the most photons is wider than that of BL Lac.

[1] for all histograms in this section.

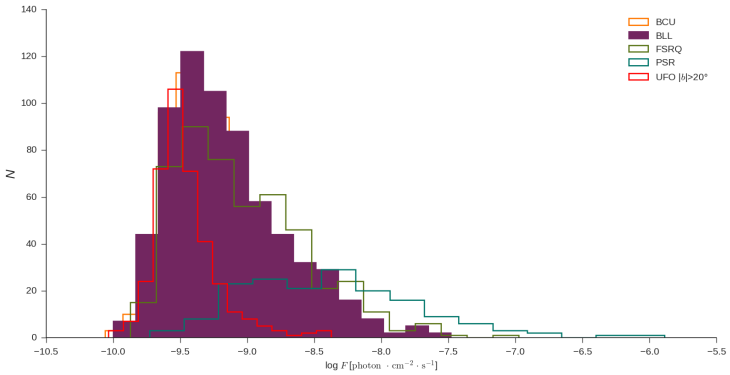

(a) Photon flux histogram for 3FGL BL Lac objects.

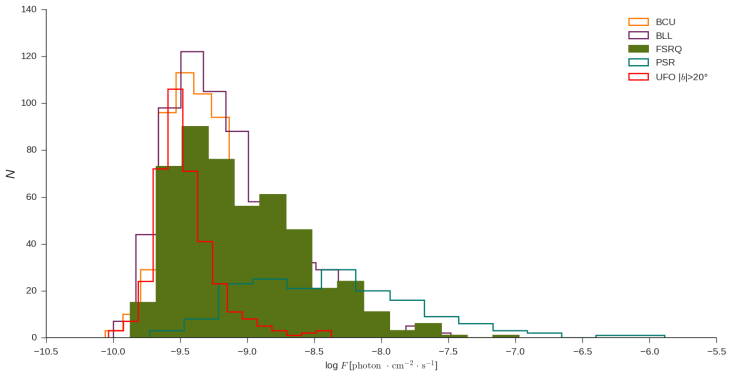

(b) Photon flux histogram for 3FGL FSRQ objects.

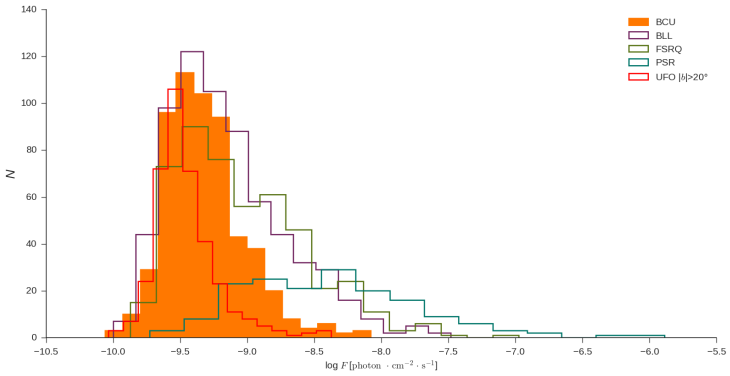

(c) Photon flux histogram for 3FGL BCU objects.

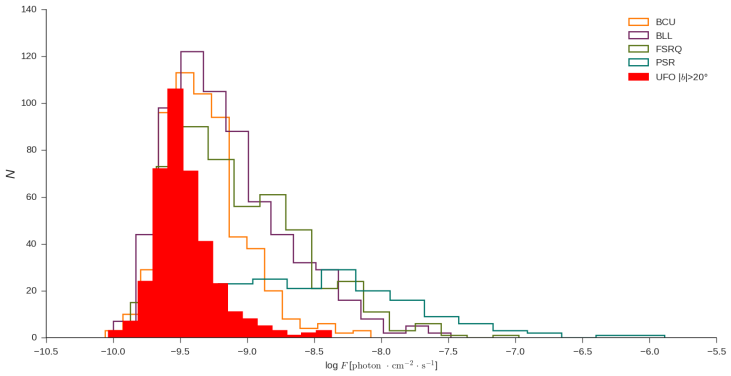

(d) Photon flux histogram for 3FGL UFO objects.

Figure 5.6: Photon flux distribution for blazar class. Photon flux is plotted on abscissa while ordinate represents the number of objects.

Interesting feature are three "jumps" in frequency of sources for photon fluxes concentrated at $\log F \sim -8.3$, -8.7 and -9.4 photons per second per unit area. The trend where there are more objects that emit more photons is present here as well.

Photon flux of **blazar candidates**, plotted in Fig. 5.6c spans over approximately two magnitudes: from 8.73×10^{-11} to 8.36×10^{-9} photons $\cdot\, \mathrm{cm}^{-2} \cdot \mathrm{s}^{-1}$. The majority of sources have photon flux in the interval from $\log F \sim -9.2$ to -9.7 ph. $\cdot\, \mathrm{cm}^{-2} \cdot \mathrm{s}^{-1}$ with most of them emitting $\log F \sim -9.5$ photons per second per area. We also noticed that BCU that emit more photons are more numerous. Photon flux of BCU category falls into bins of known blazar types (Fig. 5.6a and 5.6b).

Unidentified Fermi sources have photon flux in the interval from $9.3{\times}10^{-11}$ to $4.2{\times}10^{-9}$ ph. $\cdot\, \mathrm{cm}^{-2} \cdot \mathrm{s}^{-1}$ (Fig. 5.6d). The interval of photon flux where majority of sources emit is the shortest out of all sampled classes. It ranges from $\log F \sim -9.4$ to ~ -9.7 [ph. $\cdot\, \mathrm{cm}^{-2} \cdot \mathrm{s}^{-1}$]. The distribution peaks at exactly $\log F = -9.5$ ph. $\cdot\, \mathrm{cm}^{-2} \cdot \mathrm{s}^{-1}$. Asymmetry in distribution can be seen and, as in previous cases, sources that emit less photons are lower in number. Majority of UFO photon flux falls into blazar bins. Smaller percentage falls into PSR bins. This could be used as an indication of class (of course, with great caution).

The first characteristic about **pulsar** photon flux distribution (Fig. 5.7) is that it is higher on average than that of other classes sampled. It spans over four orders of magnitude, from 1.9×10^{-10} to 1.3×10^{-6} photons $\cdot\, \mathrm{cm}^{-2} \cdot \mathrm{s}^{-1}$. The interval where majority of pulsars are emitting photons goes from $\log F \sim -7.7$ to ~ -9.3 photons per unit time and area. Highest frequency[2] of pulsars emit around $\log F \sim -8.4$ photons per second per unit area. There is also an increase in number of pulsar emitters for photon flux of $\log F \sim -8.8$ photons $\cdot\, \mathrm{cm}^{-2} \cdot \mathrm{s}^{-1}$. The explanation of higher pulsar photon flux lies in the fact they are galactic sources so the distance to objects is responsible.

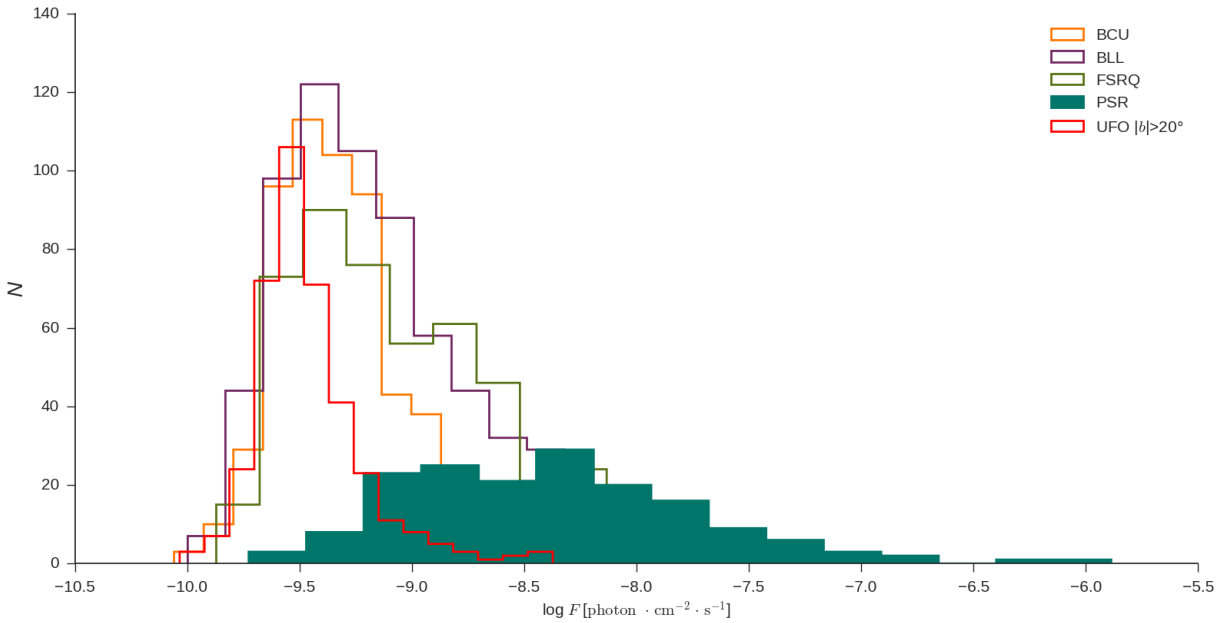

Figure 5.7: Histogram of photon flux for PSR

[2]by frequency we are referring to number of pulsars.

5.3 Energy flux

Energy flux is defined as energy emitted per unit time per unit area. It depends on luminosity and distance (decreases following inverse square law). As it is one of the fundamental parameters for studying emitters, gathering statistics is not only helpful but also required.

Distribution of energy fluxes of our sample is presented in Fig. 5.8. Histogram parameters are given in Table 5.3. Logarithmic values of energy flux is plotten od x-axis. Ordinate represents the number of objects. Common characteristics is, again, a slight asymmetry and each distribution is analyzed in following segments.

Table 5.3: Distribution parameters for histogram depected in Fig. 5.8

Object class	Number of sources	Number of bins
BLL	660	15
FSRQ	484	15
BCU	573	15
UFO	380	15
PSR	167	15

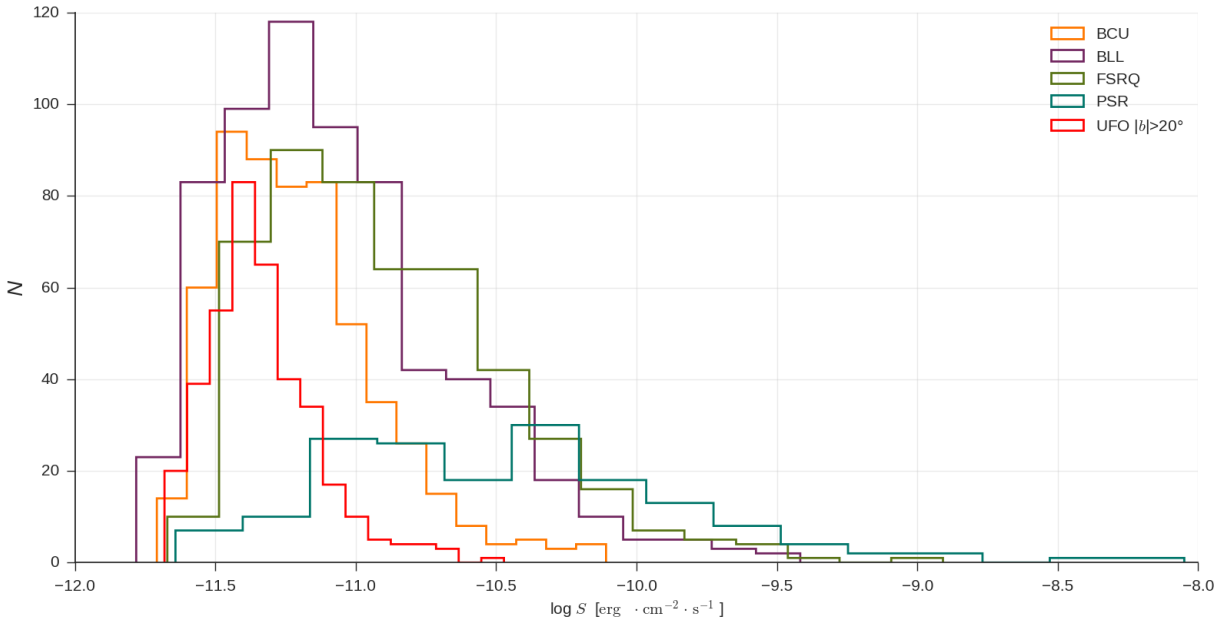

Figure 5.8: Histogram of energy flux for different classes of objects

3FGL energy flux of **BL Lacertae** sources is in two order of magnitude interval: from 1.65×10^{-12} to 3.8×10^{-10} erg $\cdot$ cm$^{-2} \cdot$ s^{-1}. Distribution is given in Fig. 5.9a. The range is which majority of sources are radiating is wide ($\log S \sim -11.6$ to -10.8 erg $\cdot$ cm$^{-2} \cdot$ s^{-1}). Distribution peaks around $\log S \sim -11.3$ erg $\cdot$ cm$^{-2} \cdot$ s^{-1} and is asymmetric with same properties as described before. BLL noticabely have a population for which the interval from $\log S \sim -10.8$ to ~ -10.4 erg $\cdot$ cm$^{-2} \cdot$ s^{-1} is significant.

Flat spectrum radio quasars have very wide energy flux range (Fig. 5.9b): it spans from 2.1×10^{-12} to 1.2×10^{9} erg $\cdot$ cm$^{-2} \cdot$ s^{-1}. That is 3 orders of magnitude. The interval where majority FSRQs emit is from $\log S - 11.5$ to ~ -10.6 erg $\cdot$ cm$^{-2} \cdot$ s^{-1}. The peak is at around $\log S - 11.2$ erg $\cdot$ cm$^{-2} \cdot$ s^{-1}. The asymmetry is present and can we noticed an absence of sources from -9.3 to -9.1 erg $\cdot$ cm$^{-2} \cdot$ s^{-1}.

Energy flux of **BCU** (Fig. 5.9c) spans from 1.9×10^{-12} to 7.8×10^{-11} erg $\cdot$ cm$^{-2} \cdot$ s^{-1}. Majority of BCUs have energy flux between $\log S \sim -11.5$ and ~ -11 erg $\cdot$ cm$^{-2} \cdot$ s^{-1}. Distribution peaks around $\log S \sim -11.4$ erg $\cdot$ cm$^{-2} \cdot$ s^{-1}. The asymmetry trend is present here.

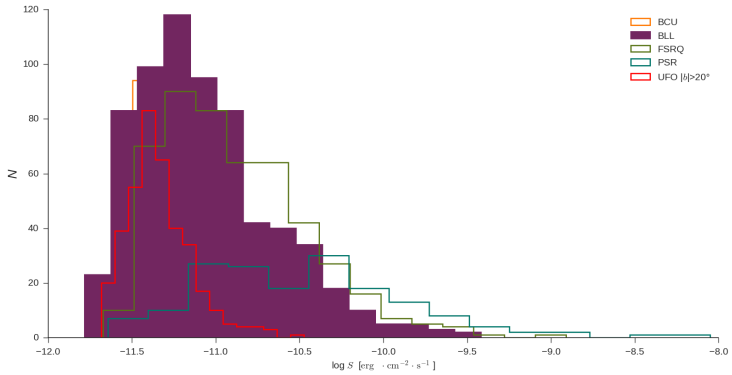

(a) Energy flux histogram for 3FGL BL Lac objects.

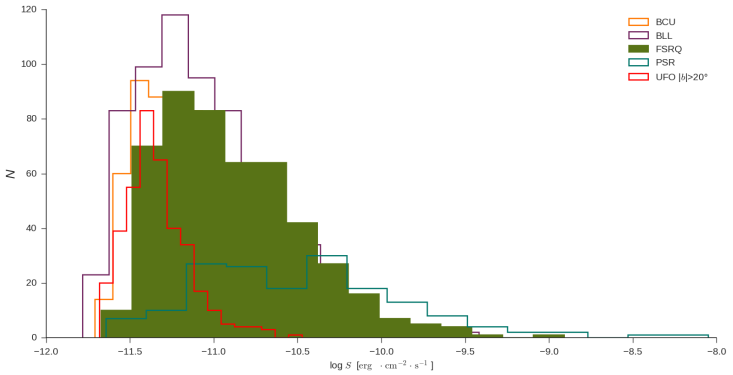

(b) Energy flux histogram for 3FGL FSRQ objects.

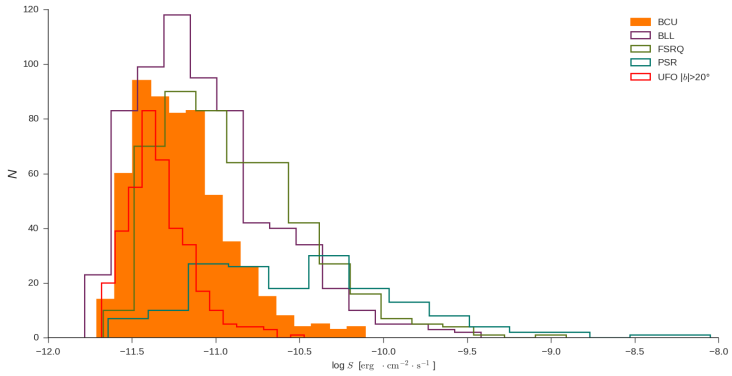

(c) Energy flux histogram for 3FGL BCU objects.

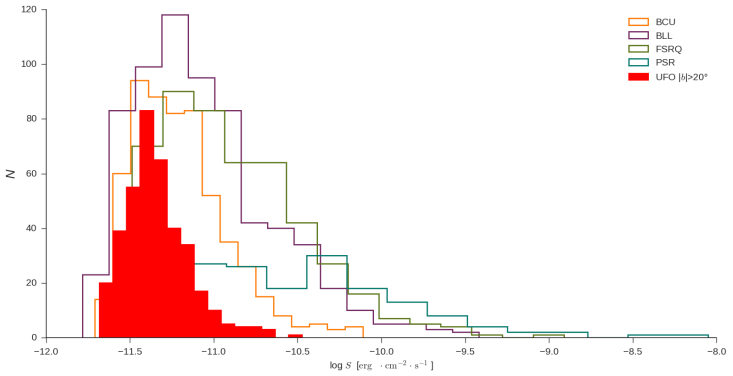

(d) Energy flux histogram for 3FGL UFO objects.

Figure 5.9: Energy flux distribution for blazar class. Energy flux is plotted on abscissa while ordinate represents the number of objects.

Unassociated Fermi objects have tighter distribution (Fig. 5.9d) compared to other classes. They span from 2.1×10^{-12} to 3.4×10^{-11} erg $\cdot$ cm^{-2} $\cdot$ s^{-1}. Their distribution shows a higher level of symmetry and peaks at about $\log S = -11.4$ erg $\cdot$ cm^{-2} $\cdot$ s^{-1}. UFO bins fall into bins of blazar classes as well to pulsar class.

Pulsars, although few in number, have energy flux distribution (Fig. 5.10) at higher values. This can be explained by their location/distance. The range of fluxes in which these compact objects emit covers three orders of magnitude: from 2.3×10^{-12} to 8.9×10^{-9} erg $\cdot$ cm^{-2} $\cdot$ s^{-1}. There are two peaks of distribution: one is positioned around $\log S = -11$ and the other at approximately -10.4 erg $\cdot$ cm^{-2} $\cdot$ s^{-1}. We noticed a lack of pulsars detected in 3FGL that emit in the $\log S \sim -8.5$ to -8.7 interval.

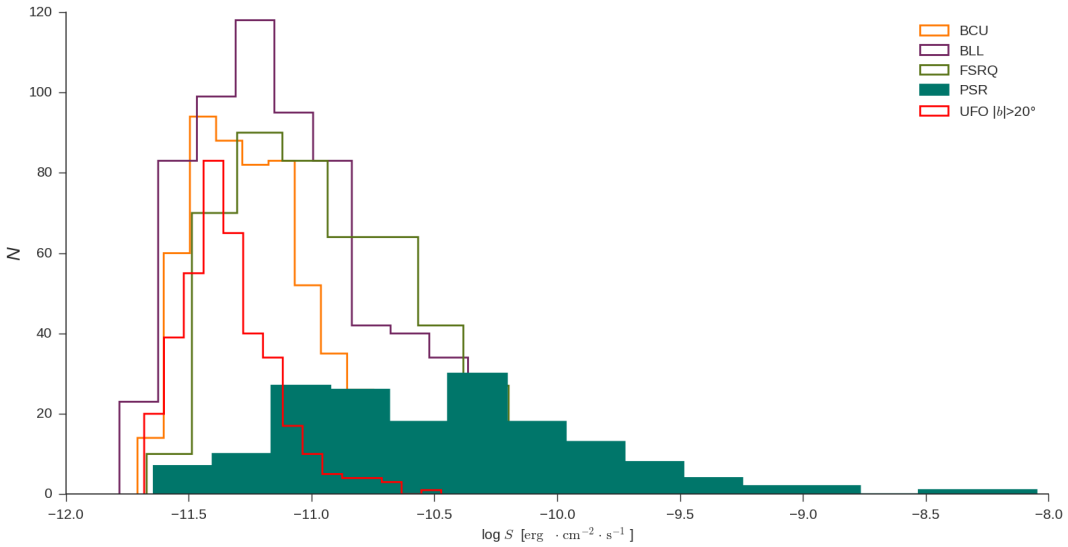

Figure 5.10: Histogram of energy flux for PSR

5.4 Spectral index

Spectral index is a crucial quantity as it represents spectrum slopes of all objects of interest to gamma-ray astronomy, as discussed in Ch. 2.2. Obtaining a better statistics of spectral index for each class provides constraints and can be used in investigations. In this section, spectral index distributions of each class are examined.

Distributions of spectral indices of all sampled classes (apart from UFO that were omitted) are constructed and are given in Fig. 5.11. Spectral indices are plotted on abscissa and ordinate represents the number of sources. Number of sources and bin sizes for each class is given in Table 5.4. Unlike previous distributions, spectral index distributions of selected classes show symmetry.

Table 5.4: Parameters for spectral index distribution of sampled classes

Object class	Number of sources	Number of bins
BLL	660	15
FSRQ	484	15
BCU	573	15
UFO	380	15
PSR	167	15

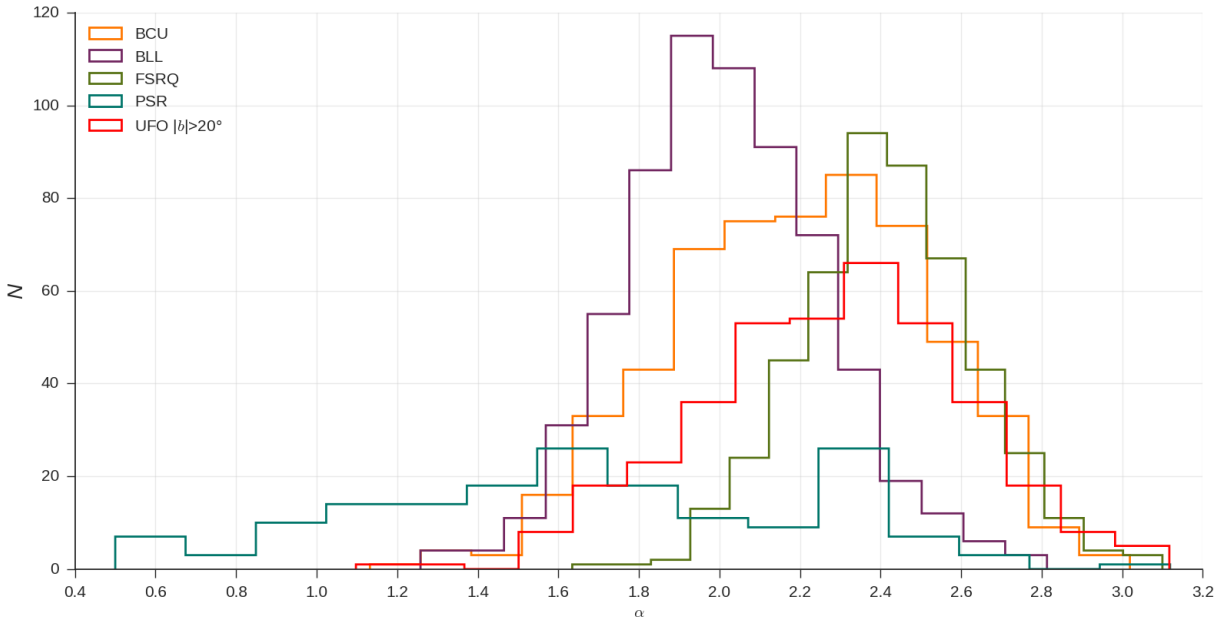

Figure 5.11: Histogram of spectral index for different classes of objects

Spectral index of **BL Lacertae** class spans from 1.26 to 2.81 (Fig. 5.11). Maximum of distribution is in the interval from 1.9 to 2.0. Distribution is symmetric.

FSRQ have overall higher values of spectral index (Fig. 5.12b) when compared to BL Lac. It covers a range from 1.63 to 3.1. Peak of distribution is at spectral index 2.4. Distribution is symmetric.

Blazar candidates of unknown type have spectral index in the range from 1.13 to 3.02. Distribution is symmetric and is given in Fig. 5.12c. Peak of distribution is in the interval from 2.3 to 2.4. Spectral index of BCU falls into known blazar bins.

Unassociated Fermi objects have spectral index distribution similiar to that of blazars 5.12d. It covers a range from 1.1 to to 3.11. We noticed that the peak of distribution matches to peak of unknown blazar class as well as flat spectrum ones ($\alpha = 2.4$). Distribution is also symmetric.

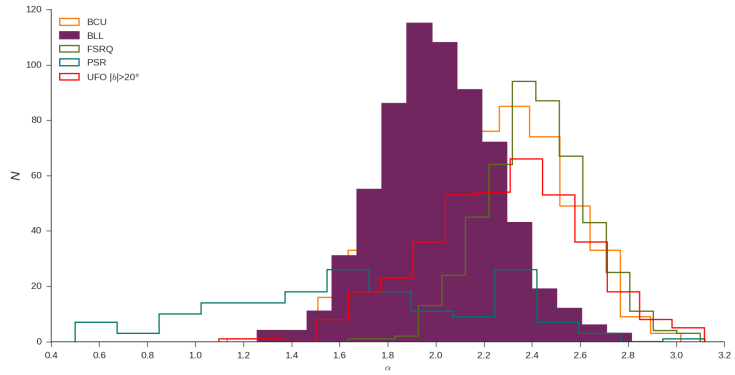

(a) Spectral index histogram for 3FGL BL Lac objects.

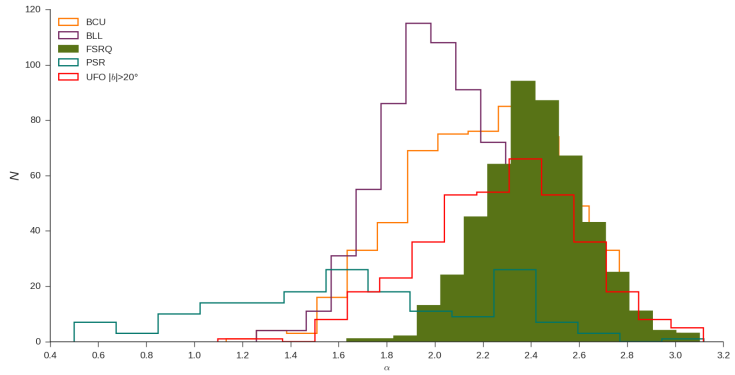

(b) Spectral index histogram for 3FGL FSRQ objects.

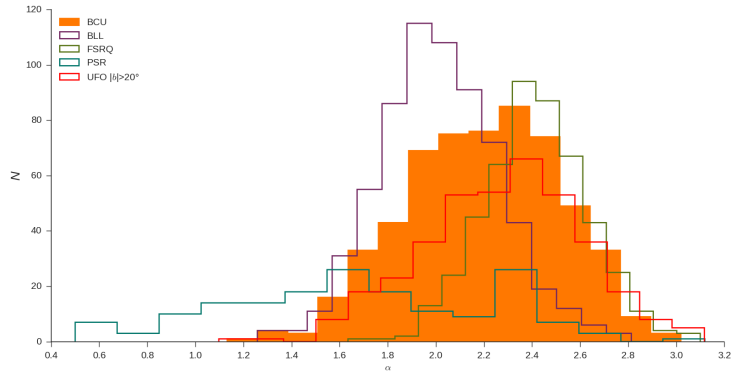

(c) Spectral index histogram for 3FGL BCU objects.

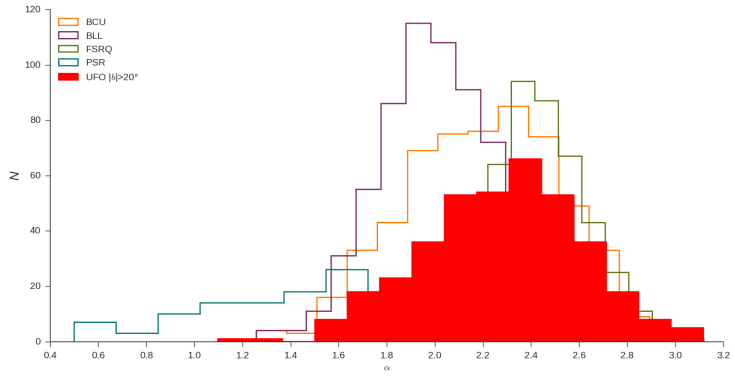

(d) Spectral index histogram for 3FGL UFO objects.

Figure 5.12: Spectral index distribution for blazar class. Spectral index is plotted on abscissa while ordinate represents the number of objects.

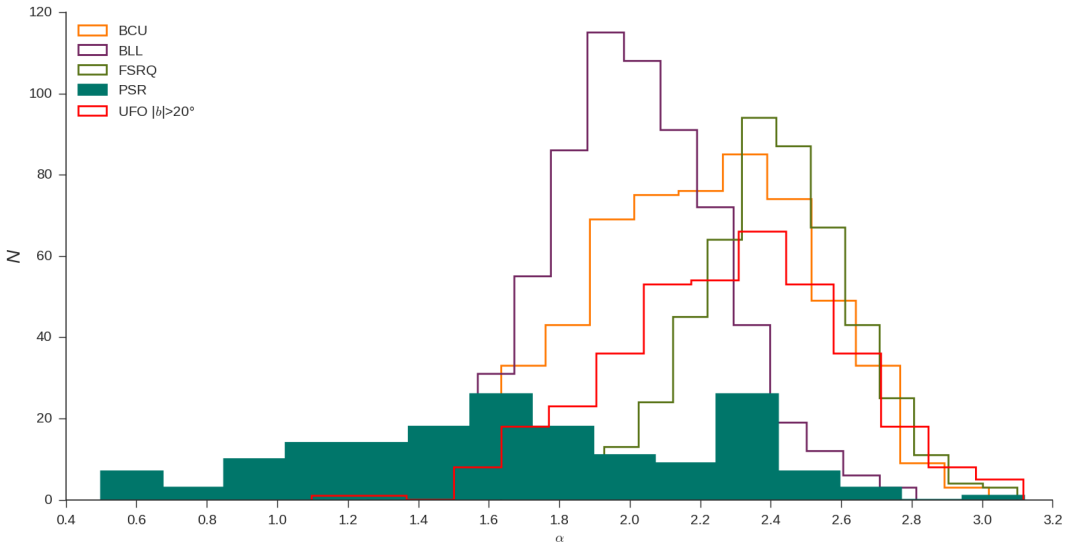

Figure 5.13: Histogram of spectral index for PSR

Histogram of spectral index values for 3FGL **pulsars** is given in Fig. 5.13. It covers a range from 0.5 to 3.11. The distribution is shifted to lower spectral index value, with peak at 1.6. We are reporting another peak at around $\alpha = 2.3$. Apart from the second peak, the distribution is symmetric. In the interval from $\alpha \sim 2.1$ to $\alpha \sim 2.9$ there is a lack of pulsar type sources.

5.5 Variability index

Another quantity which we investigated is variability index. Detailed definition on this quantity, its calculation, upper and lower limits can be found in (Nolan et al., 2012). We will just use a description for variability index: "Sum of $2 \times \log(\text{Likelihood})$ comparison between the flux fitted in 24 time segments and a flat lightcurve over the full 2-year catalog interval. A value greater than 41.64 indicates $< 1\%$ chance of being a steady source." given in (Acero et al., 2015) Table 12.

Varibility index is a useful quantity in this field as it provides am indication of the type of the source. Gamma-ray sources are known to demonstrate flux variability on long timescales. "The variability index indicates that the source is variable on a time scale of months. It does not address shorter or longer time variations. An index > 72.44 indicates a $> 99\%$ confidence probability that the source is variable." (NASA-FERMI). Values of variability index of our 3FGL sample cover extremely wide range. In order to construct the histogram, logarithmic values of variability indices were calculated and plotted on abscissa versus the number of sources of corresponding class on y-axis. The parameters are given in Table 5.5 and histogram is given in Fig. 5.14. FSRQ are by far the most variable sources while pulsars are the least variable. BL Lacs are overall less variable than flat spectrum radio quasars In-depth analysis of each class is given below.

Table 5.5: Histogram parameters for variability index of out sample

Object class	Number of sources	Number of bins	Variability index interval
BLL	660	20	24.24 to 5716.5
FSRQ	484	20	30.68 to 60733.92
BCU	573	20	22.94 to 3202.14
UFO	380	20	26.10 to 510.76
PSR	167	20	20.01 to 621.93

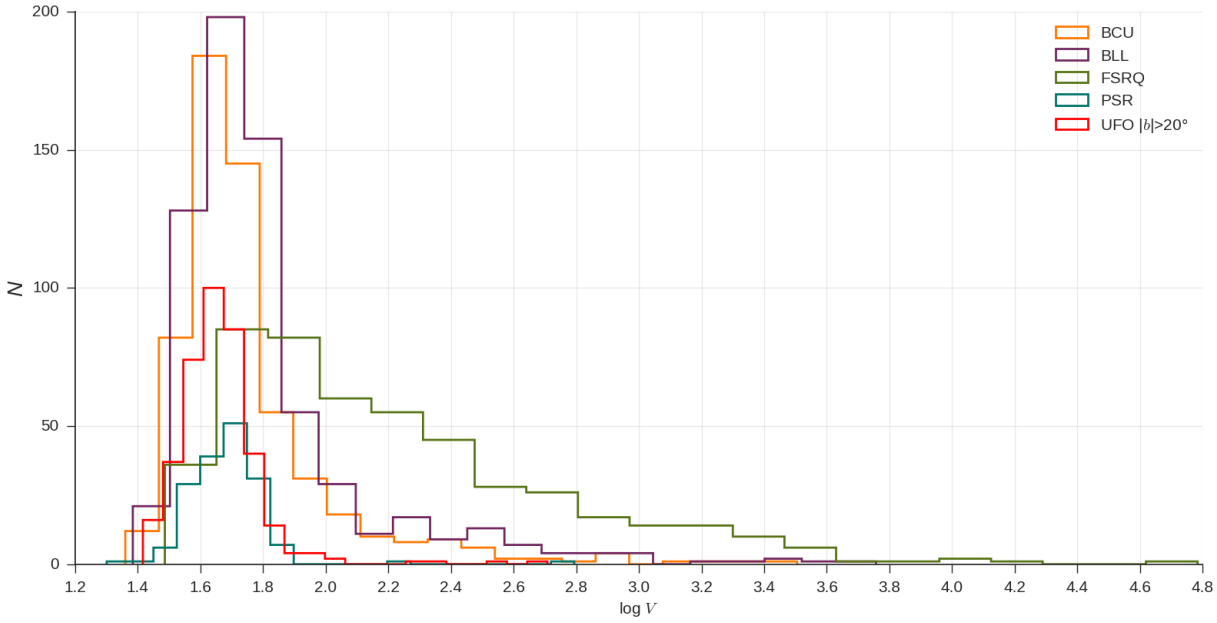

Figure 5.14: Histogram of variability index for different classes of objects

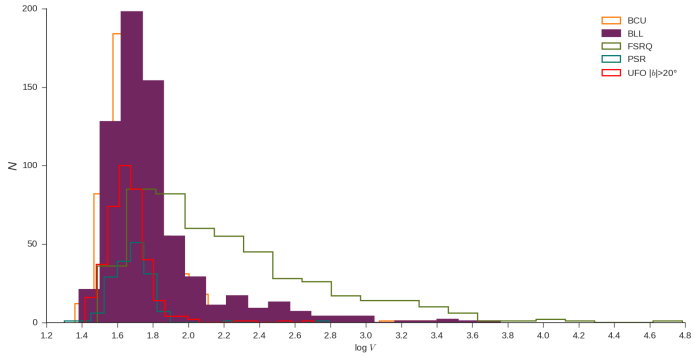

(a) Histogram for variability index for 3FGL BL Lac objects.

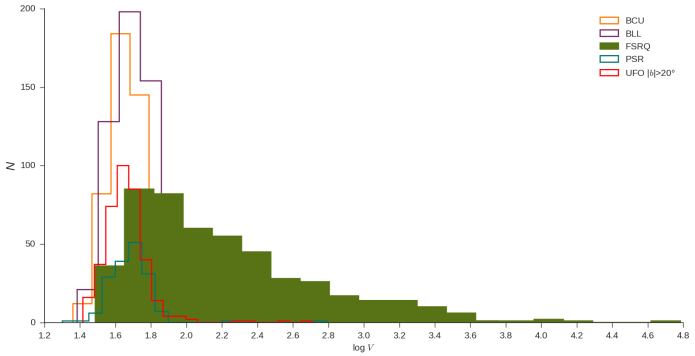

(b) Histogram for variability index for 3FGL FSRQ objects.

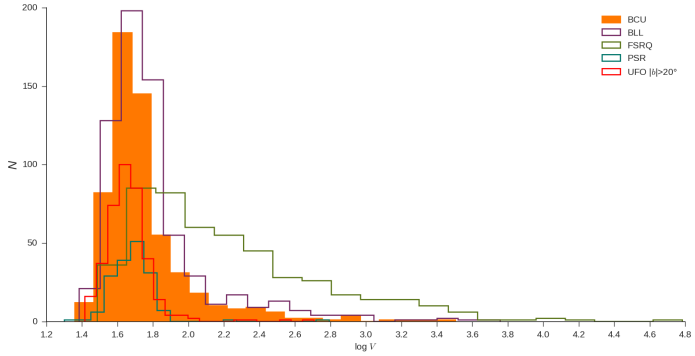

(c) Histogram for variability index for 3FGL BCU objects.

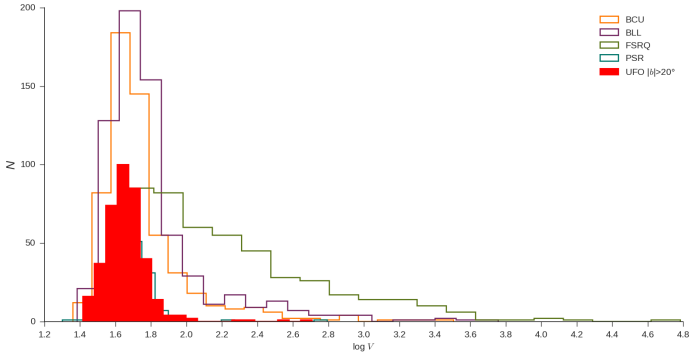

(d) Histogram for variability index for 3FGL UFO objects.

Figure 5.15: Distribution of variability index for blazar class and for 3FGL UFOs. Logarithmic values of variability index are plotted on abscissa while ordinate represents the number of objects.

BL Lacertae sources show a wide range of variability index (Fig. **??**): values span from 24.24 to 5716.5. As variability treshold is 41.64 (~ 42), BL Lac variability index less than this value indicates a quiescent stage. The peak of distribution is for $\log V \sim 1.7$ while majority of BL Lacs have variability index in the interval from $\log V \sim 1.5$ to $\log V \sim 1.9$. The asymmetry is present in this distribution.

Extreme span of variability index of **flat spectrum radio quasars** can be seen in Fig. 5.15b. It covers a range from $\log V \sim 1.5$ to $\log V \sim 4.8$. and peaking at about $\log V = 1.7$. Distribution is asymmetric as well.

Distribution of variability index of **blazars of unknown category** (Fig. 5.15c) is strikingly well matching the distribution of BL Lacs. A slight "shift" of $\log V \sim 0.05$ to lower index values is very noticable. The peak is at around $\log V = 1.6$. Asymmetry is present.

Variability index distributin of **UFOs** (Fig. 5.15d) shares interesting characteristics to that of pulsars; however, it definitely falls into blazar bins. It covers a range from $\log V \sim 1.4$ to $\log V \sim 2.7$. Distribution is symmetric in this case.

Lastly, the distribution of pulsar variability index is given in Fig. 5.16. Pulsars show much narrower distribution of index when comapred to blazars. The peak of distribution is for variability index of about $\log V = 1.7$. What is interesting in this case is the asymmetry that is the opposite of blazar distributions: there are more pulsars in lower variability index range.

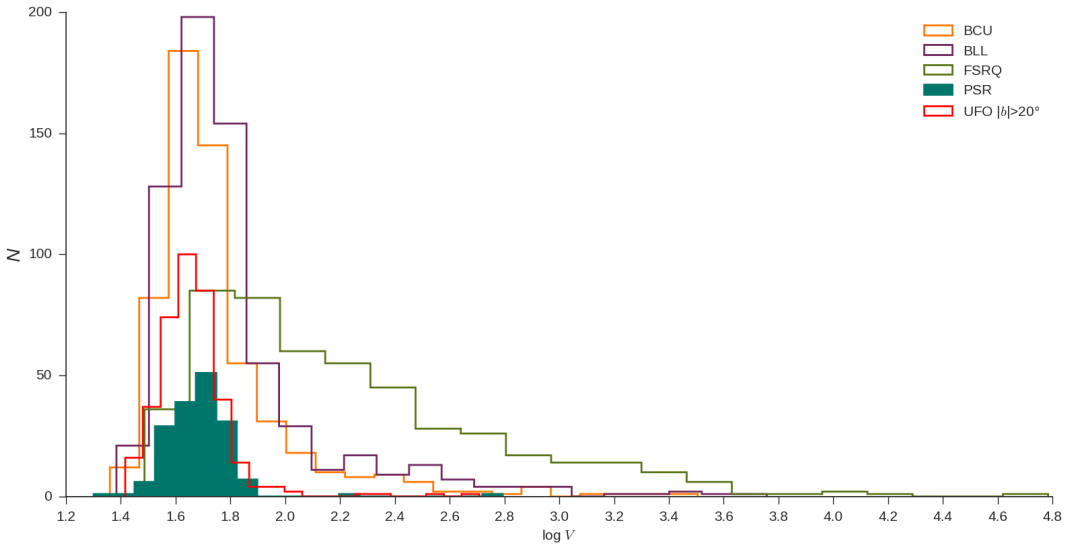

Figure 5.16: Histogram of variability index for PSR

5.6 Redshift

Redshift is a problematic, yet crucial parameter. The issue with this quantity is that in BL Lacs[3], there is an absence of strong emission lines. Therefore, it is impossible to obtain a spectroscopic redshift. Redshift determination is also problematic for lower frequences (Ajello et al., 2014a). Obtaining redshift for different AGN classes is one of the major tasks as it can be put into a cosmological context. In this section we present the statistics of redshift for different optical classes of AGN: BL Lacs and FSRQ, as well as the redshift distribution of BL Lac SED classes.

Flat spectrum radio quasars are known to evolve positively: there were more FSRQ in the past (Dunlop and Peacock, 1990). Cosmic evolution of BL Lacs, on the other hand, is still under a debate. This is understandable considering the problematics regarding the redshift determination which translates into smaller sample and ambiguities. FSRQ from Fermi catalog all have assigned redshifts. Majority of BL Lacs do not: only 326 BLL sources have assigned redshift. Other 247 have reported redshift of 0 (zero). This was assumed for SED classification (Ackermann et al., 2015). There has been reported a suggestion to assign a redshift of $z = 1$ for these sources (Giommi et al., 2013).

BL Lac object with the lowest redshift reported in 3FGL is J2204.4+0439 with $z = 0.027$. Highest redshift ($z = 2.471$) is reported for 3FGL J1450.9+5200 BL Lac source. Flat spectrum quasar with the lowest redshift is 3FGL J1330.0-3818 ($z = 0.02843$) while furthest FSRQ is 3FGL J0540.0-2837 with redshift of 3.104. Redshift distribution for both blazar classes is given in Fig. 5.17 and the parameters are reported in Table 5.6. Assuming the 3FGL reported redshifts, our first conclusion from Fig. 5.17 is the positive evolution of FSRQ and negative evolution of BL Lacs.

Table 5.6: Parameters for redshift distribution of sampled classes of blazars. It is to be noted that majority of BL Lac sources lack redshift value in the catalog which reduced their number to 326 in our study.

Object class	Number of sources	Number of bins	Redshift interval
BLL	326	20	$0.027 < z < 2.471$
FSRQ	484	25	$0.0284 < z < 3.104$

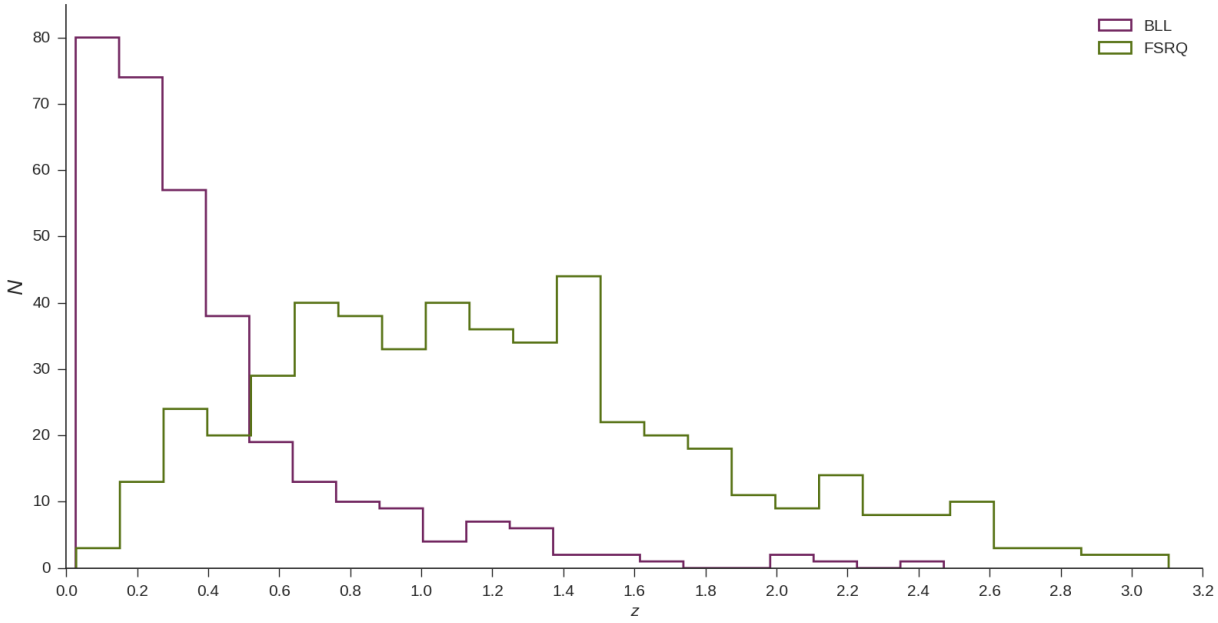

Figure 5.17: Redshift distribution of flat spectrum radio quasars (FSRQ) and BL Lacertae (BL Lac) blazars from 3FGL LAT catalog. It can be seen that FSRQ evolve positively: there were more of these objects in the past. BL Lacs, on the oher hand, are more in number in recent epoch, which leads us to a conclusion that their evolution is negative.

[3]majority of BL Lacs.

Positive evolution of flat spectrum radio quasars is in agreement with accepted stance (Dunlop and Peacock, 1990). It is evident that FSRQ started evolving around $z \sim 3$ and their peak was at redshift $z \sim 1.5$. Subsequently, although their numbers slightly dropped, they were the dominant class up to redshift $z = 0.6$. After that redshift, their number is significantly dropping. At the same time, we are reporting the rise in numbers of BL Lacs which supports the theory of negative evolution. This is consistent with (Rector et al. (2000), Beckmann et al. (2003) and Ajello et al. (2014b)). Redshift $z = 0.1$ is the redshift with the highest number of blazars of this class. We are also reporting undoubtable rise in BL Lac numbers at the same redshift where number of FSRQ dropped (and vice versa). This can also be seen in Fig. 5.17 for redshifts $z \sim 2.4$, $z \sim 2$, $z \sim 1.4$, $z \sim 1.2$, $z \sim 0.9$. There has to be a correlation. Giommi et al. (2013) argue that "BL Lacs are actually FSRQs with their emission lines swamped by the non-thermal continuum hampering determination of their redshifts." and Shaw et al. (2013) are pointing out that measured redshifts are biased low.

We also investigated how BL Lac SED subclasses evolve. We compared them among themselves and with FSRQ class. Parameters are given in Table 5.7 and results are plotted in In Fig. 5.18. It is obvious there is a similar trend for HSP and ISP BL Lac subclass. However, LSP category does not evolve as dramatically as high and intermediate ones. This needs further investigation.

Table 5.7: Parameters for redshift distribution of SED classes of BL Lacs and FSRQ.

Object class	Number of sources	Number of bins	Redshift interval
BLL-HSP	170	15	$0.031 < z < 2.1$
BLL-ISP	72	15	$0.027 < z < 2.471$
BLL-LSP	72	15	$0.041 < z < 2.017$
FSRQ	484	25	$0.0284 < z < 3.104$

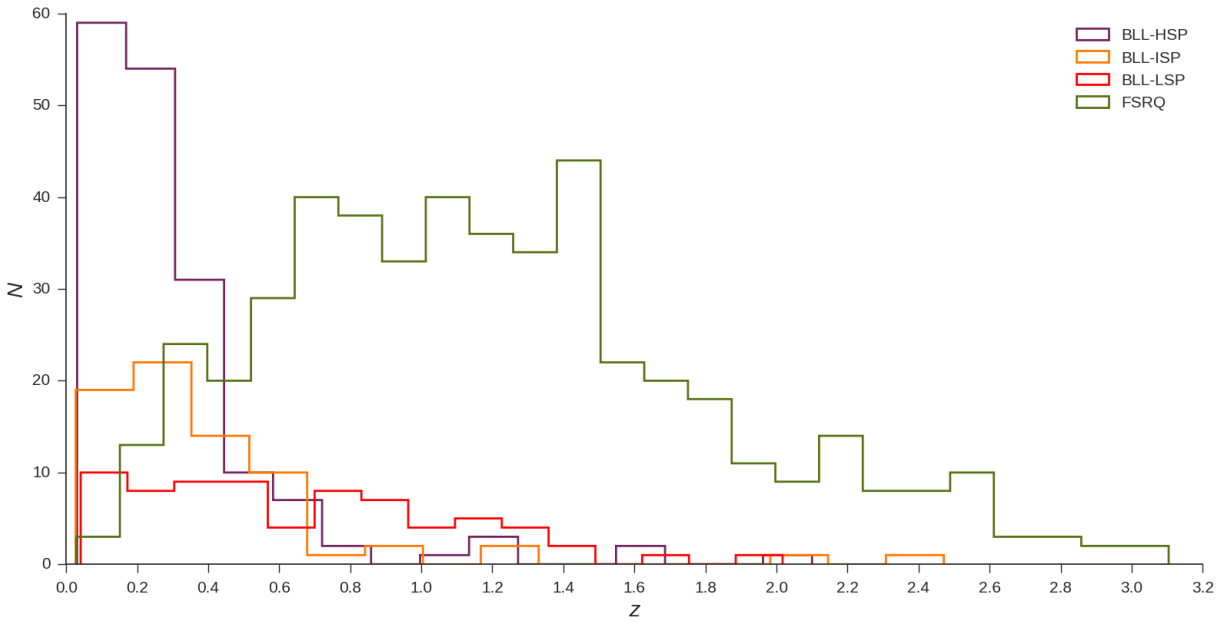

Figure 5.18: Redshift evolution of BL Lac SED subclasses and FSRQ. Purple line represents HSP BL Lacs, orange line is ISP BL Lac while red line is LSP-BL Lac. Green line shows FSRQ. There is an obvious rapid negative evolution for HSP and ISP class while LSP class, although evolving negatively, it is not as dramatic as in HSP and ISP case. 3FGL BL Lacs with redshit $z = 0$ are not included in this sample.

Lastly, we investigated how the ratio of fluxes in X and radio domain of two blazar classes evolve with redshift. This is represented in Fig. 5.19. A strong similarity to situation represented in Fig. 5.17 can be noted. We found that fluxes are tightly contained in certain regions of plot while completely absent in other. When compared to color-color diagram in Fig. 5.19 we can see contours have changed for different redshifts. This calls for further inspection.

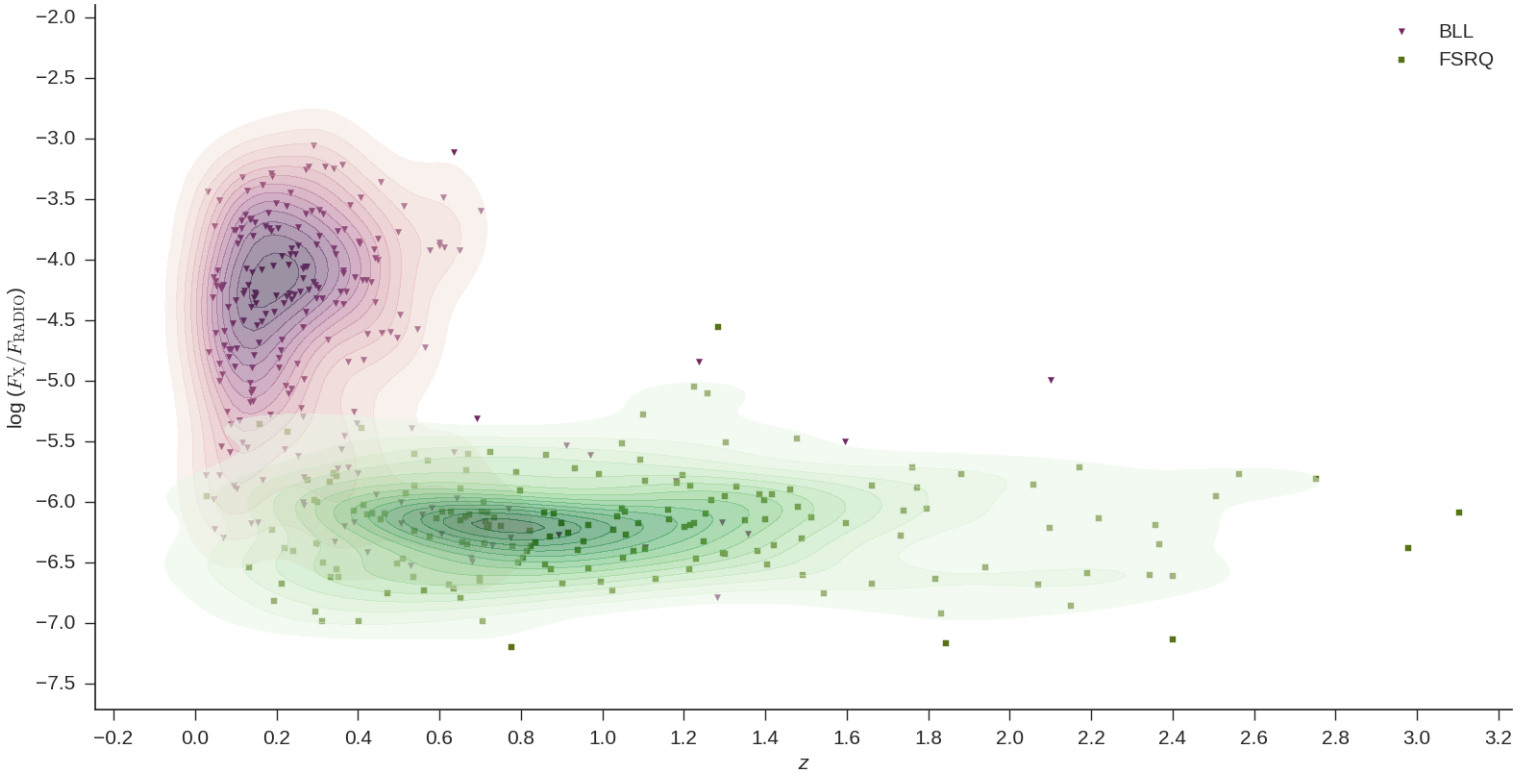

Figure 5.19: Redshift evolution of X/RAD flux ratios for BL Lacs (purple) and FSRQ (green) blazars.

Chapter 6

Analysis of selected gamma-sources: color-color diagrams

In this chapter, we present the results of second part of our work: the construction of color-color diagrams (CCD) for our selected sample of sources. The description of our method of data reduction was described in §4. In this part we will only focus on analysis. Chapter is divided into sections, each dealing with different category of sources. In the first segment we will analyze CCDs for optical classes and in the following section, CCDs of SED classes will be discussed. Section 3 will describe our finding regarding the 3FGL sources with known optical class which lack the SED classification. We will briefly touch the ISP SED class and our findings regarding sources 3FGL J0250.6+1713 and 3FGL J0202.3+0851 in the subsequent segments. We will finish our work by using our diagnostic plots to a cross-correlation with some sources from 2FGL and 3FGL catalog. *A note to reader: all flux ratios; that is, ratios of fluxes in X and radio will be referred to as X/Rad, ratios of fluxes in gamma and X will be referred to as G/X and so forth.*

6.1 Optical classes

For our optical classes, that is for our selected sample of blazars (BL Lacs, FSRQs and BCUs) and pulsars, we constructed three color-color diagrams: Rad/X vs G/X, Vis/Rad vs G/X and X/Rad vs X/Vis. Each CCD will be discussed in the following subsections.

X/Rad vs G/X diagram

Our first diagnostic plot (Fig. 6.1a) has values of ratios of fluxes in gamma and X on abscissa and flux ratio of X and radio on ordinate. The basic parameters of our plot are given in Table

Table 6.1: Parameters for X/Rad vs G/X color-color diagram, given in Fig **??**.

Object class	Number of sources	Number of levels
BLL	397	15
FSRQ	177	15
BCU	178	-
PSR	48	-

The first result we are reporting is an obvious clustering depending on the class of the object. Contours are plotted for BLL and FSRQ blazar classes only as BCU are of unknown optical class (and are therefore too scattered). Pulsars show some grouping but are nonetheless very dispersed. However, there is a clear distinction between a pulsar and a blazar in this plot. The most representative are blazar classes: BL Lacs and FSRQ. BL Lacs are confined to a region between $\log(F_\gamma/F_\mathrm{X})$ -9 and -5.5 and $\log(F_\mathrm{X}/F_\mathrm{Rad})$ = -7 and -3. FSRQ occupy a region on the diagram within approximate values of $\log(F_\gamma/F_\mathrm{X})$= -8.5 and -5.5. On the y-axis, they are contained between -7 and -5. BL Lac X/Rad ratio is lower than that of FSRQ. The situation is opposite for FSRQ: their X/Rad ratio is higher. This can be used as a good indication when dealing with classification of unknown sources. Using only these flux ratios we can make an educated guess to which blazar class each BCU belongs to. Similar result

was reached by Iani (2014) for 2FGL sources. The trend of the whole population contained in BLL and FSRQ region[1], i.e. the obvious slope or lack of it will be adressed in the end, in Ch.**??**. We are also reporting a slight hint of bimodal distribution for flat spectrum radio quasars.

Vis/Rad vs G/X

The next diagnostic plot we created is a Vis/Rad vs G/X (Fig. 6.1b). Abscissa has logarithmic values of gamma flux over X-flux and ordinate has a ratio of fluxes in optical and radio. Parameters are given in Table 6.2. Our sample is much smaller for each class in this case since there is a lack of data for flux in optical band.

Table 6.2: Parameters for diagnostic plot Vis/Rad vs G/X, given in Fig. 6.1b.

Object class	Number of sources	Number of levels
BLL	375	15
FSRQ	162	15
BCU	126	-
PSR	16	-

A distinction between blazar populations is present as was in last case, again with some overlapping. BL Lacs are distributed between -9 and -6 on $\log(F_\gamma/F_\mathrm{X})$ axis and range from -4.5 to 0 on ordinate. Flat spectrum radio quasars are somewhat tighter distributed in both x and y axes: they cover a range from approximately -8.5 to -5.5 on $\log(F_\gamma/F_\mathrm{X})$ axis. In y-dimension, they can be found between -4.5 and -2.5. In this case, we are also reporting a slight bimodality but now for both BL Lac and FSRQ class. The general conclusion is that the Vis/Rad ratio is greater for flat spectrum radio quasars. An estimation regarding pulsar distribution is hard to give in this case, reason being the sample is too small and their values are way too dispersed (one pulsar can be found in the region very well populated by BL Lacs, for example).

X/Rad vs X/Vis

Last plot we constructed for optical classes was X/Rad vs X/Vis diagram and can be seen in Fig. 6.1c. Number of sources and number of levels in contours for each class are the same as in previous case and are given in Table 6.3.

Table 6.3: Parameters for diagnostic plot Vis/Rad vs G/X, given in Fig. 6.1b.

Object class	Number of sources	Number of levels
BLL	375	15
FSRQ	162	15
BCU	126	-
PSR	16	-

The distribution for pulsars is the same as before: they are quite sparse and scattered, although they seem to populate the region where X/Vis ratio is high (again, few pulsars can be found in blazar-dominated regions). Blazars, on the other hand, show very interesting distribution: BL Lacs are very spread out while FSRQs are tightly contained. To give numerical values: BL Lacs are distributed from -5 to -1 in X/Vis and from -7 to -3 in X/Rad (which we already established in first CCD). Flat spectrum radio quasars seem concentrated between -3.5 and -1.5 X/Vis region and between 7.5 and -5.5 in X/Rad dimension. We do not notice bimodality in distribution of FSRQ in this diagnostic plot. However, BL Lac distribution is showing some trend. There is also an overlap of distributions present.

[1] for this and for all subsequent CCDs.

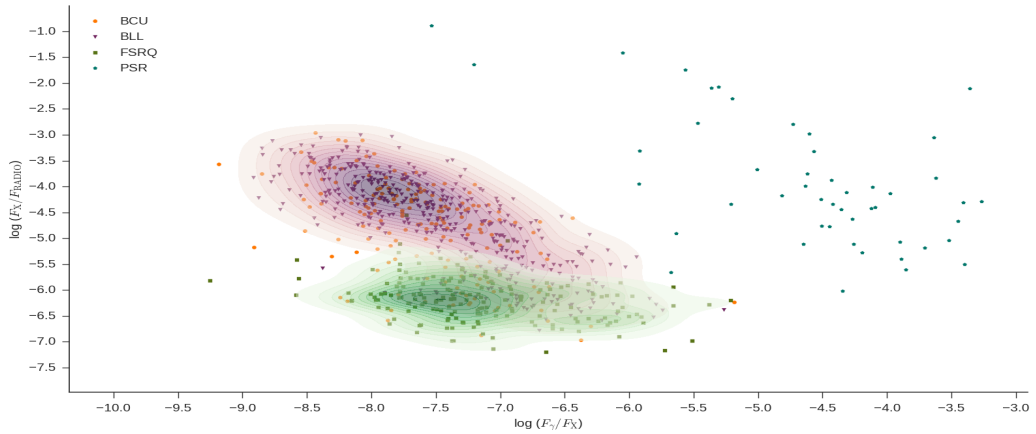

(a) X/Rad vs G/X

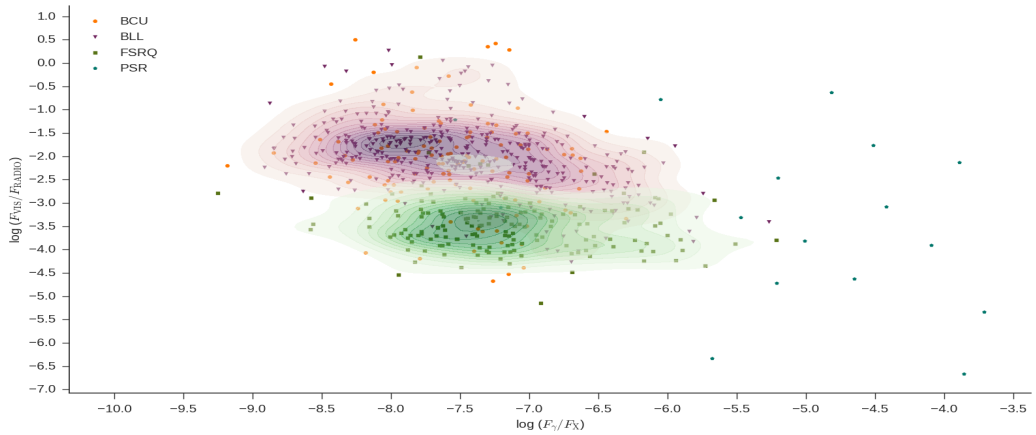

(b) Vis/Rad vs G/X

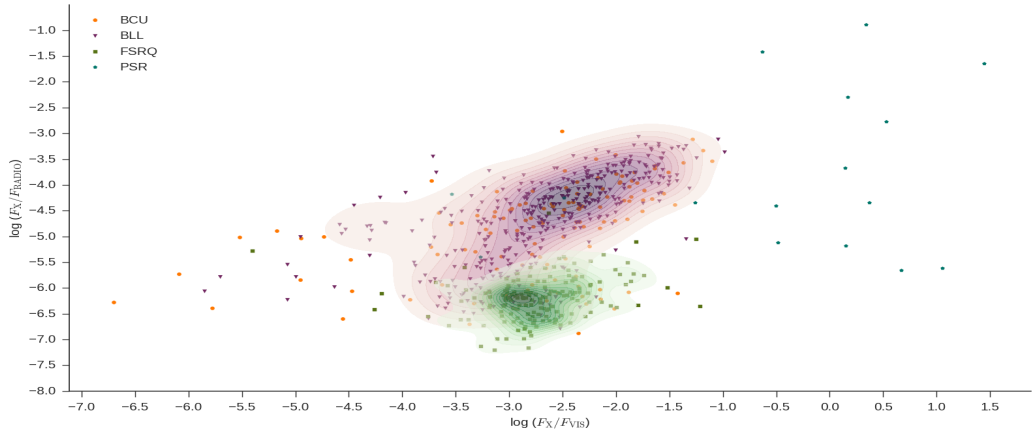

(c) X/Rad vs X/Vis

Figure 6.1: Color-color diagrams for optical classes

6.2 SED classes

The next step we took was to construct color-color diagrams in the same manner but now for blazar SED classes (naturally, pulsars and BCUs are omitted). This is shown in Fig. 6.7. Results are almost identical to distributions of BL Lacs and FSRQ, which is to be expected. The only difference now is the less prominent or complete absence for signs of bimodality for HSP and LSP classes. In order not to be repetative, we will not describe the obvious similarities but we will point out to some interesting results we obtained.

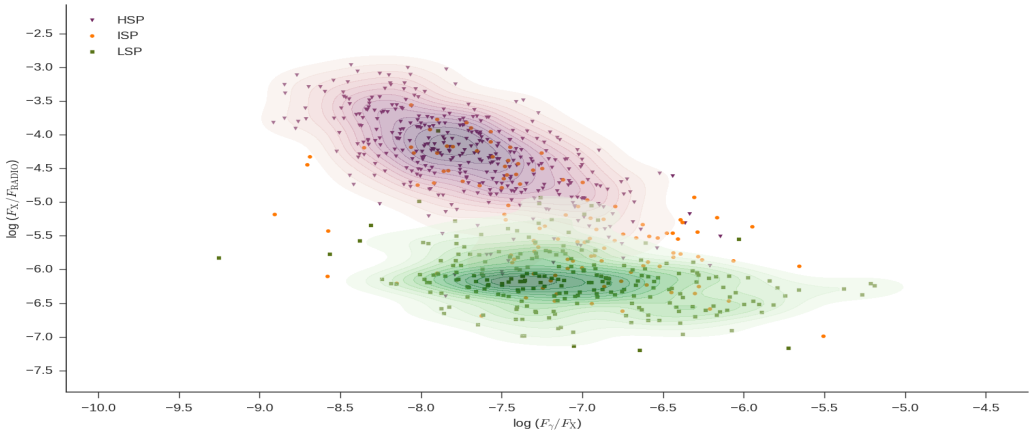

(a) X/Rad vs G/X

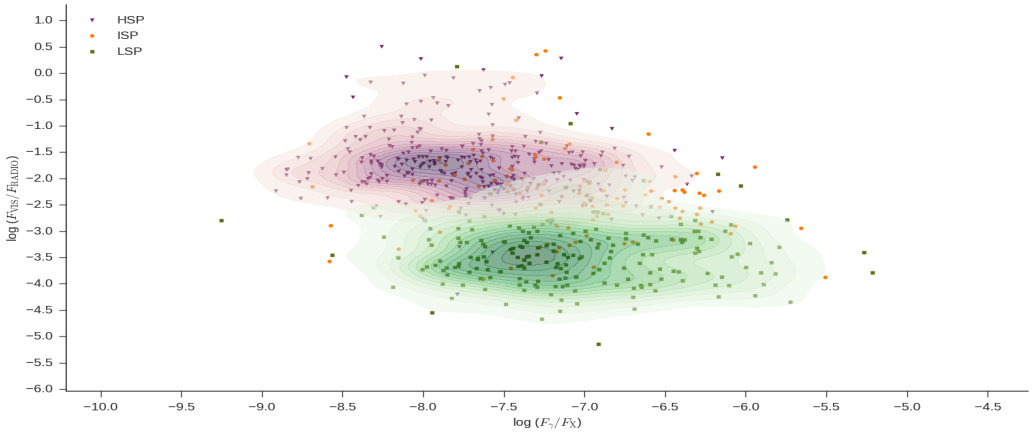

(b) Vis/Rad vs G/X

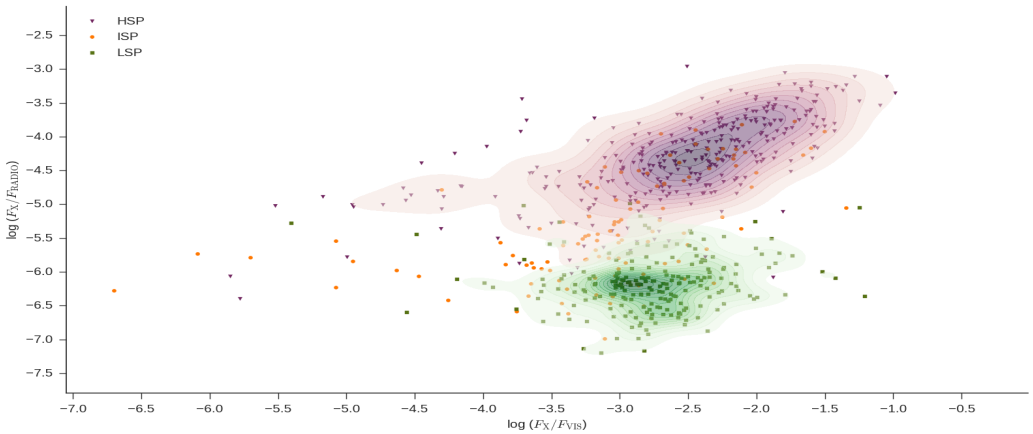

(c) X/Rad vs X/Vis

Figure 6.2: Color-color diagrams for SED classes

ISP class

Blazars are divided into three classes, based on the value of the rest-frame broadband-SED synchrotron peak frequency $\nu^S_{\rm peak}$ into 3 SED classes:

- **High-synchrotron peaked blazar (HSP)**: for

$$\nu^S_{\rm peak} > 10^{15}{\rm Hz}$$

- **Intermediate-synchrotron peaked (ISP)**: for

$$10^{14}{\rm Hz} < \nu^S_{\rm peak} < 10^{15}{\rm Hz}$$

- **Low-synchrotron peaked (LSP)**: for

$$\nu^S_{\rm peak} < 10^{14}{\rm Hz}$$

This classification and the motivation behind the classification is reported in Ackermann et al. (2011) and (Ackermann et al., 2015). They also reported that some sources (now in 3LAC catalog) changed the original 2LAC SED classification. However, when we constructed the SED-CCDs, we found a clear bimodality for the intermediate class: sources tend to fall into HSP or into LSP category. This is shown in Figs. 6.3, 6.4a and 6.4b. We are suggesting that while ISP subcategory might have practical purpose for catalog construction, in reality only leads to further confusion in already confused and overly-complicated field of AGN.

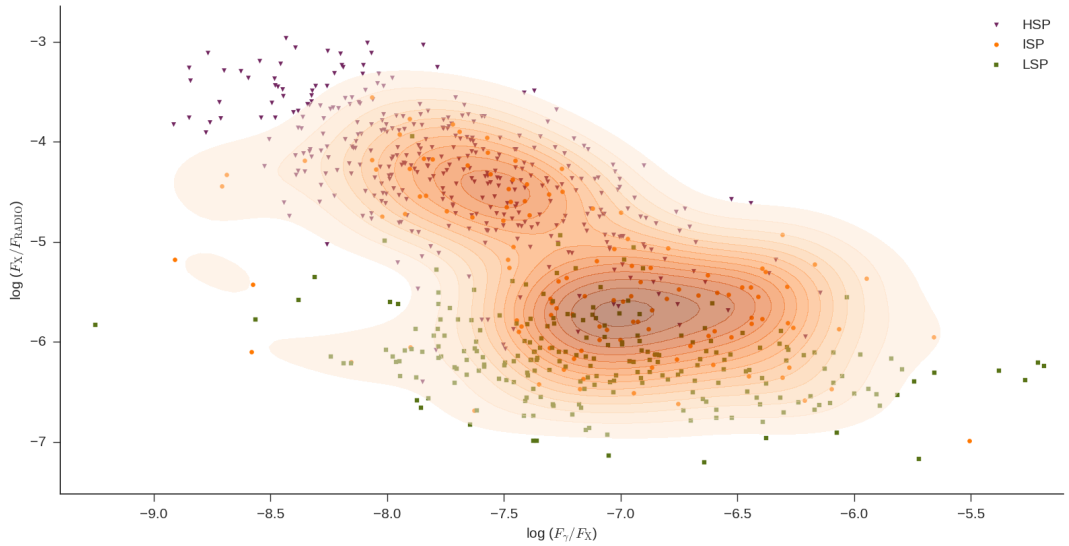

Figure 6.3: X/Rad vs G/X for ISP SED class. Bimodal trend of distribution is present.

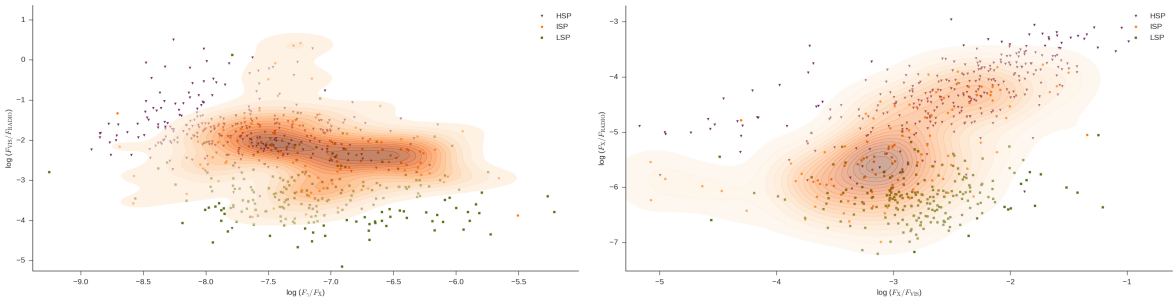

(a) Vis/Rad vs G/X for ISP SED class

(b) X/Rad vs X/Vis for ISP SED class

Sources 3FGL J0250.6+1713 and 3FGL J0202.3+0851

While constructing and analyzing color-color diagrams, we noticed inconsistency with 3FGL J0250.6+1713 and 3FGL J0202.3+0851 sources. They are classified as flat spectrum radio quasars (FSRQ). At the same time, they are classified as HSP sources. It should be mentioned that they are the *only* two sources categorized as such (FSRQ-HSP). To investigate this, we plotted these two sources on a color-color diagram in such a way that we took both optical and SED classes into account. In other words: in Fig. 6.5 optical class is plotted over an SED contour. That way we secured we are certain where does each optical class belong to. The results confirmed out suspicion: there is a clear inconsistency with classification of these sources. In the literature, it can be seen that BL Lacs can be further divided into three SED subclasses. However, FSRQ are only ISP or LSP (Ackermann et al. (2015), Boettcher (2010), Shaw et al. (2013)). We are proposing this is a confusion and it is probably a case to which Shaw et al. (2013) refer to as "A BLL observed in a FSRQ state".

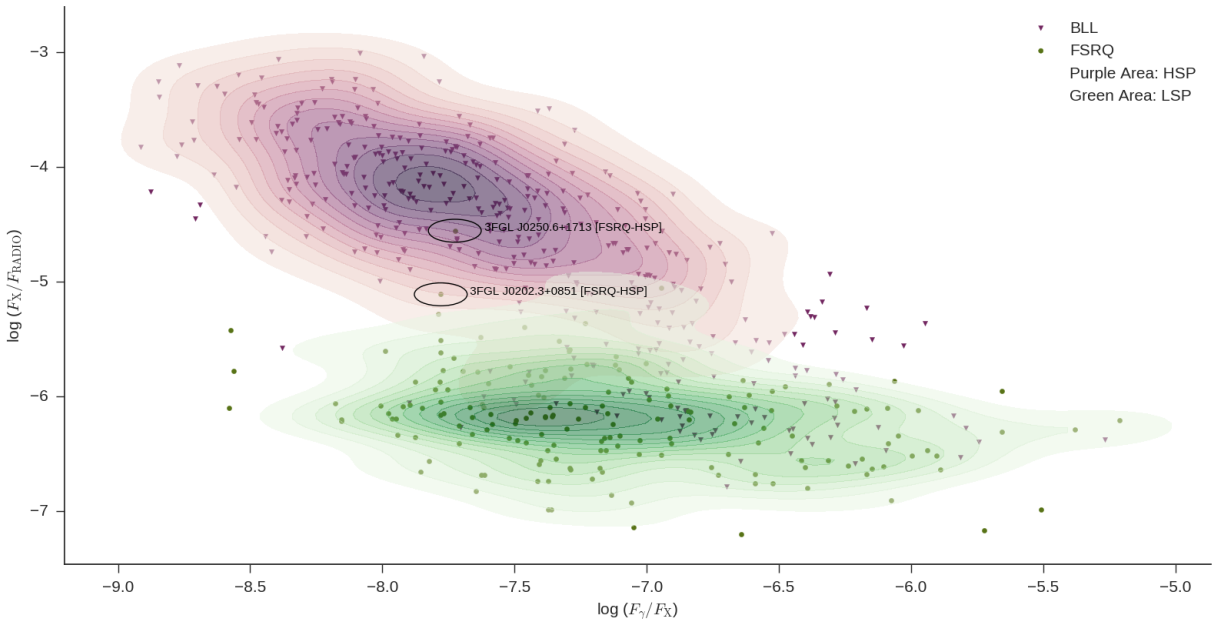

Figure 6.5: X/Rad vs G/X diagram for optical and SED classes with sources 3FGL J0250.6+1713 and 3FGL J0202.3+0851 marked.

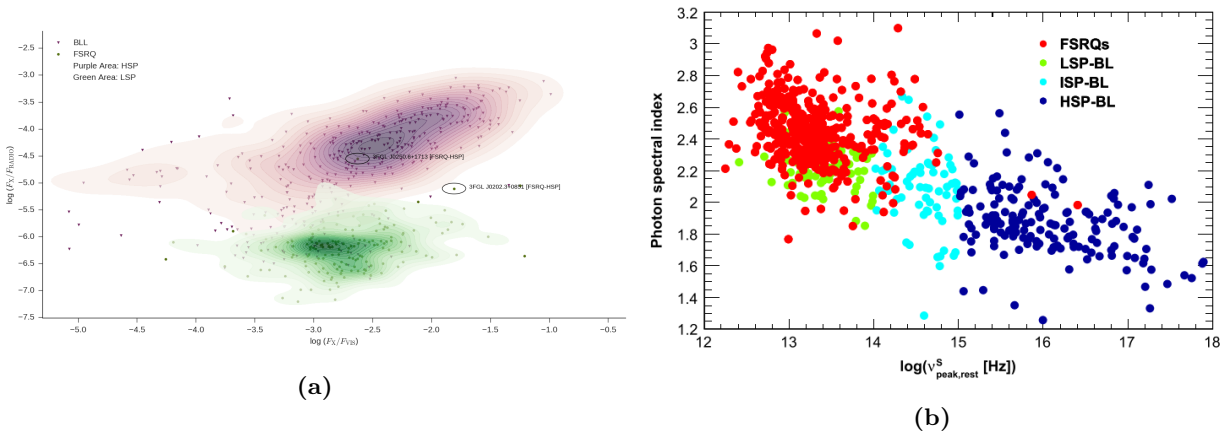

(a) **(b)**

Figure 6.6: (a) X/Rad vs X/Vis diagram for optical and SED classes with sources 3FGL J0250.6+1713 and 3FGL J0202.3+0851 marked and (b) Photon spectral index vs. frequency of synchrotron peak: the two sources we are referring to are clearly misclassified. Picture taken from (Ackermann et al., 2015).

6.3 Sources with unknown SED

In this section, we put our color-color diagrams to test. There are 42 sources in The Third FERMI catalog that have either have an optical classification or are classified as BCUs but lack an SED classification. Since there is sufficient information available in 3FGL that allows placement in the CCD, we placed these sources over our countours in order to predict their SED classification. We will refer to these sources as UK (Un-Known). The diagrams are given in Figs. 6.7a, 6.7b and 6.7c. We need to emphasize that several sources do not have enough data to be able to be plotted in all three color-color diagrams. In each plot, same sources have same designations. Our finding is that *all* but one source belong to HSP class and our result is given in a tabular form (Table 6.4).

Table 6.4: List of 3FGL sources without SED classification for which we predicted SED class using our diagnostic plots. The number of each source corresponds to the number in the plots given in Fig. 6.7. Class is 3FGL assigned optical class while SED represents our SED prediction.

#	Fermi name	Class	SED	#	Fermi name	Class	SED
1	3FGLJ 1132.8+1015	FSRQ	LSP	22	3FGL J0550.6-3217	BLL	HSP
2	3FGL J0512.2+2918	BCU	HSP	23	3FGL J0054.8-2455	BLL	HSP
3	3FGL J0131.3+5548	BCU	HSP	24	3FGL J1943.2-3510	BLL	HSP
4	3FGL J2336.5+2356	BCU	HSP	25	3FGL J0723.2-0728	BCU	HSP
5	3FGL J2108.6-8619	BCU	HSP	26	3FGL J1955.9+0212	BCU	HSP
6	3FGL J0244.4-8224	BCU	HSP	27	3FGL J0103.4+5336	BLL	HSP
7	3FGL J1129.4-4215	BCU	HSP	28	3FGL J0503.5+6538	BLL	HSP
8	3FGL J0525.6-6013	BCU	HSP	29	3FGL J0509.7-6418	BCU	HSP
9	3FGL J1030.4-2030	BCU	HSP	30	3FGL J1606.1+5630	BLL	HSP
10	3FGL J1136.9+2551	BLL	HSP	31	3FGL J0111.5+0535	BLL	HSP
11	3FGL J0040.3+4049	BCU	HSP	32	3FGL J1451.2+6355	BLL	HSP
12	3FGL J0626.6-4259	BCU	HSP	33	3FGL J2152.9-0045	BLL	HSP
13	3FGL J2250.1+3825	BLL	HSP	34	3FGL J1149.5+2443	BLL	HSP
14	3FGL J0627.9-1517	BCU	HSP	35	3FGL J2131.8-2516	BLL	HSP
15	3FGL J1504.5-8242	BCU	HSP	36	3FGL J1123.6+7231	BLL	HSP
16	3FGL J2041.7-3732	BLL	HSP	37	3FGL J0304.3-2836	BLL	HSP
17	FGL J1158.9+0818	BCU	HSP	38	3FGL J1744.9-1725	BCU	HSP
18	3FGL J2312.9-6923	BCU	HSP	39	3FGL J1218.5+6912	BCU	HSP
19	3FGL J0116.2-2744	BCU	HSP	40	3FGL J0528.3+1815	BCU	HSP
20	3FGL J1711.6+8846	BCU	HSP	41	3FGL J2246.7-5205	BCU	HSP
21	3FGL J1849.3-1645	BCU	HSP	42	3FGL J0409.4+3158	BCU	HSP

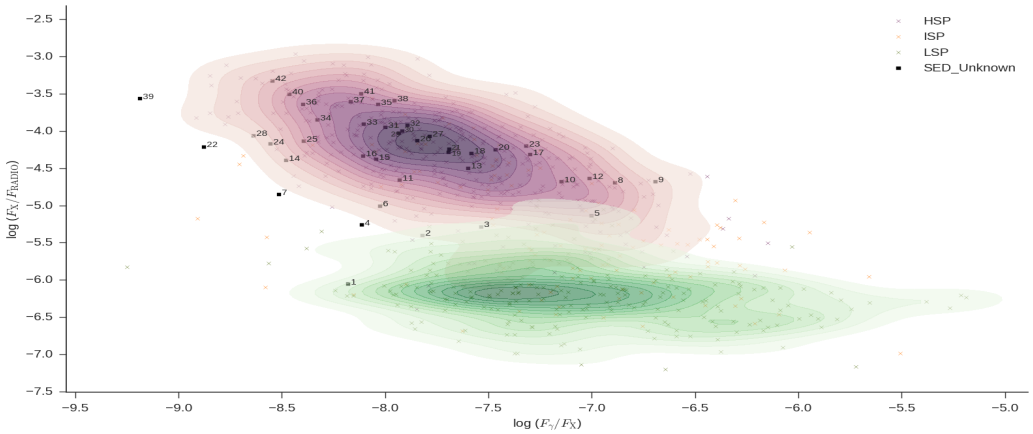

(a) X/Rad vs G/X

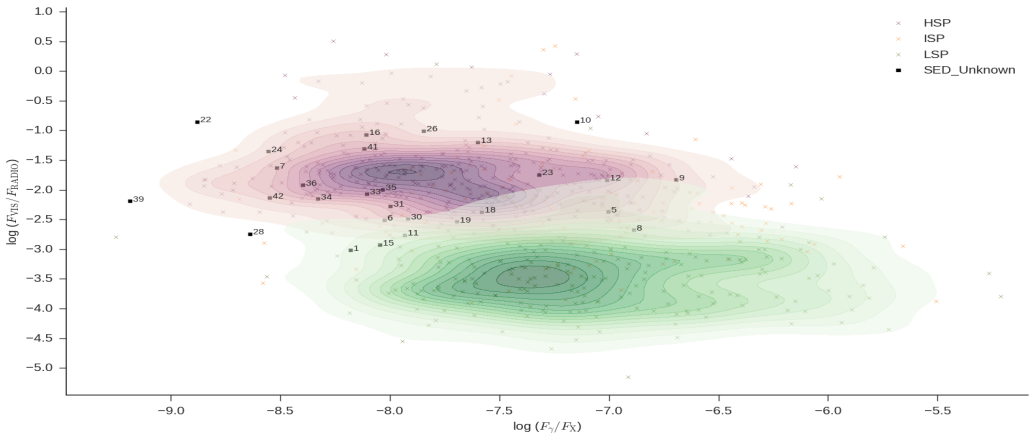

(b) Vis/Rad vs G/X

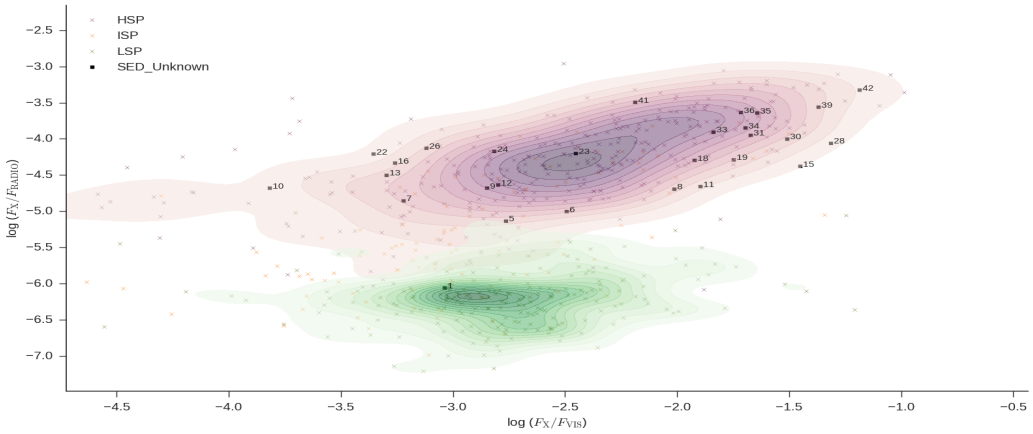

(c) X/Rad vs X/Vis

Figure 6.7: Color-color diagrams used as diagnostic plots to predict an SED class of 3FGL sources

6.4 Unassociated Fermi Objects (UFOs)

The last part of our work was to test our diagnostic plots against recently classified objects from Fermi catalog and, at the same time, double-check those sources and their classification.

6.4.1 2FGL Test data

The first test data sample was taken from (Paiano, 2014). Sample consists of 7 sources and their 2FGL name and association proposed by Paiano (2014) are given in Table 6.5. For each source, fluxes in gamma, X and radio were normalized and then flux ratios calculated in order to plot them on a color-color diagnostic plot (Fig. 6.8). We conclude test data taken from this PhD thesis is in agreement with our diagnostics.

Table 6.5: First test data sample to cross-correlate with our diagnostic plots. Data was taken from (Paiano, 2014). HBL and LBL are different notation for HSP and LSP SED classes.

2FGL name	Association
2FGL J1129.0+3758	FSRQ
2FGL J0227.7+2249	LBL
2FGL J0102.2+0943	LBL
2FGL J1614.8+4703	LBL
2FGL J0338.2+1306	HBL
2FGL J1511.8-0513	HBL
2FGL J0143.6-5844	HBL

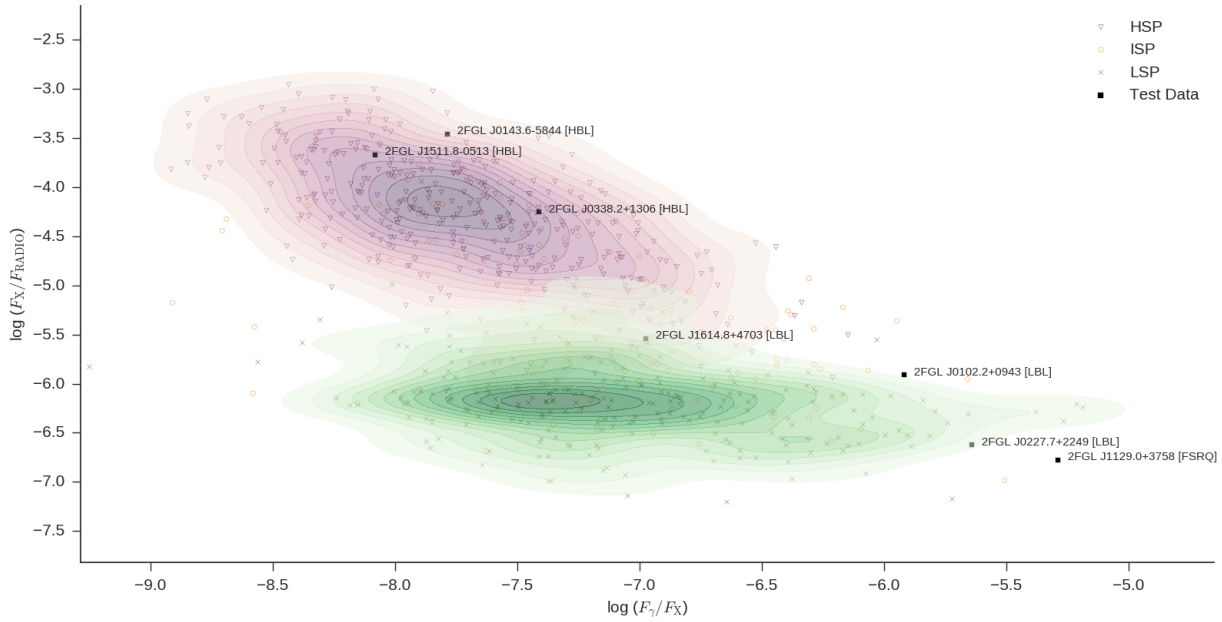

Figure 6.8: Data from sample 1 plotted onto our color-color diagram. The test data are agreening with out diagnostics.

6.4.2 3FGL Test data

We also present flux ratio distribution as a funtion of redshift as a diagnostic plot. We use it to test SED classificaton proposed by Paiano et al. (2017).

To test the data for which an SED class and redshift was proposed by Paiano et al. (2017), we constructed a diagnostic plot. Parameters of this test data sample is given in Table 6.6. Our diagnostic plot is similar to the ones already presented in this work. The difference now is that we plotted 3FGL redshifts on abscissa and ratio of fluxes in X and radio bands on ordinate. On top of that, we plotted data from this data sample, using the fluxes presented in the paper (Paiano et al., 2017). The plot is given in Fig. 6.9. Our finding is that most of test sources are in agreement with our method of classification determination. However, we are suggesting a few changes which we present in the Table 6.7. Sources that we suggest need further investigation are: 3FGL J0102.2+0943 (Fig. 6.10), 3FGL J0116.3-6153 (Fig. 6.11) and 3FGL J2115.2+1213 (Fig. 6.12), marked as A, B and K in Fig. 6.9, respectively. Our proposition is that the sources belong to LSP class which would also imply the change of redshift value, taking into account the method explained by Paiano et al. (2017).

Table 6.6: 3FGL sources for which a redshift and an SED class was proposed by Paiano et al. (2017).

Fermi name	Proposed SED	Proposed redshift
3FGL J0102.2+0943	HSP	0.5
3FGL J0116.3-6153	HSP	0.4
3FGL J0143.7-5845	HSP	0.3
3FGL J0338.5+1303	HSP	0.3
3FGL J1129.0+3758	LSP	1.6
3FGL J1410.9+7406	HSP	0.6
3FGL J1502.2+5553	LSP-ISP	1.7
3FGL J1511.8-0513	HSP	0.1-0.2
3FGL J1615.8+4712	ISP	0.3
3FGL J1704.1+1234	HSP	0.3
3FGL J2115.2+1213	HSP	0.4
3FGL J2246.2+1547	ISP	0.3
3FGL J2346.7+0705	ISP/HSP	0.2

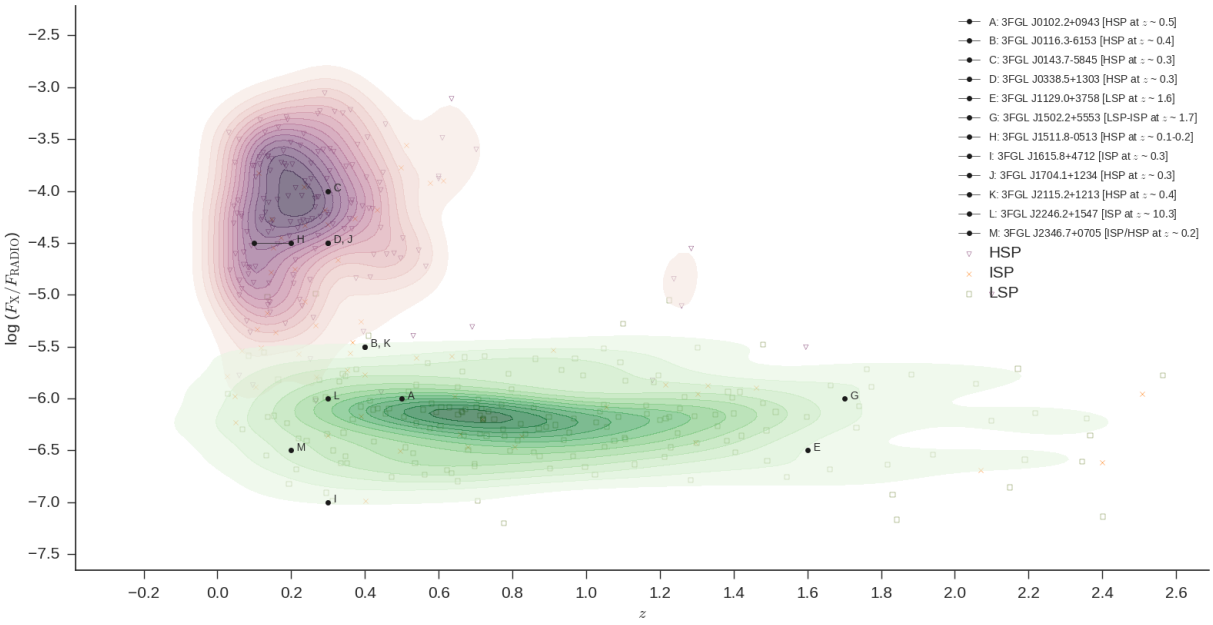

Figure 6.9: Diagnostic plot: on abscissa we ploted the redshifts available from 3FGL. Y-axis represents X and radio flux ratios. Test data parameters are given in Table 6.6 and are taken from (Paiano et al., 2017). Sources marked as A, B and K (and classified by Paiano et al. (2017) are not in agreemed with our diagnostic plot. We suggest further investigation of these sources.

Table 6.7: Our suggestion for classification and corresponding redshift of the three sources that are not in agreement with aour diagnostics. Values of the newly proposed redshifts are taken from (Paiano et al., 2017).

Fermi name	Newly proposed SED	Newly proposed redshift
3FGL J0102.2+0943	LSP	1.1
3FGL J0116.3-6153	LSP	1.1
3FGL J2115.2+1213	LSP	1.0

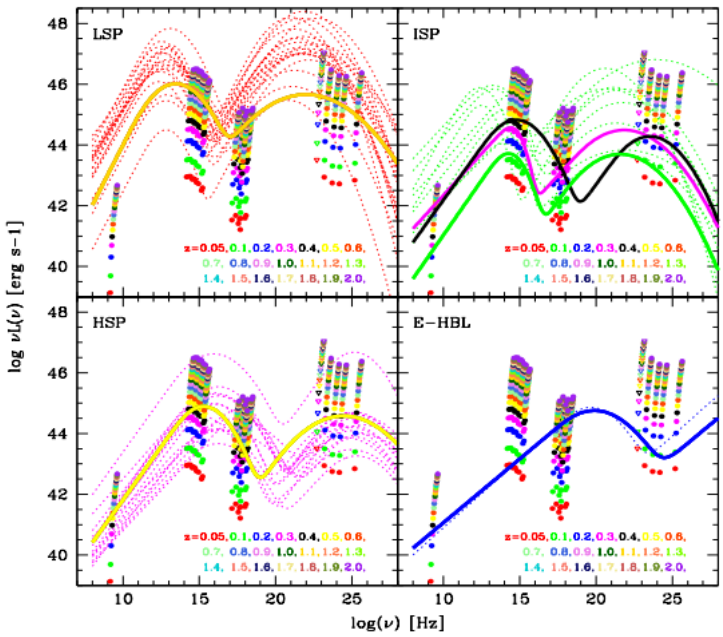

Figure 6.10: Diagnostic plot used to determine an SED class and redshift of 3FGL J0102.2+0943 by Paiano et al. (2017). Plots are taken from the same work and depict all possible SED classifications. E-HBL represents the extreme-HBL source.

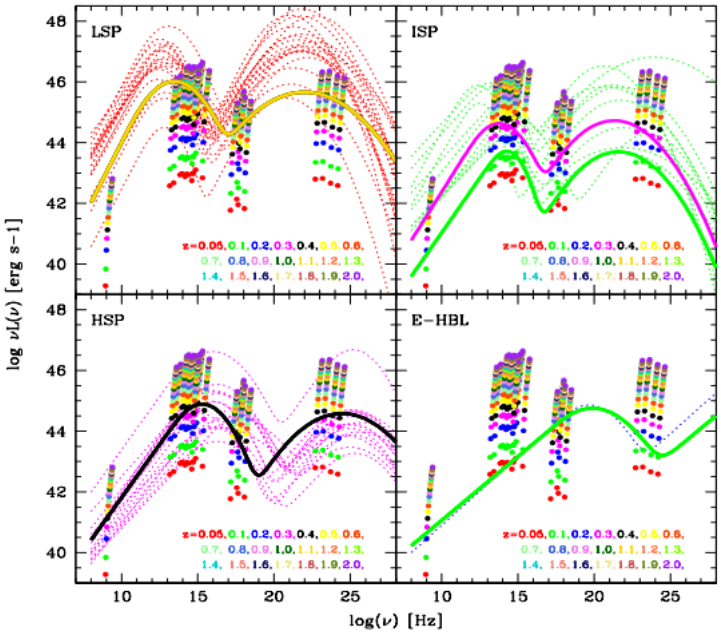

Figure 6.11: Diagnostic plot used to determine an SED class and redshift of 3FGL J0116.3-6153 by Paiano et al. (2017). Plots are taken from the same work and depict all possible SED classifications. E-HBL represents the extreme-HBL source.

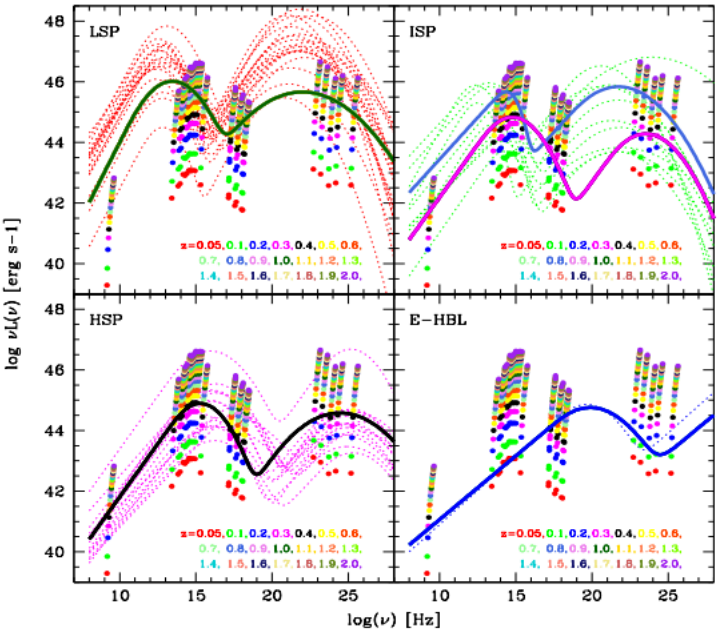

Figure 6.12: Diagnostic plot used to determine an SED class and redshift of 3FGL J2115.2+121 by Paiano et al. (2017). Plots are taken from the same work and depict all possible SED classifications. E-HBL represents the extreme-HBL source.

Chapter 7

Conclusion

In this work we used data from the Third Fermi LAT catalog, and analyzed them together with photometric data at other wavelengths to investigate the astrophysical nature of the various populations of cosmic sources emitting gamma-rays. The Thesis followed two main paths:

- a statistical analysis of already known and identified classes of sources in 3FGL;
- a detailed comparison of the population of unidentified sources from 3FGL to the populations of already identified sources from 3FGL, and inferences about their nature.

Here are our main results.

For our first line of investigation, the conclusion is that, although the information is sparse and there are many ambiguities and obstacles (especially for the sources near the Galactic Ridge), all data indicate that:

- galactic sources have higher fluxes, due to their small distance. Intrinsically, of course, extra-galactic sources are much more energetic than the galactic ones;
- the majority of unassociated sources are most likely to be AGNs;
- there is a certain asymmetry in the spatial distribution of analyzed sources. In the case of galactic latitudes, that is explained by the fact there are more cataloged sources in the northern hemisphere than in southern (catalogs in questions are the one Fermi uses in the automated data association). However, this trend exists for other parameters, for which we are unable to provide an explanation at this point;
- flat spectrum quasars are much more variable than BL Lacs;
- FSRQ also have slightly higher fluxes than BL Lacs;
- pulsars have, on average, lower spectral indices than blazars and at the same time they display a high energy cut-off;
- judging by the variability index, most BCUs are of probably BL Lac type;
- flat spectrum radio quasars evolve positively with redshift (there were more FSRQ in the past);
- BL Lacs evolve instead negatively with redshift. The evolution of HSP and ISP class of BL Lacs is more pronounced than that of LSP class of BL Lacs, that is they fall off faster with redshift;

The second line of our work involved the construction of color-color diagrams and using them as diagnostic tools to investigate the nature of unidentified and unassociated Fermi sources. Here is the summary of our findings:

- fluxes in the optical band do not seem to be very useful in building the color-color diagrams in this way, as they tend to produce confused plots, perhaps partly because of the contribution of the host galaxy;

- pulsars particularly lack information in optical band, because they are too faint there, which reduced our sample significantly. In any case, they show extreme dispersion in the diagnostic diagrams and we suggest that a much larger sample is needed in order to extract some knowledge about these interesting objects;
- there is a definite correlation between the optical class of blazars and their SED type. FSRQ tend to have synchrotron peaks at low frequencies;
- based on kernel density estimation, we observed a slightly bimodal trend in the optical classes and SED classes in color-color diagrams;
- the intermediate synchrotron peaked (ISP) class is a confused one and exhibits a strong bimodality: objects classified as ISP are either HSP or LSP, based on our findings;
- using our diagnostic plots, we predict an SED classification for 42 Fermi objects (listed in § 6.3), most of them published as BCU sources (blazar candidate of unknown type);
- we are suggesting that published associations or identifications of objects designated as 3FGL J0250.6+1713 and 3FGL J0202.3+0851 are wrong;
- we suggest that objects designated as 3FGL J0102.2+0943, 3FGL J0116.3-6153 and 3FGL J2115.2+1213, found in (Paiano et al., 2017) are wrong. We suggest for them a different classification and, consequently, a different redshift for these sources;
- our diagnostic plots are very reliable, based on test data.

Lastly, we have identified many possibilities for future work. Even without new associations, a lot can be done with already existing data. For example, we noticed some clear correlations in sample distributions of our color-color plots. We estimated the slopes using linear regression functions: what is left is to interpret it. We can also use our diagnostic plots to check new data when they will become available. In near future, when more classes are identified and data processed, further statistical analysis like ours can be made that will provide a better understanding of the gamma-ray sky.

References

F. Acero, M. Ackermann, and M. et al. Ajello. Fermi Large Area Telescope Third Source Catalog. ApJS, 218:23, June 2015. doi: 10.1088/0067-0049/218/2/23.

M. Ackermann, M. Ajello, A. Allafort, E. Antolini, W. B. Atwood, M. Axelsson, and L. et al. Baldini. The Second Catalog of Active Galactic Nuclei Detected by the Fermi Large Area Telescope. ApJ, 743:171, December 2011. doi: 10.1088/0004-637X/743/2/171.

M. Ackermann, M. Ajello, A. Allafort, and L. et al. Baldini. Detection of the Characteristic Pion-Decay Signature in Supernova Remnants. *Science*, 339:807–811, February 2013. doi: 10.1126/science.1231160.

M. Ackermann, M. Ajello, and W. B. Atwood et al. The third catalog of active galactic nuclei detected by the fermi large area telescope. *The Astrophysical Journal*, 810(1):14, 2015. URL http://stacks.iop.org/0004-637X/810/i=1/a=14.

F. A. Aharonian. TeV gamma rays from BL Lac objects due to synchrotron radiation of extremely high energy protons. New A, 5:377–395, November 2000. doi: 10.1016/S1384-1076(00)00039-7.

M. Ajello, R. W. Romani, D. Gasparrini, and M. S. et al. Shaw. The Cosmic Evolution of Fermi BL Lacertae Objects. ApJ, 780:73, January 2014a. doi: 10.1088/0004-637X/780/1/73.

M. Ajello, R. W. Romani, D. Gasparrini, and M. S. et al. Shaw. The Cosmic Evolution of Fermi BL Lacertae Objects. ApJ, 780:73, January 2014b. doi: 10.1088/0004-637X/780/1/73.

J. Aleksić, E. A. Alvarez, and L. A. et al. Antonelli. Phase-resolved energy spectra of the Crab pulsar in the range of 50-400 GeV measured with the MAGIC telescopes. A&A, 540:A69, April 2012. doi: 10.1051/0004-6361/201118166.

ASI. Agenzia spaziale italiana: Science data center. URL http://www.asdc.asi.it/.

W. B. Atwood, A. A. Abdo, and M. Ackermann et al. The large area telescope on the fermi gamma-ray space telescope mission. *The Astrophysical Journal*, 697(2):1071, 2009. URL http://stacks.iop.org/0004-637X/697/i=2/a=1071.

A. Badertscher, P. Crivelli, W. Fetscher, U. Gendotti, S. N. Gninenko, V. Postoev, A. Rubbia, V. Samoylenko, and D. Sillou. Improved limit on invisible decays of positronium. Phys. Rev. D, 75(3):032004, February 2007. doi: 10.1103/PhysRevD.75.032004.

V. Beckmann, D. Engels, N. Bade, and O. Wucknitz. The HRX-BL Lac sample - Evolution of BL Lac objects. A&A, 401:927–938, April 2003. doi: 10.1051/0004-6361:20030184.

R. D. Blandford, H. Netzer, and L. Woltjer. *Active Galactic Nuclei*. Springer Berlin Heidelberg, 1990. ISBN 978-3-540-31625-1.

M. Boettcher. Models for the Spectral Energy Distributions and Variability of Blazars. *ArXiv e-prints*, June 2010.

M. Boettcher and R. Schlickeiser. Pair annihilation radiation from relativistic jets in γ-ray blazars. A&A, 306:86, February 1996.

C. D. Dermer. Sources of GeV Photons and the Fermi Results. *Astrophysics at Very High Energies, Saas-Fee Advanced Course, Volume 40. ISBN 978-3-642-36133-3. Springer-Verlag Berlin Heidelberg, 2013, p. 225*, 40:225, 2013. doi: 10.1007/978-3-642-36134-0_3.

C. D. Dermer, J. D. Finke, R. J. Murphy, A. W. Strong, F. Loparco, and M. N. et al. Mazziotta. On the Physics Connecting Cosmic Rays and Gamma Rays: Towards Determining the Interstellar Cosmic Ray Spectrum. *ArXiv e-prints*, March 2013.

J. S. Dunlop and J. A. Peacock. The Redshift Cut-Off in the Luminosity Function of Radio Galaxies and Quasars. MNRAS, 247:19, November 1990.

FERMI. Fermi data products. URL https://fermi.gsfc.nasa.gov/ssc/data/access/.

G. Ghisellini, editor. *Radiative Processes in High Energy Astrophysics*, volume 873 of *Lecture Notes in Physics, Berlin Springer Verlag*, 2013. doi: 10.1007/978-3-319-00612-3.

P. Giommi, P. Padovani, and G. Polenta. A simplified view of blazars: the γ-ray case. MNRAS, 431: 1914–1922, May 2013. doi: 10.1093/mnras/stt305.

William F. Hanlon. Cosmic ray spectrum. URL http://www.physics.utah.edu/~whanlon/spectrum1Small.png.

http://www.star.bris.ac.uk/ mbt/topcat/sun253/ack.html. Fv: The interactive fits file editor. URL http://www.star.bris.ac.uk/~mbt/topcat/.

Edoardo Iani. Caratterizzazione delle sorgenti gamma dell'osservatorio fermi. University od Padova, 2014. Laurea Triennale in Astronomia.

Malcolm S. Longair. *High Energy Astrophysics*. Cambridge University Press, 3 edition, March 2011. ISBN 978-0521756181.

NASA-FERMI. Fermi 4-year catalog. URL https://fermi.gsfc.nasa.gov/ssc/data/access/lat/4yr_catalog/.

H. Netzer. *The Physics and Evolution of Active Galactic Nuclei*. Cambridge University Press, September 2013.

P. L. Nolan, A. A. Abdo, M. Ackermann, M. Ajello, A. Allafort, E. Antolini, W. B. Atwood, M. Axelsson, L. Baldini, J. Ballet, and et al. Fermi Large Area Telescope Second Source Catalog. ApJS, 199:31, April 2012. doi: 10.1088/0067-0049/199/2/31.

S. Paiano, A. Franceschini, and A. Stamerra. A New Method to unveil blazars among multi-wavelength counterparts of Unassociated Fermi Gamma-ray Sources. *Mon. Not. R. Astron. Soc.*, February 2017.

Simona Paiano. *A Multi-wavelength Study of Unidentified Objects in the Second Fermi Gamma-Ray catalogue*. PhD thesis, Facoltà di Scienze MM.FF.NN. Dipartimento di Fisica e Astronomia "G. Galilei", 2014.

W. Pence and P. Chai. Fv: The interactive fits file editor. URL http://heasarc.gsfc.nasa.gov/ftools/fv/.

T. A. Rector, J. T. Stocke, E. S. Perlman, S. L. Morris, and I. M. Gioia. The Properties of the X-Ray-selected EMSS Sample of BL Lacertae Objects. AJ, 120:1626–1647, October 2000. doi: 10.1086/301587.

M. S. Shaw, R. W. Romani, G. Cotter, and S. E. et al. Healey. Spectroscopy of the Largest Ever γ-Ray-selected BL Lac Sample. ApJ, 764:135, February 2013. doi: 10.1088/0004-637X/764/2/135.

W. A. Stein, S. L. Odell, and P. A. Strittmatter. The BL Lacertae objects. ARA&A, 14:173–195, 1976. doi: 10.1146/annurev.aa.14.090176.001133.